A study of molecular gas in nearby active galactic nuclei with Atacama Pathfinder EXperiment, APEX

Oliver Damkjær
vqx956

March 31, 2021

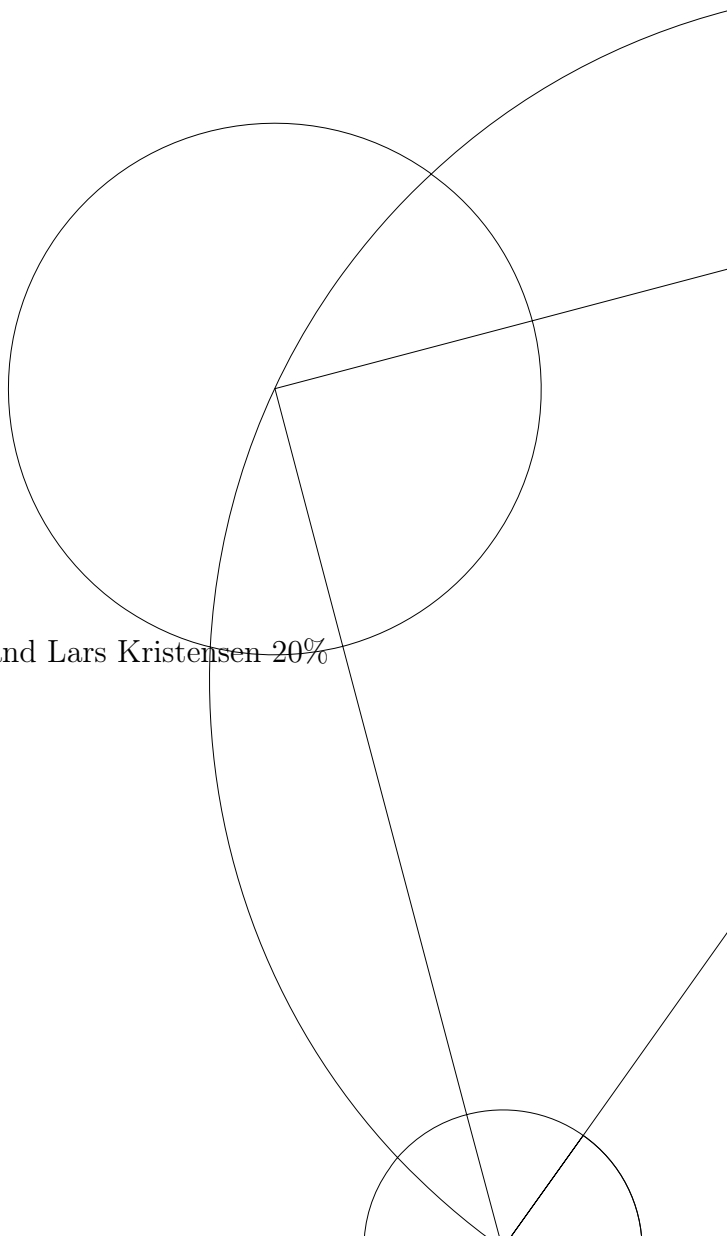

Advisors: Marianne Vestergaard 80% and Lars Kristensen 20%

Abstract

I present CO(2-1) and CO(3-2) global emission line observations of 17 nearby active galactic nuclei (AGN), carried out with the 230 GHz APEX-1 and 345 GHz APEX-2 receivers on the Atacama Pathfinder EXperiment (APEX) telescope. The main goal of this project is to probe the molecular gas content of galaxies with an actively accreting supermassive black hole in the center, to determine the physical properties and the kinematics of the molecular gas. I further corrected these results, for potential CO emission falling outside the primary APEX telescope beam, thereby allowing me to estimate the molecular gas mass of the entire galaxy, even though the beam in many cases only covers the circumnuclear central few kpc. I report a final CO(2-1) detection rate of 37.5% (6/16), and a CO(3-2) detection rate of 50% (4/8). For the detections, I determined their total velocity-integrated flux densities, CO line luminosities and the equivalent H_2 gas masses. I find an average CO luminosity of $L'_{\rm CO} = 4.35 \pm 1.09 \times 10^8 {\rm K\,km\,s^{-1}pc^2}$ with a standard deviation of $2.99 \times 10^8 {\rm K\,km\,s^{-1}pc^2}$ across the sample of 6 CO(2-1) detections. Additionally, I infer a mean molecular gas mass of $M(H_2) = 11.35 \pm 9.53 \times 10^8 M_\odot$ with a standard deivation of $2.19 \times 10^8 M_\odot$ by using a very conservative CO-to-H2 conversion factor of solar metallicity, as well as a line ratio $r_{21} = L'_{\rm CO(2\text{-}1)}/L'_{\rm CO(1\text{-}0)}$ found in the literature. For the non-detections I estimate informative 3σ-upper limits on the line flux, CO luminosities and H_2 gas masses. I compare with different studies that have also measured the CO luminosities and H_2 gas masses, as well as the Milky Way and our nearest neighbor, M31. I find that M31 has an overall lower molecular gas mass than the average value for my sample of AGN, and that the Milky Way contains roughly five times more molecular gas in the form of H_2 than the average molecular gas mass of my sample.

Despite the lack of spatial resolution in the single-dish observations, I investigate how much of this spatial information can be recovered (if at all), by developing a forward-model of the gas structure and kinematics of a typical spiral galaxy. The model effectively mimics a single-dish radio telescope observation of a mock galaxy, with a beam large enough to include all the gas. This has allowed me to simulate the distribution of gas in coordinate and velocity phase space and compare it with the observed data. I am able to partially extract some spatial kinematics that is folded into the global profile data from this model. I evaluate the performance of the model using the Affine Invariant Markov Chain Monte Carlo (MCMC) Ensemble sampler `emcee`. From my analysis of the gas motions using MCMC, I find that a simple model such as this is capable of producing emission line profiles similar to that we see in the data, and expect to see from theoretical considerations of the kinematics of rotating gas in disk galaxies.

Contents

1. Introduction

Galaxies are massive collections of stars, gas, dust and dark matter held together by gravity in single cohesive structures. They can harbor anywhere from a million to hundreds of trillions of stars. As of 2021, NASAs New Horizons space probe estimates the number of galaxies in the observable universe to be around 200 billion (Lauer et al. 2021). Nearly all large galaxies are thought to also contain supermassive black holes (SMBH) at their centers (Kormendy and Richstone 1995; Kormendy and Ho 2013). There are many different types of galaxies, with a wide range of morphologies and characteristics. According to the Galaxy Zoo project[1], spiral galaxies make up about two thirds of all massive galaxies, whilst around one third are ellipticals, and a few percent merging galaxies.

The galaxies in my sample (described in more detail in Section 2.1), all contain an AGN. AGNs are the most luminous persistent sources of radiation in the Universe, and are powered by accretion onto a SMBH. The central AGN component consists of a SMBH surrounded by an accretion disk of material, and is typically highly variable and very bright compared to the rest of the galaxy (Peterson 1997). In the same plane as the accretion disk, there is a torus of dense gas and dust. This torus is opaque to most forms of radiation, and only the most energetic X-rays are able to penetrate the torus (Sparke and Gallagher 2007). It is believed that most galaxies have gone through an AGN phase, which has played a crucial role in their formation and evolution (Kormendy and Ho 2013). Before we go on, let us review (in the context of this project) the relevant basics of galaxies, and how to observe the gas in them.

Spiral galaxies take their name from the extended spiral arms that wind around in a thin disk. Spiral galaxies comprise a central bulge or spheroidal component and a very flattened disk that extends to a large distance from the centre (Sparke and Gallagher 2007). The Andromeda Galaxy shown in the center panel of Fig. 1.1 is an example of a typical spiral galaxy.

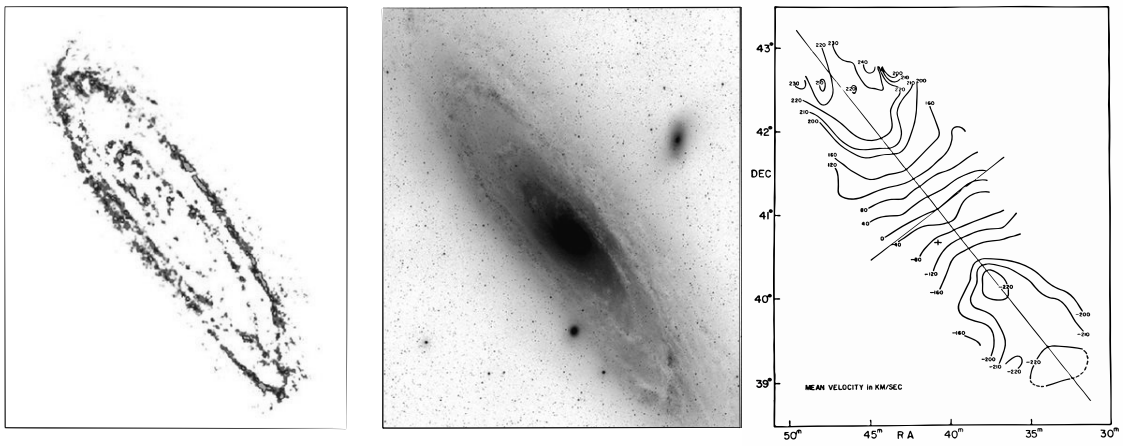

Fig. 1.1: Left: Distribution of cold gas (CO) in the Andromeda Galaxy (M31). Source: Nieten et al. (2006). Center: Optical image of M31. The bright center, prominent bulge and tightly wrapped spiral arms in the disk are clearly visible. Source: Tautenburg Observatory. Right: Radial velocity contours of atomic hydrogen in M31. Source: Argyle (1965). In all images: north is up, east is left.

[1] `https://www.zooniverse.org/projects/zookeeper/galaxy-zoo`

Most of the gas of a spiral galaxy is found in the disk. This gas consists of both cool atomic (HI) and molecular (H_2) hydrogen. The left panel of Fig. 1.1 shows the emission of Carbon Monoxide (CO) tracing dense molecular gas in M31. The gas is located in the disk, and congregates in the vicinity of the spiral arms. This reservoir of gas in a galaxy is directly linked to the process of star formation, as it makes up the raw material out of which new stars are born. The cold molecular gas component of spiral galaxies is of special interest in this project. In particular, the two main properties that describe the cold molecular gas in the disk, which are relevant to know about in the context of this project are (1) the surface brightness profile of the disk, and (2) the kinematics of the gas in the disk:

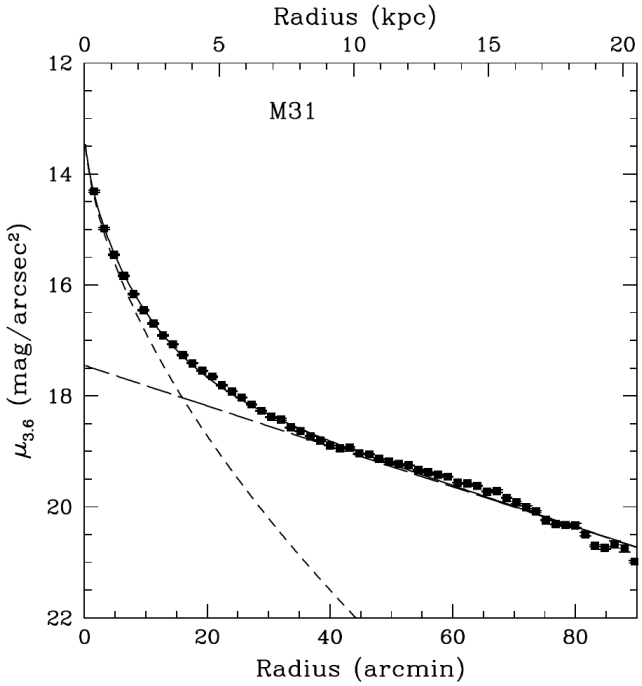

Fig. 1.2: Spitzer 3.6 µm surface brightness profile of M31 with decomposition into bulge and disk components. The bulge has been fitted with a Sérsic model (dashed line), and the disk has been fitted with an exponential model (long dashed line). Source: Seigar et al. (2008).

Surface photometry and the examination of surface brightness profiles is an important step in the identification of the various components of a galaxy and determining their masses. In fact, because a mass-luminosity relation M/L exists, it is possible to infer the mass of a galaxy from its luminosity alone. Because this luminosity varies from the centre to the edge of galaxies, and to a lesser extent from one galaxy to another, kinematic observations are required to determine the true mass distribution of galaxies. The surface brightness is a measure for the flux coming from each square arcsecond of the galaxy, expressed as an apparent magnitude (mag arcsec^{-2}). The surface brightness of a disk depends on the angle i (defined as the angle between the normal of the disk and our line of sight) at which we see it. Assuming optically thick emission (which is often the case for CO (Sparke and Gallagher 2007)), if the disk is seen edge-on (i.e., $i = 90°$), a given surface area will emit less strongly as more matter is tilted into view, causing the front layer to act as an opaque barrier preventing radiation to escape from behind it (self-shielding). In practice, we can correct to what we would observe if M31 had been face-on, and then find the average surface brightness $I(R)$ at distance R from the center.

Theoretically, the surface brightness profile of a disk galaxy is a combination of the

central bulge and the extended disk. In the stellar disk, when averaged over features like spiral arms, the surface brightness $I(R)$ often follows an exponential of the form (e.g., Sparke and Gallagher (2007))

$$I(R) = I_0 \exp(-R/h_R) \tag{1.1}$$

where I_0 is the intensity at the center (where $R = 0$) and h_R is the so-called scale length, a characteristic length that tells us at what radius the intensity of light has decreased by a factor e. The surface brightness of the bulge is often approximated by Sérsic's formula

$$I(R) = I_0 \exp\left[-(R/h_r)^{1/n}\right] \tag{1.2}$$

which in the case where the so-called Sérsic index $n = 1$, will tend toward the disk-model in Eq. (1.1). If $n = 4$, it is the "de Vaucoleurs formula", which describes the distribution of light in elliptical galaxies. In fact, the properties of bulges in disk galaxies closely resemble elliptical galaxies (Sparke and Gallagher 2007). Fig. 1.2 shows the surface brightness profile of M31, which has been fit with both a Sérsic model, and an exponential model, for the bulge and disk, respectively.

The dynamics of spiral galaxies appears to be well understood; nevertheless away from their centers their rotation velocity does not decrease as one would expect, whereas the light of the stars does. This has been attributed to the presence of dark matter: particles that barely interact with ordinary baryonic matter and radiation, except through gravity. Close to 80% of the mass of the universe is hidden from view if this is the case (Sparke and Gallagher 2007). Fig. 1.3 shows the rotation curve of M31. Without the contribution of a dark matter halo (shown by the dotted line), this curve would not be as flat as observations suggest.

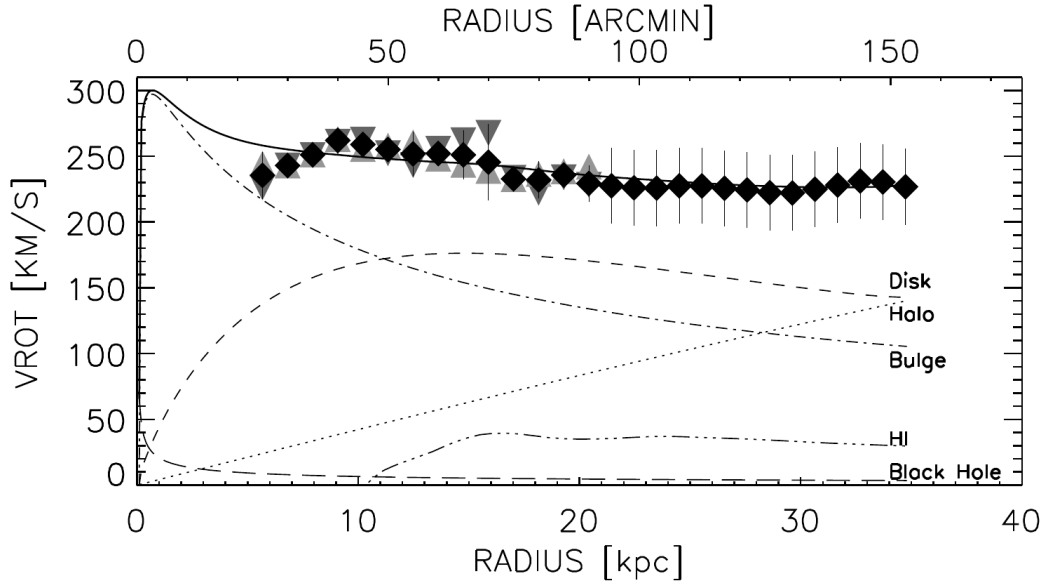

Fig. 1.3: Rotation Curve and mass model for M31. The solid line is the best fit to the data (diamonds). Between 20 and 35 kpc, the rotation curve is nearly flat at a velocity of $\sim 226\,\mathrm{km\,s^{-1}}$. Source: Carignan et al. (2006).

While motion of gas in a spiral galaxy does have a smaller random component (from local gravitational perturbations), the predominant energy of motion is by far ordered rotation

around the center. Observationally, all we can detect from this motion is the radial velocity V_r toward or away from us (using the Doppler effect). Because the random velocity component is negligible, it is safe to assume that at radius R from the center, a gas cloud follows a circular path with speed $V(R)$. Let us look at a flat disk of gas rotating around an axis z, tilted at an angle i, as shown in figure 1.4. The position of any gas cloud in the disk can be specified by its radial distance from the center R and azimuth ϕ, measured in the disk from the kinematic major axis AB lying perpendicular to our line of sight. The radial velocity V_r of such a cloud of gas is

$$V_r(R, i) = V_{\rm sys} + V(R) \sin i \cos \phi \tag{1.3}$$

where $V_{\rm sys}$ is the systemic velocity, or the velocity of the galaxy as a single system moving relative to us (Sparke and Gallagher 2007).

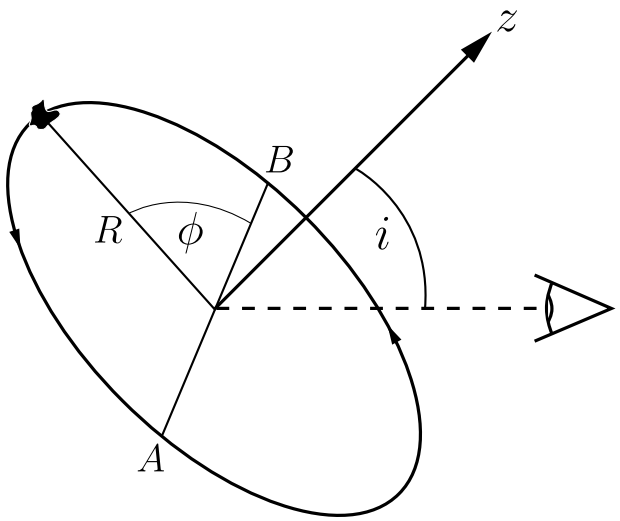

Fig. 1.4: A rotating disk with its normal tilted at an angle i relative to the line of sight of an observer. The inclination is defined such that a galaxy seen face-on has an inclination $i = 0°$ and a galaxy seen edge-on has $i = 90°$. The position of a gas cloud in the disk plane is specified by its radius from the center R and azimuth ϕ.

For a galaxy seen at inclination $i = 0°$ (i.e., face-on), we would not be able to measure any radial motion at all, since the gas would be moving in a plane perpendicular to our line of sight. On the other hand, a galaxy seen edge-on allows us to measure the true peak of the rotation curve, since all of the gas is moving in a plane parallel to our line of sight. If you connect points with the same value of $V(R) \cos \phi$ in contours of constant V_r, you can make a so-called "spider diagram" like that of M31 in the right panel of Fig. 1.1. The kinematic major axis AB in Fig. 1.4 shown by the central contour line perpendicular to the $V = 0$ velocity contour, is the azimuth where V_r deviates the most from $V_{\rm sys}$. The minor axis (perpendicular to AB), has to be joined with the isovelocity $V = V_{\rm sys}$, the axis of symmetry of the spider diagram. In the central regions of the galaxy, the contours are thus parallel to the minor axis. Further out, where the rotation speed is nearly constant at $\sim 226\,{\rm km\,s^{-1}}$ (Fig. 1.3), the contours run radially away from the center. If $V(R)$ begins to decrease, the contours close in on themselves. This is roughly what we see in the spider diagram of M31.

If you integrate all the flux from the gas across a galaxy, and measure how much there is at each velocity, you can construct a so-called global profile of the gas. Fig. 1.5 shows the integrated global profile of atomic gas (HI) for M31. Because a large portion of the gas

lies at radii where $V(R)$ is nearly constant at $\sim 226\,\mathrm{km\,s^{-1}}$ (Fig. 1.3), most of the emission is crowded into two peaks near the extreme velocities. If you imagine shifting the x-axis such that it is centered at $V = 0$, the peaks are roughly located at $\pm$220-230 $\mathrm{km\,s^{-1}}$. The separation of the peaks W represents the observed range of the smallest and largest velocities relative to the systemic velocity, and is (Sparke and Gallagher 2007)

$$W \approx 2V_{\mathrm{max}} \sin i \tag{1.4}$$

where V_{max} is the peak rotation speed of the galaxy (i.e., the highest point of the rotation curve). So by measuring the width of the profile, you can estimate the peak rotation velocity of the galaxy, without the need for detailed high-resolution observations of the gas. As the observations that comprise my sample of AGN are global profiles of the CO gas, being able to measure the peak velocity of a rotation curve that I have no knowledge of a priori, is quite useful. How exactly I intend to make use of these observations is described in more detail in Section 1.1.

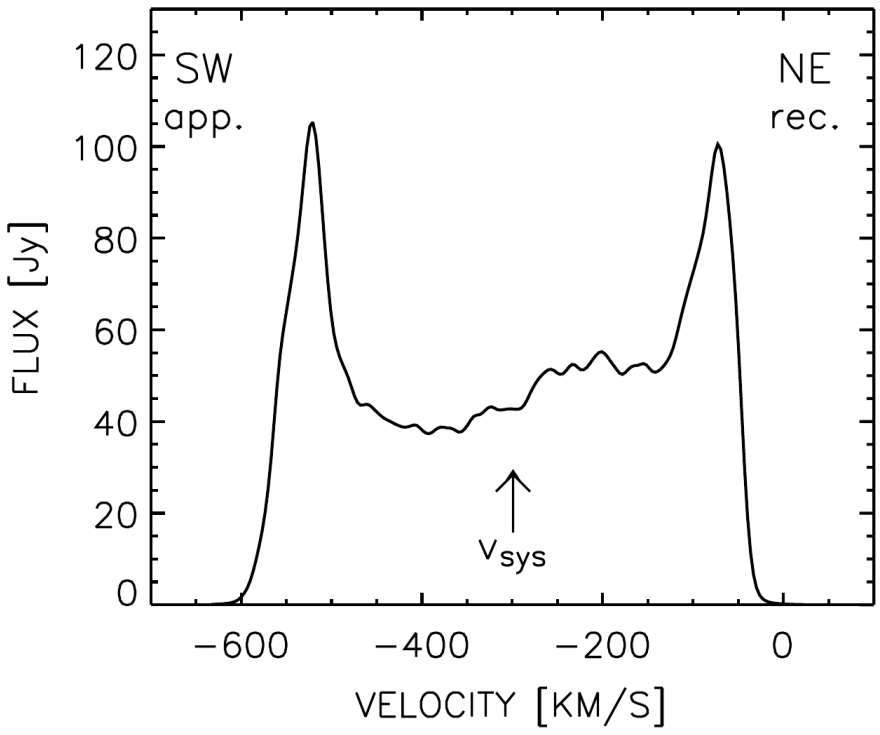

Fig. 1.5: HI integrated profile of M31. The absolute difference between the systemic velocity V_{sys} and the extreme velocities roughly equals the constant velocity of $226\,\mathrm{km\,s^{-1}}$ in the rotation curve between 20 and 35 kpc (Fig. 1.3) Source: Chemin et al. (2009).

1.1 Scientific focus

Molecular gas is a crucial component in the interstellar medium (ISM) as the formation of stars occur exclusively within molecular clouds. Therefore, it is essential to understand the properties of molecular gas to investigate galaxies and their evolution. Carbon monoxide (^{12}CO, hereafter CO) is the most abundant molecule after molecular hydrogen, and is the most commonly employed tracer of interstellar molecular gas, thanks to its low-J transitions

at millimetre wavelengths that are easily excited down to gas temperatures of $T \sim 10\,\mathrm{K}$ (Carilli and Walter 2013). Previous studies of CO have been done for local interacting (ultra)-luminous infrared galaxies ((U)LIRGS; Solomon et al. (1997); Lu et al. (2017); Mashian et al. (2015)), local high-M_* (Leroy et al. 2009) and low-M_* (Cicone et al. 2017) star-forming galaxies. Recently, Ramakrishnan et al. (2019) did a study of the morphology and kinematics of molecular gas in seven nearby AGN using ALMA to detect the CO(2-1) transition.

My project is highly motivated by the opportunity to use data from the ESO/APEX-Sub-mm-telescope to study the molecular gas in nearby galaxies with an actively accreting black hole. This data are in the form of global CO(2-1) and CO(3-2) profiles. Because these observations are single-dish observations, none of the gas is spatially resolved (as all of it is integrated across the beam). Despite this, it may be interesting to investigate how much of this spatial information can be recovered (if at all), by developing a forward-model of the gas structure and kinematics of a typical spiral galaxy. Such a model effectively mimics a single-dish radio telescope observation of a mock galaxy, with a beam large enough to include all the gas. This would allow me to simulate the distribution of gas in coordinate and velocity phase space and compare it with the data. I may be able to partially extract some of the original spatial information that is folded into the global profile data. The results of this analysis may further allow me to investigate potential differences between active galaxies and galaxies with a quiescent black hole.

2. Observations

2.1 Source sample

The source sample consists of 17 nearby galaxies with an actively accreting black hole. These objects have APEX observations of the CO(2-1) or CO(3-2) rotational transitions. Table 2.1 provides an overview of the source sample and some basic information.

The APEX telescope is ideal for high sensitivity observations, as a result of the typically low amounts of precipitable water vapour at Llano de Chajnantor, where the telescope is located. With its 12 meter diameter dish, APEX can cover a large fraction of a galaxy in a single pointing. The 17 sources were observed over four observation programs: E-097.B-0604A, E-097.B-0757A, E-098.B-0152A and E-099.B-0049A (PI Vestergaard[1]). The APEX observation log is shown in table 2.2.

Table 2.1: Overview of the AGN sample and their basic properties.

Galaxy name	RA[(a)] (h:m:s)	DEC[(b)] (°:′:″)	z[(c)]	D_L[(d)] (Mpc)	i[(e)] (deg)	$d25$[(f)] (arcsec)
3C 120	04:33:11.1	+05:21:15.6	0.03301	149.6	65.1	45.51 ± 5.24
Ark 120	05:16:11.4	−00:08:59.4	0.03271	148.2	51.8	62.83 ± 7.23
Fairall 9	01:23:45.7	−58:48:20.8	0.04702	215.3	64.1	61.40 ± 5.65
IC 4329A	13:49:19.2	−30:18:33.9	0.01605	71.8	65.5	95.09 ± 6.57
Mrk 50	12:23:24.1	+02:40:44.8	0.02343	105.5	51.7	37.00 ± 5.96
Mrk 335	00:06:19.5	+20:12:10.5	0.02578	116.2	0.0	26.19 ± 18.70
Mrk 509	20:44:09.7	−10:43:24.5	0.03440	156.1	36.4	35.33 ± 9.76
Mrk 590	02:14:33.5	−00:46:00.0	0.02638	119.0	26.0	75.54 ± 6.96
NGC 2617	08:35:38.7	−04:05:17.6	0.01421	63.5	39.2	84.75 ± 23.42
NGC 3227	10:23:30.5	+19:51:54.1	0.00386	17.1	68.3	238.86 ± 16.50
NGC 3783	11:39:01.7	−37:44:19.2	0.00973	43.3	26.6	128.28 ± 8.86
NGC 4593	12:39:39.4	−05:20:39.3	0.00900	40.1	34.0	143.93 ± 9.94
NGC 5548	14:17:59.5	+25:08:12.4	0.01717	76.9	41.4	79.10 ± 7.28
NGC 6814	19:42:40.6	−10:19:24.5	0.00052	2.3	85.6	185.42 ± 8.54
PG 0844+349	08:47:42.4	+34:45:04.3	0.06400	296.6	–	–
PG 1229+204	12:32:03.6	+20:09:29.9	0.06301	291.8	36.2	20.80 ± 4.31
PG 2130+099	21:32:27.8	+10:08:19.2	0.06298	281.7	62.1	30.77 ± 4.96

[(a)] Right ascension in the J2000.0 epoch extracted from the NASA/IPAC Extragalactic Database (NED).[2]
[(b)] Declination in the J2000.0 epoch extracted from NED.
[(c)] Redshift extracted from NED.
[(d)] Luminosity distance according to the Cosmology ($H_0 = 67.8\,\mathrm{km\,s^{-1}Mpc^{-1}}$, $\Omega_\mathrm{M} = 0.308$, $\Omega_\mathrm{vac} = 0.692$).
[(e)] Inclination of the optical disk.
[(f)] Optical diameter as defined by the 25th magnitude isophote. I extracted both i and d_{25} from the Hyperleda database.[3]

[1] mvester@dark-cosmology.dk, DK, Dark Cosmology Centre, Niels Bohr Institute
[2] `https://ned.ipac.caltech.edu/`
[3] `http://leda.univ-lyon1.fr/`

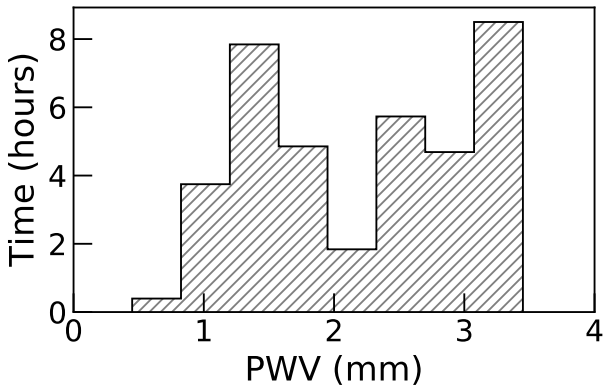

Fig. 2.1: Distribution of precipitable water vapour (PWV) conditions at the Chajnantor Plateau as measured by the APEX radiometer throughout the total 37.6 h of observations.

For the program E-097.B-0604A, 15 h of 345 GHz (SHeFI/APEX-1) was requested to detect the CO(3-2) line emission in the circumnuclear regions of a subset of five nearby AGNs from the AGN Watch Reverberation Mapping Database (Bentz and Katz 2015). for which the central gas contents are currently unknown. This database consists of ∼35 AGN that are located south of declination +30° such that they can be observed at reasonably high elevations with APEX to minimize atmospheric absorption. The sample was also limited to targets with redshifts of $z < 0.02$, such that the 18″ primary beam at ∼345 GHz measures only the flux within the inner few (1.5 to 6) kpc regions of the galaxy.

For the program E-098.B-0152A, 11.4 h of ∼230 GHz (SHeFI/APEX-1) was requested to detect the CO(2-1) line in the circumnuclear regions of three targets: NGC 3783, NGC 4593 and IC 4329A. These three targets are also part of the above-mentioned program E-097.B-0604A, for which the CO(3-2) line is observed by APEX. Having observations of both rotational transitions will provide constraints on the gas excitation levels, which in turn will lead to more accurate estimates of the molecular gas mass.

For the program E-099.B-0049, a total of 20.8 h was requested, split into 12.2 h of 230 GHz (SHeFI/APEX-1) for the CO(2-1) line, and 8.6 h of 345 GHz (SHeFI/APEX-2) for the CO(3-2) line in the circumnuclear regions of three targets: NGC 2617, MRK 50 and NGC 6814. They were selected for being relatively nearby, such that it is possible to obtain a stellar dynamical mass of the central black hole with the Very Large Telescope at a later time.

For the program E-097.B-0757, 36 h of 230 GHz (SHeFI/APEX-1) was requested to observe the CO(2-1) line. The 10 targets were selected to reside within the redshift range of $0.017 < z < 0.7$. The upper redshift cut-off was chosen so that any potential ALMA follow-ups would still be able to probe gas distributions at angular resolutions $\lesssim$150 pc. Since the CO(3-2) flux may be very weak for galaxies at those redshifts, this cut-off also keeps integration times modest. In the context of my project, the interesting thing about this program in particular—as opposed to the other three programs mentioned above—is that the lower redshift cut-off was chosen so that the ∼27″ beam at ∼230 GHz would cover at least ∼10 kpc in diameter. This allows a reasonable gauge of the gas mass of the entire galaxy, as opposed to just the inner few kiloparsecs.

All observations were made with the beam-switching mode, where a wobbling secondary rapidly switches positions between the target (ON) and a nearby position in the sky (OFF). Observations made in this mode—as opposed to position switching (moving the telescope)—are less sensitive to time dependent instabilities in the receivers and atmosphere. Needless to say, target sizes need to be smaller than the maximum throw of 5' for the secondary wobbler,

which is indeed the case for all targets in my sample.

2.2 APEX data reduction

I performed the data reduction using the GILDAS software package `CLASS`.[2] The data reduction pipeline I use is the standard procedure for APEX heterodyne instruments, and is outlined in the `CLASS` reduction script that accompanies the raw APEX data.

Most sources in the sample have multiple observations recorded at different times, sometimes months apart. Table 2.2 provides detailed information about each source and their corresponding constituent observations. The raw spectra delivered by the APEX real-time calibration software is in the corrected antenna temperature T_A^* scale. The corrections include atmospheric attenuation, forward efficiency and signal band gain.

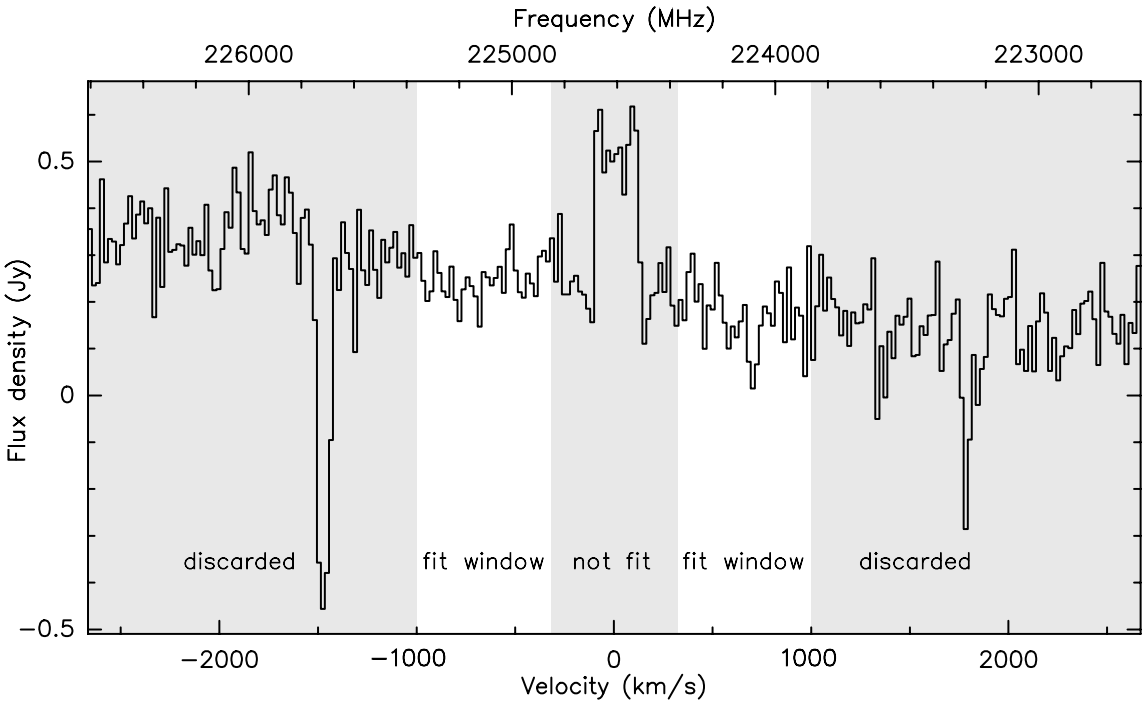

Fig. 2.2: Sample spectrum of the Mrk 590 CO(2-1) line - the average of two observations made on 27-05-2016 and 31-05-2016 shown in table 2.2. I converted the x-axis to units of velocity from frequency using the relativistic doppler-effect. The masked window and discarded regions are shown by the grey shadows.

I first converted the T_A^* to flux density (S_ν) scale using the Jansky to Kelvin conversion factor S_ν/T_A^*, which I extracted from the APEX Telescope Efficiencies page.[3]. The conversion factor can be approximated by $24.4\eta_f/\eta_a$ Jy/K, where η_f is the forward efficiency and η_a is the aperture efficiency. η_a intrinsically includes the effects due to error beams, blockage, spillover etc. because it is measured on sky toward a planet. The forward efficiency is the fraction of power in the forward beam of the feed. At this point I collected all the individual spectra belonging to observations targeting the same source (sometimes observed on different dates), and averaged them to produce a single, high S/N (Signal-to-noise ratio) and high

[2] `http://www.iram.fr/IRAMFR/GILDAS/`

[3] `http://www.apex-telescope.org/telescope/efficiency/`

resolution spectrum for each source. The averaging was done with weights proportional to the integration time, divided by the square of the system temperature ($w_i \propto t_{\rm int}/T_{\rm sys}^2$).

I then rebinned the resulting spectra to a velocity resolution of either $\sim$10 km s^{-1} or $\sim$20 km s^{-1} (depending on the width of the emission line) using a moving boxcar. (`SMOOTH BOX` function in `CLASS`).[4] Specifically, I rebinned NGC 6814 CO(2-1 & 3-2), NGC 2617 CO(2-1 & 3-2) and NGC 3783 CO(2-1) to $\sim$10 km s^{-1}. I rebinned the rest to $\sim$20 km s^{-1}. I found that this gave the best trade-off between noise and clarity of profile features. I completely discarded the 3C 120 observations from my analysis as they had very heavy baseline wiggles.

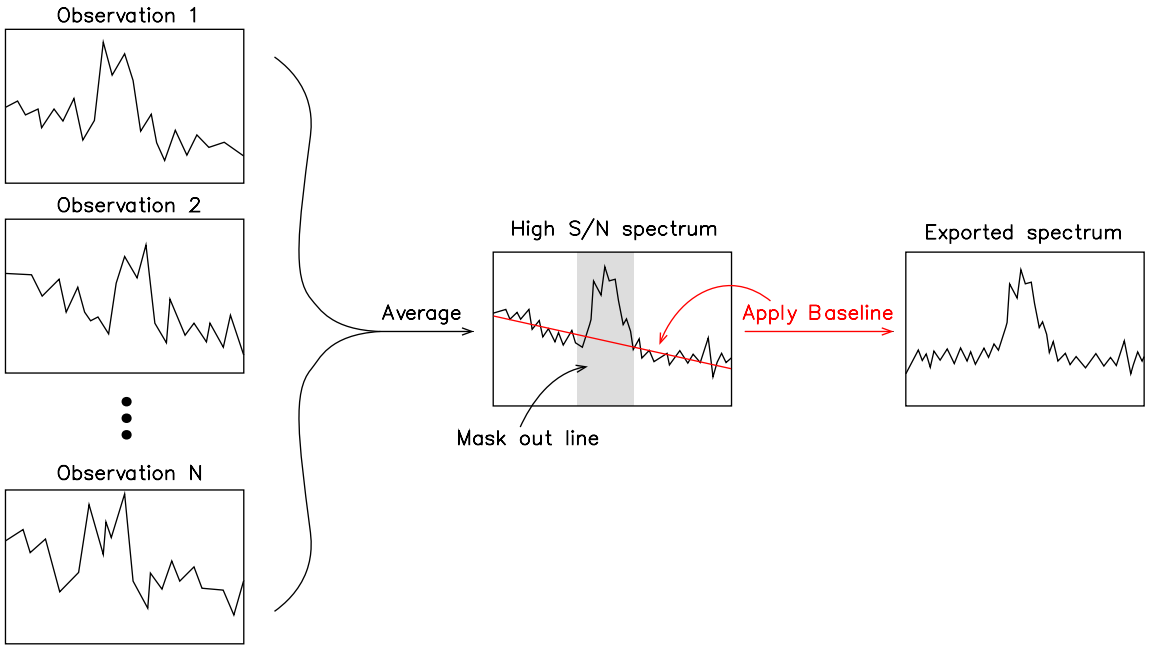

Fig. 2.3: Schematic showing the steps involved in reducing the APEX data. All individual spectra are first averaged to form a single spectrum. Next a first-degree polynomial baseline is subtracted, by only considering the regions outside the central $\pm$300 km s^{-1} shown by the grey shadow. The final spectrum is exported to .fits format for data analysis in Python.

For my analysis I extracted the region $v \in (-1000, 1000)$ kms^{-1} relative to the expected CO line center, and discarded everything outside of it (Fig. 2.2). This gives a clear view of the line profile, while retaining plenty of channels to ensure a reliable baseline subtraction. I then masked the region $v \in (-300, 300)$ km.s^{-1} (i.e. 300 km s^{-1} either side of the expected central velocity of the CO emission line), and performed a first-order polynomial baseline subtraction (Fig. 2.4). The spectrum after baseline subtraction is shown in Fig. 2.5. The typical reduction workflow is illustrated in Fig. 2.3. The final set of baseline-subtracted APEX CO(2-1) and CO(3-2) spectra, rebinned in bins of either $\delta v \approx 20$ km s^{-1} or $\delta v \approx 10$ km s^{-1}, depending on the width of the profile. The final exported spectra can be found in appendix A (Figs. A.1-A.23). The right panels show Digital Sky Survey (DSS) cutout images of the corresponding host galaxy.

[4] `https://www.iram.fr/IRAMFR/GILDAS/doc/html/class-html/node249.html`

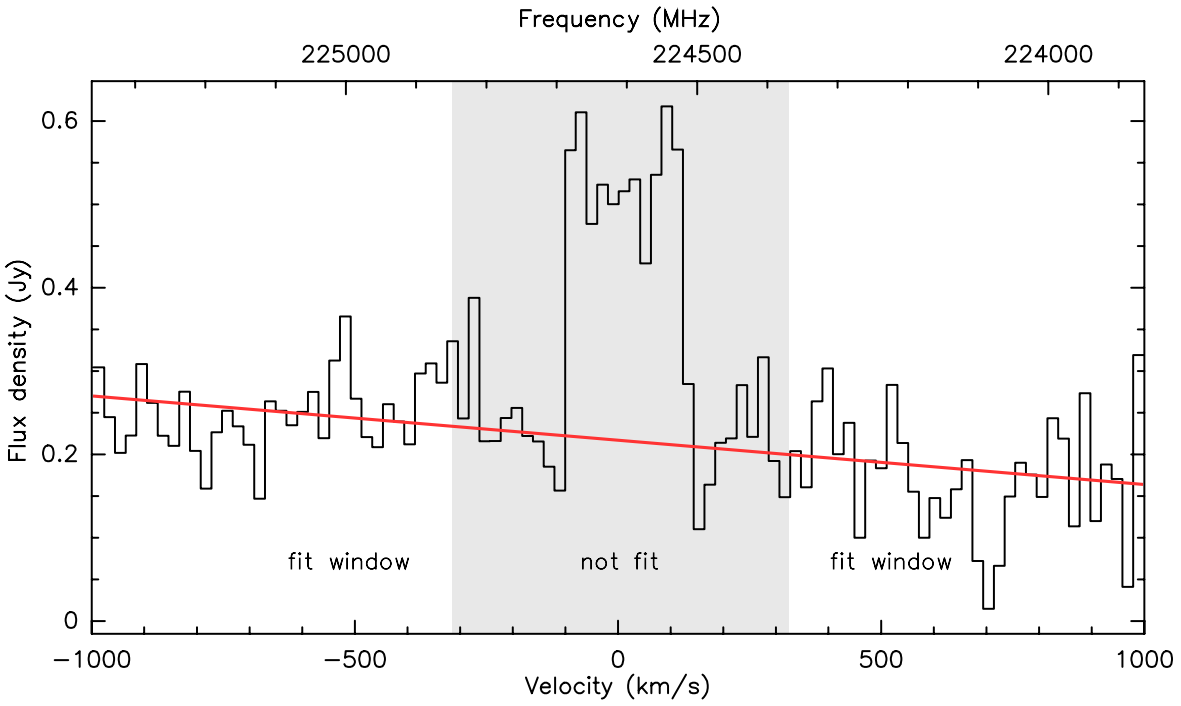

Fig. 2.4: The same spectrum from Fig. 2.2 with the discarded regions excluded. A first-degree baseline fit is shown by the red line. The masked window shown by the central grey shadow containing the line profile is not used in the fit.

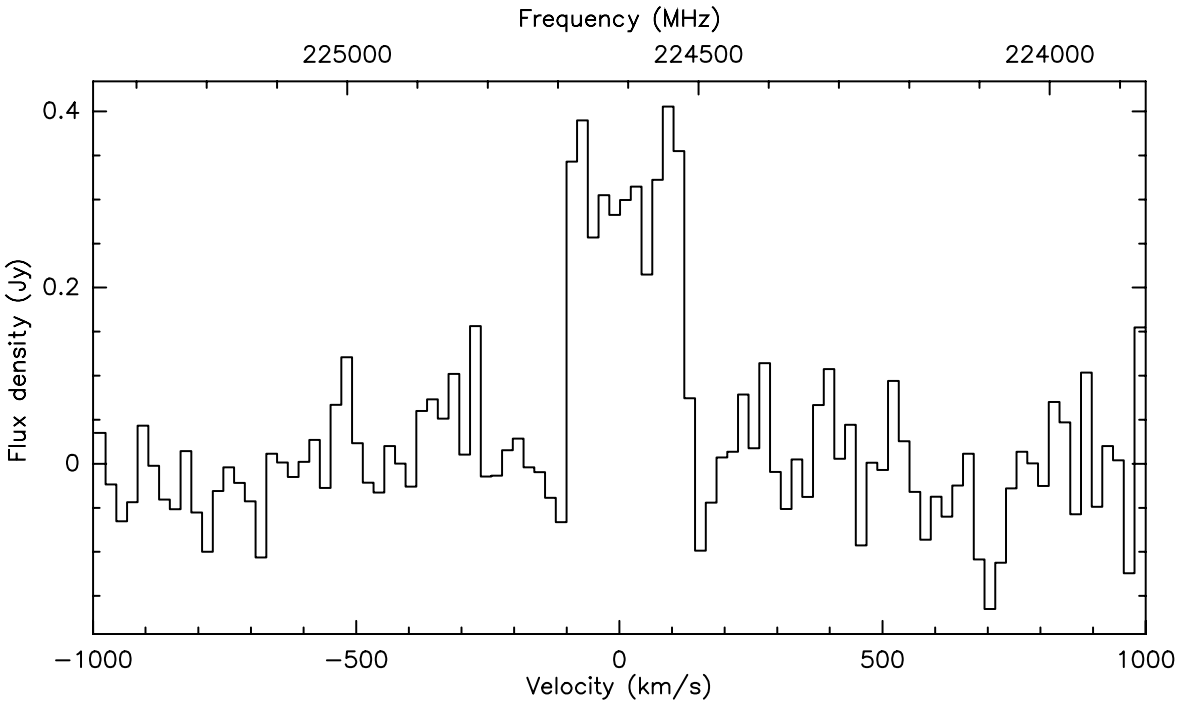

Fig. 2.5: The final spectrum rebinned to $\delta v = \sim 20\,\mathrm{km\,s^{-1}}$ after baseline subtraction.

Table 2.2: APEX observation log.

Program	Source	Line	Date (dd-mm-yy)	t_{ON}[a] (min)	PWV[b] (mm)
E-097.B-0604A	NGC3227	CO(3-2)	14-04-16	2.95	1.2 - 2.0
			15-04-16	11.75	1.4 - 1.7
			26-05-16	8.80	1.4 - 1.7
	NGC3783	CO(3-2)	14-04-16	26.4	1.2 - 2.0
	NGC4593	CO(3-2)	17-04-16	8.80	1.6 - 2.6
			26-05-16	11.80	1.4 - 1.7
	IC4329A	CO(3-2)	13-04-16	17.65	1.1 - 1.3
			31-05-16	20.55	2.0 - 2.3
			01-06-16	8.80	1.7 - 2.1
	NGC5548	CO(3-2)	13-04-16	14.70	1.1 - 1.3
			26-05-16	8.80	1.4 - 1.7
			27-05-16	14.70	1.3 - 1.5
			01-06-16	41.20	1.7 - 2.1
E-097.B-0757A	Mrk335	CO(2-1)	31-07-16	33.65	1.5
	Fairall9	CO(2-1)	06-04-16	24.15	3
			31-05-16	11.95	1.8 - 3.0
			31-07-16	4.85	1.5
			01-08-16	4.80	1.85
			07-08-16	19.15	2.6 - 3.0
	3C120	CO(2-1)	06-04-16	45.65	> 3
			12-04-16	7.20	3.2
			05-08-16	16.75	2.0 - 2.2
	Ark120	CO(2-1)	06-04-16	18.25	> 3
			08-04-16	33.45	3.0
			12-04-16	9.60	3.2
			13-04-16	16.85	1.8 - 2.0
	PG0844	CO(2-1)	08-04-16	21.15	1.9 - 4.8
			11-04-16	36.25	2.1 - 2.6
			12-04-16	3.00	2.1
	PG1229	CO(2-1)	08-04-16	63.00	1.9 - 4.8
			12-04-16	6.05	2.0
	NGC5548	CO(2-1)	08-04-16	42.30	1.9 - 4.8
	Mrk509	CO(2-1)	08-04-16	6.05	1.9 - 4.8
			27-05-16	31.25	3.0 - 3.9
			29-05-16	43.4	3.3 - 3.5
	Mrk590	CO(2-1)	31-05-16	14.35	1.8 - 3.0
			27-05-16	19.15	3.0 - 3.9
	PG2130	CO(2-1)	29-05-16	12.00	3.3 - 3.5

Table 2.2: Continued.

Program	Source	Line	Date (dd-mm-yy)	t_{ON}[a] (min)	PWV[b] (mm)
			31-05-16	38.45	1.8 - 3.0
			31-07-16	9.60	1.5
E-098.B-0152A	NGC3783	CO(2-1)	05-08-16	26.70	2.2-2.6
			04-12-16	26.50	1.0
	NGC4593	CO(2-1)	05-08-16	14.70	2.2-2.6
			09-08-16	17.65	0.9-1.1
			06-12-16	11.85	0.4-0.5
			07-12-16	29.35	1.0
			08-12-16	17.60	1.8-2.0
	IC4329A	CO(2-1)	05-08-16	23.60	2.2-2.6
E-099.B-0049A	NGC2617	CO(2-1)	25-04-17	18.00	1.3
		CO(3-2)	23-04-17	12.10	1.5
			25-04-17	18.05	1.3
			29-04-17	27.05	1.8
	MRK50	CO(2-1)	02-07-17	24.00	0.8-1.1
		CO(3-2)	30-06-17	3.00	1.5
			01-07-17	26.85	1.5
	NGC6814	CO(2-1)	29-06-17	5.95	2.5
		CO(3-2)	02-05-17	14.90	0.9
			30-06-17	21.00	1.2

[a] ON-source time.
[b] Precipitable water vapour as measured by the APEX radiometer during the integration time t_{ON}.

3. CO gas measurements

The cool, molecular gas content (which is mostly dominated by molecular hydrogen H_2) is a critical parameter in galaxy evolution, serving as the immediate fuel for star formation in galaxies. Because H_2 lacks a permanent dipole moment, the lowest rovibrational (rotation + vibration) transitions are forbidden and have excitation requirements that are significantly higher than the temperatures typically found in giant molecular clouds (which is where H_2 is most abundant). As a result, it is not easy to detect the H_2 gas mass directly; it needs to be measured indirectly through tracer molecules such as CO (the second most abundant molecule after H_2). In this chapter I will measure the total molecular gas in each galaxy of my sample, using the CO(2-1) and CO(3-2) observations as indirect tracers of H_2.

This chapter is outlined in the following way: In Section 3.1 I describe how I classify observations as detections vs. non-detections. In Section 3.2 I describe my method of calculating line widths. In Section 3.4 I discuss how I use the CO observations as a proxy, to estimate the total H_2 gas mass for every AGN in my sample. Finally, in section 3.5 I present my approach for correcting the values obtained in section 3.4 for flux falling outside the APEX telescope beam.

3.1 Classification of detections

To classify detections, I calculate the S/N ratio by dividing the velocity-integrated flux density (hereafter line flux) by its error and impose a S/N $>$ 5 cutoff. I calculate the velocity integrated flux density by adding up the flux contained in each channel belonging to the CO line $S_{\mathrm{CO,chan}}$ and multiplying by the channel width δv ($\approx 20\,\mathrm{km\,s^{-1}}$):

$$\int S_{\mathrm{CO}}\,\mathrm{d}v = \delta v_{\mathrm{chan}} \sum S_{\mathrm{CO,chan}} \tag{3.1}$$

The uncertainty on the total line flux is calculated by adding in quadrature the individual uncertainties in each channel. Specifically, because the rms noise in each channel $\sigma_{\mathrm{rms,chan}}$ is the same across all channels, the propagated error on the line flux is the square root of the number of channels in the range of summation N_{chan}, multiplied by the channel width and rms noise per spectral channel:

$$\sigma_{\int S_{\mathrm{CO}}\,\mathrm{d}v} = \sqrt{N_{\mathrm{chan}}}\delta v_{\mathrm{chan}}\sigma_{\mathrm{rms,chan}} \tag{3.2}$$

The S/N ratio is therefore given by

$$\mathrm{SNR} = \frac{\int S_{\mathrm{CO}}\,\mathrm{d}v}{\sigma_{\int S_{\mathrm{CO}}\,\mathrm{d}v}} = \frac{\sum S_{\mathrm{CO,chan}}}{\sqrt{N_{\mathrm{chan}}}\sigma_{\mathrm{rms,chan}}} \tag{3.3}$$

The range of summation should reflect the width an average CO line is expected to have: Cicone et al. (2017) found an average CO line width of $\Delta v_{\mathrm{line}} \sim \langle \mathrm{FWHM_{CO}} \rangle_{\mathrm{det}} = 160 \pm 91\,\mathrm{km\,s^{-1}}$ for their sample of 97 low-mass star-forming galaxies. Similarly, Cairns et al. (2019) found $\Delta v_{\mathrm{line}} \sim \langle \mathrm{FWHM_{CO}} \rangle_{\mathrm{det}} \sim 170\,\mathrm{km\,s^{-1}}$ for their sample of 72 star-forming galaxies from the Antlia galaxy cluster (They did not report a standard deviation nor include a table of line widths I could extract).

Based on these studies, I conservatively chose to integrate the flux density in the range of -300 to $+300$ $\mathrm{km\,s^{-1}}$ (relative to the line center). This initial threshold yielded 12

detections that passed the S/N > 5 test in total, as can be seen in Table 3.2. But, a couple of observations had to be handled separately and the original classification as detected or non-detected had to be re-evaluated: A visual inspection of the line profiles prompted me to reclassify the CO(3-2) NGC 5548 line as a detection (that was previously classified as a non-detection with S/N = 4.01), as there are some major troughs in the flux right around the expected location of the line, that underestimates the line flux, and consequently the S/N ratio (Fig. A.18). Additionally, I reclassified both the CO(2-1) Mrk 509 and CO(2-1) Fairall 9 lines as non-detections. While they both meet the S/N ratio requirements of a detection (5.86 and 6.06 respectively), they lack a coherent shape and can be mistaken for noise depending on the integration range (Figs. A.8-A.2). The final number of detections is 11, corresponding to a total detection rate of $\sim 52\%$ for all the CO observations.

3.2 Calculating line widths

I wrote software code in Python to calculate the FWHM of the emission lines of my sources. Given the large variety of emission line shapes in my sample, the software needed to be able to robustly find the FWHM of both single-peaked, double-peaked, and flat profile shapes as well as anything in between. It works like this:

The code finds the velocity channel $v_{\rm peak}$ with the highest flux density in the central -1000 to $+1000$ $\mathrm{km\,s^{-1}}$ region (relative to the center of the emission line). It the splits the spectrum into two parts: One part containing channels in the velocity range -1000 to $v_{\rm peak}$ (blue part), and the other part containing channels in the velocity range $v_{\rm peak}$ to $+1000$ $\mathrm{km\,s^{-1}}$ (red part). Starting with the left region (the blue region), the code then iterates through each channel (from left to right) until it finds the *first* channel with a flux density *higher* than half the maximum flux density. It then iterates over the same region, this time from right to left, until it finds the first channel with a flux density *lower* than half the maximum flux density. A linear function between the two channels found is then established. A precise velocity value is then found by evaluating this linear function at the half-maximum flux density value. The whole procedure is then repeated, this time for the other region (the red region) that was initially split at $v_{\rm peak}$. The velocity difference between the final two endpoints (on each side of the profile) is then taken to be the FWHM of the profile.

Using this software, I found the average FWHM line width of the 11 detections in my sample to be $\langle \mathrm{FWHM_{CO}} \rangle_{\rm det} = 198 \pm 86\,\mathrm{km\,s^{-1}}$, which is consistent with the studies mentioned above. The FWHM measurements for each galaxy in my sample are listed in Table 3.2.

As an added bonus, taking the middle value between the two endpoints found by the FWHM software, allows for a pretty robust determination of the central velocity of each profile. Because the emission lines are often not centered directly at $v = 0$ (as a result of imprecise redshift values), I can use this middle velocity value to manually shift each spectrum such that the line center is directly at $v = 0$ (or close to). This is not particularly important in the context of this chapter and the calculations I do in it, but it is very important when it comes to fitting the model I created (chapter 4) using MCMC algorithms (chapter 6.4.2).

3.3 Measuring the maximum gas velocity

I measured the maximum velocity of the CO gas for all detections using Eq. (1.4) described in Chapter 1:

$$V_{\rm max} \approx \frac{W}{2 \sin i}$$

where W is the separation of the peaks in the global profile. The inclination i is the angle between the disk normal and our line of sight. I extracted i from the Hyperleda database[1] (PG 0844+349 did not have an inclination listed, so I assumed $i = 45°$). I measured W in the following way: If the emission line profile had a clear double-horned shape, such as the CO(2-1) line in NGC 2617 (Fig. A.10) I measured the difference in velocity between the two peaks and took that to be W. In the case where the peaks could not be clearly identified, such as the CO(3-2) line in NGC 4593 (Fig. A.16) I measured the FWHM using the technique described in Section 3.2 and took that as the W. This is a tentative measurement; the FWHM values are possibly overestimating the true W, as I find that W tends to be smaller than the FWHM line width (for the double-horned profiles where a clear measurment of W was possible), by a factor 0.69 ± 0.13.

3.4 Determining molecular gas masses

In this Section I describe in detail my approach to determine the total molecular gas mass. In short, the process involves four steps: First I measure the total velocity-integrated flux density of the CO emission lines of every galaxy in my sample. Next I convert the flux densities into CO line luminosities. I then convert the CO(2-1) and CO(3-2) line luminosities into a CO(1-0) line luminosity, using line ratios found in the literature. Finally, I use this CO(1-0) line ratio to estimate the H_2 gas mass, through the assumption of a CO-to-H_2 conversion factor (also found in the literature):

To determine the total H_2 gas mass of the AGN in my sample, I first and foremost determined their total velocity-integrated line flux densities using Eq. (3.1) as described in Section 3.1. The difference now—as opposed to the fixed central $\pm 300\,{\rm km\,s^{-1}}$ region used in the classification process described earlier–is that a small integration range is preferable, as it reduces the error on the line flux. I found (by trial and error) that an integration range of $\pm 1.3 \times {\rm FWHM_{CO,source}}$ (with respect to the line center) yielded integration ranges narrow enough to reduce the influence of background noise, but wide enough to contain the entirety of the emission lines. The line fluxes calculated using Eq. 3.1 are listed in Table 3.2.

For non-detections, I estimate the 3σ upper limit on the total velocity-integrated line flux. Multiplying the denominator of Eq. (3.3) by 3, and using the fact that $N_{\rm chan} = \Delta v_{\rm line}/\delta v_{\rm chan}$, yields the upper limit

$$\int S_{\rm CO}\,{\rm d}v < 3\sigma_{\rm rms,chan}\sqrt{\delta v_{\rm chan}\Delta v_{\rm line}} \tag{3.4}$$

where $\Delta v_{\rm line}$ is the expected CO line width.

I assumed $\Delta v_{\rm line}$ equal to the average CO FWHM calculated using the CO lines classified as detections, that is $\Delta v_{\rm line} \sim \langle {\rm FWHM_{CO}} \rangle_{\rm det} = 198 \pm 86\,{\rm km\,s^{-1}}$.

[1] `http://leda.univ-lyon1.fr/`

I calculate the CO line luminosities for CO(2-1) and CO(3-2) from the velocity-integrated line flux densities, following the definition of Solomon et al. (1997):

$$L'_{\rm CO}[{\rm K\,km\,s^{-1}pc^2}] = 3.25\times10^7 \frac{D_L^2}{\nu_{\rm obs}^2(1+z)^3}\int S_{\rm CO}\,{\rm d}v \tag{3.5}$$

where D_L is the luminosity distance given in units of Mpc (listed in Table 2.1), $\nu_{\rm obs}$ is the observed frequency of the CO line in GHz. The velocity-integrated line flux $S_{\rm CO}$ is given in units of $\rm Jy\,km\,s^{-1}$. I chose to use $L'_{\rm CO}$ (expressed via the (areal) integrated source brightness temperature in units of $\rm K\,km\,s^{-1}\,pc^2$) and not $L_{\rm CO}$ (expressed as the source luminosity in $\rm L_\odot$), as the former is typically used in the translation of measured CO luminosities to $\rm H_2$ masses (Carilli and Walter 2013), which is what I intend to do in my analysis.

Typically the total molecular gas mass (dominated by $\rm H_2$) is estimated using the luminosity in the lowest energy CO(1-0) transition (as it is the most easily excited state, and therefore the most reliable estimate of CO gas mass across large regions of the ISM), through the assumption of a conversion factor $\alpha_{\rm CO}$ (Solomon et al. 1997). For the 15 galaxies in my sample that have CO(2-1) observations (detections and non-detections), I convert the $L'_{\rm CO(2\text{-}1)}$ values into $L'_{\rm CO(1\text{-}0)}$ estimates via the line ratio r_{21}:

$$r_{21} = \frac{L'_{\rm CO(2\text{-}1)}}{L'_{\rm CO(1\text{-}0)}}. \tag{3.6}$$

This ratio relates the CO(2-1) and CO(1-0) intrinsic brightness temperatures averaged over the source. Braine et al. (1993) found a r_{21} value of 0.89 ± 0.06 for their sample of 89 nearby spiral galaxies. Leroy et al. (2009) found $r_{21}\sim0.6-1.0$ for resolved observations of 18 local star-forming spirals. Aravena et al. (2014) found $r_{21}=0.70\pm0.16$, based on measurements of three massive star-forming disc galaxies at $z=1.5-2.2$. Following both Cicone et al. (2017) and Cairns et al. (2019), I adopt $r_{21}=0.8\pm0.2$, which is consistent with the aforementioned values. My justification for applying this ratio—that is ultimately based on (mostly) star-forming disc galaxies—to my sample of AGN hosts, comes from a recent study by Lu et al. (2017): They present evidence that the presence of an AGN influences only the very high J levels ($J>10$). As the CO transitions I am working with in this study are significantly lower than 10, I believe it is fair to assume that the AGN components of my sources are less important in the choice of r_{21}. Assuming local thermodynamic equilibrium (LTE) and optically thick gas, a ratio of $r_{21}=0.8$ corresponds to an excitation temperature of $T_{\rm ex}\sim10\,\rm K$.

The final step is to apply the CO(1-0) luminosity to $\rm H_2$ conversion factor (Carilli and Walter 2013),

$$M({\rm H_2}) = \alpha_{\rm CO} L'_{\rm CO(1\text{-}0)} \tag{3.7}$$

The value of $\alpha_{\rm CO}$ is still a topic of debate, but it is likely that it depends on metallicity and other local ISM conditions, including pressure, gas dynamics and metallicity—with increasing $\alpha_{\rm CO}$ as metallicity decreases. Bolatto et al. (2013) recommends a conservative $\alpha_{\rm CO}=3.3\pm2\,\rm M_\odot(K\,km\,s^{-1}pc^2)^{-1}$ in the disks of solar metallicity galaxies. I will adopt this value in my calculations. The justification for it is two-fold: (1) The galaxies in my sample are all spiral/disc galaxies. (2) The large uncertainty makes up for my lack of knowledge about the local ISM conditions in the disks (including metallicity), and will provide very conservative estimates of the ranges of $\rm H_2$ gas masses for the AGN in my sample.

For the eight galaxies in my sample that have CO(3-2) observations, a conversion factor r_{31} is needed:

$$r_{31} = L'_{\mathrm{CO(3\text{-}2)}}/L'_{\mathrm{CO(1\text{-}0)}} \tag{3.8}$$

Very recently and quite conveniently in the context of my study, Lamperti et al. (2020) found $r_{31} = 0.53 \pm 0.06$ for 36 nearby AGN hosts. As my sample of sources consist exclusively of AGNs, their r_{31} estimate is very pertinent in this context. I will apply this ratio and repeat the procedure described above to measure the H_2 gas mass, as derived from the CO(3-2) observations.

The calculated H_2 masses are listed in Table 3.3. All measurements made in this section relating to CO luminosities have been corrected for potential CO gas flux falling outside of the APEX beam, as described in Section 3.5.

3.5 Aperture correction

Because the APEX primary beam only covers the central few kpc of the majority of galaxies in my sample (chapter 2), any measurement of the line flux, CO line luminosity or H_2 gas mass, will inevitably be lower limits of the true values. It is therefore paramount that I correct for flux losses due to any potential CO emission lying outside the beam. I used the same technique as in Bothwell et al. (2014) to calculate a "beam coverage fraction". This fraction is the ratio between the flux falling inside the beam and the potential flux missing due to the beam being smaller than the CO emitting region. By taking into account the inclination of the galaxy optical disk, the method consists of integrating over the beam area of an exponential disk model for the CO emission. I calculate the scale length h_r using the relation that Young et al. (1995) and Leroy et al. (2009) derived from resolved CO(2-1) observations,

$$h_r[\mathrm{CO(2\text{-}1)}] = 0.2 \pm 0.05\, d_{25} \tag{3.9}$$

where d_{25} is the optical diameter of the galaxy. It is defined as the projected major axis of a galaxy at the isophotal level 25 mag arcsec^{-2} in the B-band. The value of $h_{r_{\mathrm{CO(2\text{-}1)}}}$ is technically only valid for CO(2-1) observations. As I was not able to find a similar relation for CO(3-2) in the literature, I adopted the same value for my CO(3-2) observations as well. As both transitions are from the same molecule, this assumption—to a first-order approximation—may not be completely unrealistic. As a result, the calculations related to the CO(3-2) beam corrections reported in this section, are tentative at best, as they inherently assume that the distribution of CO(2-1) and CO(3-2) are similar.

I extracted d_{25} for each galaxy in my sample from the Hyperleda database.[2] (except PG 1229+204, as it was unavailable). For each galaxy, I integrate its exponential disc model, described by Eq. (4.1), out to the radius covered by the 27″ or 18″ APEX beam at 230 GHz and 345 GHz, respectively. The flux that falls within the beam depends on the inclination i of the disk. If the disk is seen at an angle, the beam will pick up additional flux from the galaxy as the outer parts of the disk is tilted into view. For a galaxy seen face-on however, the gas in the outer parts of the disk—perpendicular to our line of sight—is hidden from view. The fraction of flux falling within the beam in this extreme situation, will be given by integrating a 2D exponential disc model out to the beam radius (relative to the total flux):

[2] `http://leda.univ-lyon1.fr/`

$$\text{Flux fraction} = \frac{\int_0^{2\pi} \int_0^{\text{Beam}} e^{-R/h_r} R \, \mathrm{d}r \, \mathrm{d}\theta}{\int_0^{2\pi} \int_0^{\infty} e^{-R/h_r} R \, \mathrm{d}r \, \mathrm{d}\theta}. \tag{3.10}$$

As the exponential disc model for the intensity is two-dimensional, the *total* flux (given by the double integral in the denominator) is integrated azimuthally from 0 to 2π, and radially from 0 to ∞. The flux falling within the beam (given by the double integral in the numerator) is likewise integrated azimuthally from 0 to 2π, but integrated radially from 0 to to the size of the telescope beam (given in arcseconds). The intensity at the center of the disk I_0 (Eq. (4.1)) is a constant, and cancels out in the ratio. As the inclination becomes bigger, more flux will fall inside the beam, and the solution will tend toward a 1D exponential model:

$$\text{Flux fraction} = \frac{\int_0^{\text{Beam}} e^{-R/h_r} \, \mathrm{d}r \, \mathrm{d}\theta}{\int_0^{\infty} e^{-R/h_r} \, \mathrm{d}r \, \mathrm{d}\theta} \tag{3.11}$$

The actual ratio is therefore a combination of these two extreme cases. Following Bothwell et al. (2014), I calculate a flux correction for each galaxy by taking a linear combination of both cases, with the relative contribution from each given by the inclination angle i:

$$F = \sin i \left(\frac{\int_0^{\text{Beam}} e^{-R/h_r} \, \mathrm{d}r \, \mathrm{d}\theta}{\int_0^{\infty} e^{-R/h_r} \, \mathrm{d}r \, \mathrm{d}\theta} \right) + (1 - \sin i) \left(\frac{\int_0^{2\pi} \int_0^{\text{Beam}} e^{-R/h_r} R \, \mathrm{d}r \, \mathrm{d}\theta}{\int_0^{2\pi} \int_0^{\infty} e^{-R/h_r} R \, \mathrm{d}r \, \mathrm{d}\theta} \right) \tag{3.12}$$

The beam corrections for each galaxy is shown in Table 3.3, along with the corrected line fluxes and CO luminosities.

3.6 Results of CO measurements

The calculated line fluxes, CO line luminosities and H_2 gas masses are listed in Tables 3.2 and 3.3. For non-detections, I list the 3σ-upper limits. Values corrected for potential CO flux falling outside the beam are indicated by the subscript "corr".

I extracted apparent maximum rotation velocities for the HI gas from the Hyperleda database, to compare with the directly measured CO $V_{\rm max}$ values. The result is shown in Fig. 3.1. Despite the limited number of sources in my sample, there still seems to be a direct correlation between the maximum velocities extracted from HI and CO gas. This suggests that the maximum velocity at which gas rotates in a galaxy is not all too different between atomic and molecular gas.

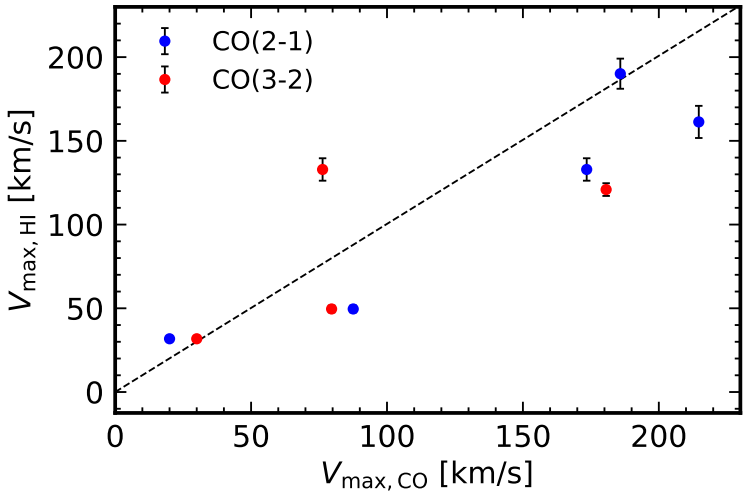

Fig. 3.1: $V_{\rm max,HI}$ vs $V_{\rm max,CO}$ maximum velocities. There is a clear correlation between the two, suggesting similar kinematics between the CO and HI gas. The blue and red points indicate the CO(2-1) and CO(3-2) transition used in the calculation of $V_{\rm max,CO}$. The dashed line indicates a 1:1 relationship.

Table 3.1: Basic CO measurements.

Galaxy name	$t_{\rm ON}$[a] (min)	rms[b] (mJy)	S/N[c] (fraction)	v_0[d] ($\mathrm{km\,s^{-1}}$)	FWHM[e] ($\mathrm{km\,s^{-1}}$)	$V_{\rm max}$[f] ($\mathrm{km\,s^{-1}}$)
APEX CO(2-1) observations						
3C 120	–	–	–	–	–	–
Ark 120	78.15	53.33	3.56	–	–	–
Fairall 9	64.90	58.84	6.06	–	–	–
IC 4329A	23.60	89.87	2.52	–	–	–
Mrk 50	24.00	80.09	0.01	–	–	–
Mrk 335	33.65	57.30	0.04	–	–	–
Mrk509	80.60	55.80	5.86	–	–	–
Mrk 590	33.50	61.38	11.67	+34.05	222.03	185.83
NGC 2617	18.00	59.84	17.20	−2.38	144.67	87.58
NGC 3227	–	–	–	–	–	–
NGC 3783	53.20	49.94	20.03	+13.19	130.03	268.13
NGC 4593	91.15	34.97	46.12	+11.43	310.09	214.70
NGC 5548	42.30	55.78	19.55	−42.61	231.76	173.46
NGC 6814	5.95	207.45	8.24	−24.91	76.24	20.00
PG 0844+349	60.40	61.92	0.24	–	–	–
PG 1229+204	69.05	50.24	1.94	–	–	–
PG 2130+099	59.05	53.33	3.55	–	–	–
APEX CO(3-2) observations						
3C 120	–	–	–	–	–	–
Ark 120	–	–	–	–	–	–
Fairall 9	–	–	–	–	–	–
IC 4329A	47.00	103.24	3.91	–	–	–
Mrk 50	29.85	160.61	0.76	–	–	–
Mrk 335	–	–	–	–	–	–
Mrk509	–	–	–	–	–	–
Mrk 590	–	–	–	–	–	–
NGC 2617	57.20	97.46	8.37	+28.56	149.31	79.62
NGC 3227	23.50	160.82	80.61	+34.20	335.43	180.62
NGC 3783	26.40	171.04	0.82	–	43.17	–
NGC 4593	20.60	146.40	13.48	+16.28	311.51	274.55
NGC 5548	79.40	92.67	4.01	+0.66	183.98	76.30
NGC 6814	35.90	133.58	9.18	+7.49	93.18	30.01
PG 0844+349	–	–	–	–	–	–
PG 1229+204	–	–	–	–	–	–
PG 2130+099	–	–	–	–	–	–

[a] On-source integration time.
[b] 1σ spectral rms calculated in channels of $\delta v \approx 20\,\mathrm{km\,s^{-1}}$.
[c] Signal-to-noise ratio calculated using Eq. (3.3).
[d] Central velocity of the CO emission line with respect to the redshift in Table 2.1. This shift in velocity was found using the FWHM software described in Section 3.2.
[e] The FWHM line width of the emission line.
[f] The peak velocity of the CO gas inferred using Eq. (1.4).

Table 3.2: CO measurements.

Galaxy name	$\int S_{\rm CO}\,{\rm d}v$[a] ($\rm Jy\,km\,s^{-1}$)	$L'_{\rm CO}$[b] ($10^8\,\rm K\,km\,s^{-1}pc^2$)	$L'_{\rm CO(1\text{-}0)}$[c] ($10^8\,\rm K\,km\,s^{-1}pc^2$)	$\rm M(H_2)$[d] ($10^8\,\rm M_\odot$)
APEX CO(2-1) observations				
3C 120	–	–	–	–
Ark 120	< 10.23	< 1.330	< 1.06	< 3.47
Fairall 9	< 11.41	< 3.089	< 2.47	< 8.06
IC 4329A	< 17.05	< 0.529	< 0.42	< 1.38
Mrk 50	< 15.29	< 1.017	< 0.81	< 2.65
Mrk 335	< 10.96	< 0.882	< 0.71	< 2.30
Mrk509	< 10.72	< 1.544	< 1.24	< 4.03
Mrk 590	76.54 ± 6.12	6.459 ± 0.517	5.17 ± 1.36	16.86 ± 11.22
NGC 2617	118.51 ± 6.19	2.881 ± 0.150	2.31 ± 0.59	7.52 ± 4.98
NGC 3227	–	–	–	–
NGC 3783	95.22 ± 3.90	1.081 ± 0.044	0.86 ± 0.22	2.82 ± 1.87
NGC 4593	179.88 ± 4.42	1.751 ± 0.043	1.40 ± 0.35	4.57 ± 3.02
NGC 5548	116.98 ± 6.13	4.160 ± 0.218	3.33 ± 0.85	10.86 ± 7.20
NGC 6814	153.22 ± 11.69	0.005 ± 0.000	0.00 ± 0.00	0.01 ± 0.01
PG 0844+349	< 12.06	–	–	–
PG 1229+204	< 9.80	< 4.802	< 3.84	< 12.53
PG 2130+099	< 10.87	< 4.961	< 3.97	< 12.95
APEX CO(3-2) observations				
3C 120	–	–	–	–
Ark 120	–	–	–	–
Fairall 9	–	–	–	–
IC 4329A	< 21.18	< 0.292	< 0.15	< 0.50
Mrk 50	< 31.10	< 0.919	< 0.49	< 1.59
Mrk 335	–	–	–	–
Mrk509	–	–	–	–
Mrk 590	–	–	–	–
NGC 2617	92.19 ± 8.57	0.996 ± 0.093	0.53 ± 0.08	1.72 ± 1.08
NGC 3227	1421.74 ± 132.4	1.125 ± 0.105	0.60 ± 0.09	1.95 ± 1.22
NGC 3783	< 30.93	< 0.156	< 0.08	< 0.27
NGC 4593	154.62 ± 19.46	0.669 ± 0.084	0.35 ± 0.06	1.16 ± 0.73
NGC 5548	103.61 ± 12.11	1.637 ± 0.191	0.87 ± 0.14	2.83 ± 1.79
NGC 6814	112.76 ± 9.50	0.002 ± 0.000	0.00 ± 0.00	0.00 ± 0.00
PG 0844+349	–	–	–	–
PG 1229+204	–	–	–	–
PG 2130+099	–	–	–	–

[a] Total velocity-integrated flux density of the CO line profile. The uncertainties listed are calculated using the denominator of Eq. (3.3). For the non-detections, I list the 3σ-upper limit on the total integrated CO flux density derived using Eq. 3.4.

[b] CO line luminosity calculated from Eq. (3.5). For non-detections, I list the 3σ-upper limit on the CO line luminosity.

[c] CO(1-0) line luminosity calculated from Eq. (3.6) (for CO(2-1) observations) and Eq. (3.8) (for CO(3-2) observations). For non-detections, I list the 3σ-upper limit on the CO(1-0) line luminosity.

[d] Molecular hydrogen mass, calculated assuming a constant $\alpha_{\rm CO}$ appropriate for disks of solar metallicity galaxies. For CO(2-1) observations, $\rm H_2$ gas masses are calculated using the ratio $r_{21} = 0.8 \pm 0.2$. For CO(3-2) observations, $\rm H_2$ gas masses are calculated using the ratio $r_{31} = 0.55 \pm 0.06$. For the non-detections, I list the 3σ-upper limit on the $\rm H_2$ mass.

Table 3.3: Beam-corrected CO measurements.

Galaxy name	$F^{(a)}$ (fraction)	$\int S_{\mathrm{CO,corr}}\,\mathrm{d}v^{(b)}$ ($\mathrm{Jy\,km\,s^{-1}}$)	${L'_{\mathrm{CO,corr}}}^{(c)}$ ($10^8\,\mathrm{K\,km\,s^{-1}pc^2}$)	${\mathrm{M}(\mathrm{H_2})_{\mathrm{corr}}}^{(d)}$ ($10^8\,\mathrm{M_\odot}$)
APEX CO(2-1) observations				
3C 120	–	–	–	–
Ark 120	0.83 ± 0.085	< 12.31	< 1.601	< 4.18
Fairall 9	0.87 ± 0.07	< 13.19	< 3.571	< 9.32
IC 4329A	0.73 ± 0.09	< 23.41	< 0.726	< 1.90
Mrk 50	0.95 ± 0.04	< 16.03	< 1.066	< 2.78
Mrk 335	0.96 ± 0.10	< 11.36	< 0.914	< 2.39
Mrk509	0.94 ± 0.06	< 11.35	< 1.635	< 4.27
Mrk 590	0.67 ± 0.11	115.00 ± 24.19	9.704 ± 2.041	25.33 ± 17.56
NGC 2617	0.68 ± 0.15	174.67 ± 40.19	4.247 ± 0.977	11.09 ± 7.76
NGC 3227	0.41 ± 0.08	–	–	–
NGC 3783	0.45 ± 0.10	212.09 ± 51.69	2.408 ± 0.587	6.29 ± 4.43
NGC 4593	0.45 ± 0.10	401.86 ± 88.87	3.911 ± 0.865	10.21 ± 7.11
NGC 5548	0.71 ± 0.10	163.70 ± 26.24	5.821 ± 0.933	15.19 ± 10.33
NGC 6814	0.52 ± 0.09	296.36 ± 68.27	0.010 ± 0.002	0.03 ± 0.02
PG 0844+349	–	–	–	–
PG 1229+204	0.99 ± 0.01	< 10.93	< 4.829	< 12.60
PG 2130+099	0.98 ± 0.02	< 9.99	< 5.055	< 13.19
APEX CO(3-2) observations				
3C 120	–	–	–	–
Ark 120	0.69 ± 0.10	–	–	–
Fairall 9	0.74 ± 0.09	–	–	–
IC 4329A	0.58 ± 0.10	< 36.53	< 0.504	< 0.87
Mrk 50	0.87 ± 0.08	< 35.88	< 1.061	< 1.83
Mrk 335	0.86 ± 0.21	–	–	–
Mrk509	0.84 ± 0.11	–	–	–
Mrk 590	0.49 ± 0.11	–	–	–
NGC 2617	0.52 ± 0.15	177.28 ± 59.32	1.915 ± 0.641	3.31 ± 2.34
NGC 3227	0.30 ± 0.07	4799.33 ± 1861.34	3.799 ± 1.606	6.57 ± 4.94
NGC 3783	0.31 ± 0.08	< 98.87	< 0.499	< 0.86
NGC 4593	0.32 ± 0.08	486.05 ± 224.78	2.102 ± 1.046	3.64 ± 2.90
NGC 5548	0.56 ± 0.10	186.04 ± 52.24	2.940 ± 0.818	5.08 ± 3.46
NGC 6814	0.38 ± 0.08	293.32 ± 87.98	0.004 ± 0.001	0.01 ± 0.01
PG 0844+349	–	–	–	–
PG 1229+204	0.96 ± 0.04	–	–	–
PG 2130+099	0.93 ± 0.05	–	–	–

[a] Fraction of expected total CO flux recovered by the $27''$ and $18''$ beams for the CO(2-1) and CO(3-2) transitions, respectively. They are calculated using Eq. (3.12). The CO(3-2) beam fractions are tentative, as they are calculated using the CO(2-1) specific disk scaling length from Eq. (3.9).

[b] Total velocity-integrated flux density of the CO line profiles, corrected for beam coverage. For the non-detections, I list the beam-corrected 3σ-upper limit on the total integrated CO flux density.

[c] CO line luminosity calculated from Eq. (3.5), corrected for beam coverage. Non-detections are listed as the 3σ-upper limit on the CO line luminosity.

[d] Molecular hydrogen mass, calculated assuming a constant α_{CO} appropriate for disks of solar metallicity galaxies, and corrected for CO flux falling outside the APEX beam. For CO(2-1) observations, $\mathrm{H_2}$ gas masses are calculated using the ratio $r_{21} = 0.8 \pm 0.2$. For CO(3-2) observations, $\mathrm{H_2}$ gas masses are calculated using the ratio $r_{31} = 0.55 \pm 0.06$. For the non-detections, I list the 3σ-upper limit on the $\mathrm{H_2}$ mass.

4. A model of the CO global profile

4.1 Introduction

To acquire a deeper understanding of the kinematics of the cold gas in the AGN in my sample, I wrote software code for a simple model of the gas structure and kinematics in a typical AGN. The idea is to simulate a single-dish radio telescope observation of a toy galaxy, with a large enough beam that includes all the gas, in order to determine the distribution of gas in coordinate and velocity phase space. That is, how much of the gas possesses a given velocity relative to the systemic velocity of the galaxy. Each parcel of gas will provide its own contribution to the profile. When I integrate over the entire spatial distribution—as the APEX telescope does—then I obtain the global CO line profile. So the profile contains the original information—and the question is whether I'm able to extract this information again—or how much of the interesting information is lost (or retained) in this integration.

I will use a model to approximate the underlying physics responsible for producing the global profiles we see in practice, with a small, and hence manageable, number of adjustable parameters. Other than having a small number of parameters, a good model obviously needs to be a good match to the data, and is preferably also tied to the underlying physics. By adjusting the various parameters that I define, I can fit the model to my data. When there's a good match, the parameters will tell me something about the physics.

4.2 The model

In order to derive a model that approximates the CO emission line reasonably well, I need to consider both the motion of gas in the galaxy, as well as the emission from that gas. I therefore divide my model parameters into two categories: gas motion vs. gas emission.

4.2.1 Gas motion parameters

As mentioned in Chapter 1, most of the gas in spiral galaxies orbits around the galaxy center, but there are also smaller random motions superimposed on the large-scale rotation. The small random motions are not included in this model, as they are borderline insignificant at speeds typically around 8-10 $\mathrm{km\,s^{-1}}$. The model assumes a flat, circular disk of material, with its normal tilted at an angle i relative to our line of sight as shown in Fig. 4.1. The disk rotates according to some rotation curve that I specify. The model further assumes that the galaxy has a clear edge R_{max}. Real galaxies do not have a well-defined edge, but there is a radius at which the gas surface brightness tapers off quickly and does not contribute significantly to the total (integrated) emission. Because flux contributions of diffuse gas at large distances are negligible, I decided to include only the gas within R_{max} in the model.

To parametrize the motion of gas in the disk, I introduce the following parameters: V_{max}, b_0, V_1, V_2 and V_3. The maximum velocity V_{max}, is the peak velocity of the rotation curve. Observing a galaxy edge-on ($i = 90°$) would allow us to measure the "true" peak of the rotation curve, since all of the gas is moving in a plane parallel to our line of sight. For anywhere in between 0° and 90°, V_{max} can be found using Eq. (1.4).

The break point b_0 (measured in units of $\mathrm{R_{max}}$) is the radius where the rotation curve transitions from its initial linear ascent to become more or less constant. The three velocities

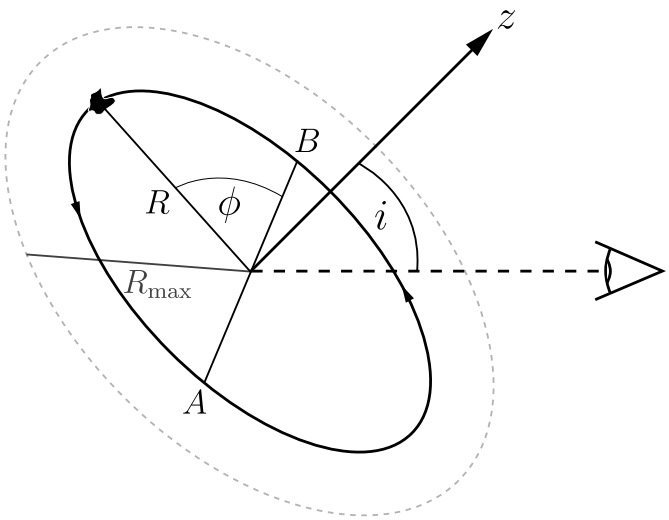

Fig. 4.1: A rotating disk with its normal tilted at an angle i relative to the line of sight of an observer. The inclination is defined such that a galaxy seen face-on has an inclination $i = 0°$ and a galaxy seen edge-on has $i = 90°$. The position of a gas cloud in the disk plane is specified by its radius from the center R and azimuth ϕ. The grey dashed ellipse shows the edge of the galaxy $R_{\max}$.

V_1, V_2 and V_3 are the speeds at which gas moves, at positions $0.5\,\mathrm{R_{max}}$, $0.75\,\mathrm{R_{max}}$ and $1\,\mathrm{R_{max}}$ from the center of the disk, respectively. They have the freedom to move vertically on the rotation curve, thereby altering the slopes of the linear segments at radii greater than b_0. I chose to limit b_0 in the range $0 < b_0 \leq 0.5$, since in practice we do not see rotation curves that flatten out at distances greater than half the radius of the galaxy (Kauffmann et al. 2015). Because $V_{\max}$ is the highest velocity in the disk, V_1, V_2 and V_3 can never assume a value higher than $V_{\max}$. Table 4.1 provides an overview of all the rotation curve parameters. They are also illustrated visually in the left panel of figure 4.2.

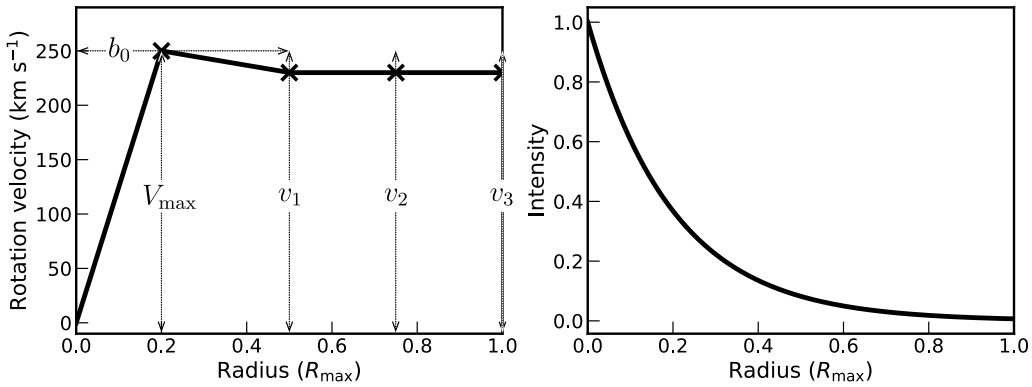

Fig. 4.2: Left: An example of a rotation curve consisting of four separate linear segments connected by the parameters $V_{\max} = 250\,\mathrm{km\,s^{-1}}$, $b_0 = 0.2\,\mathrm{R_{max}}$, and $V_1 = V_2 = V_3 = 230\,\mathrm{km\,s^{-1}}$. The horizontal and vertical dotted lines indicate the parameter limits. Right: The intensity curve constructed from the parameters $I_0 = 1$ and $h_r = 0.2\,\mathrm{R_{max}}$ in Eq. 4.1.

Table 4.1: Overview of the seven core parameters and their defined limits. The first five parameters are responsible for modifying the rotation curve. The last two exclusively affect the intensity of light throughout the disk.

Parameter	Limits	Description
$V_{\max}$	$0 < V_{\max} \leq 600\,\mathrm{km\,s^{-1}}$	The peak velocity of the rotation curve.
b_0	$0 < b_0 \leq 0.5\,\mathrm{R_{max}}$	The break point in the rotation curve that separates the initial. steep climb from the flat part
V_1	$0.8\,V_{\max} < V_1 \leq 1\,V_{\max}$	The rotation speed at $R = 0.5\,\mathrm{R_{max}}$.
V_2	$0.8\,V_{\max} < V_2 \leq 1\,V_{\max}$	The rotation speed at $R = 0.75\,\mathrm{R_{max}}$.
V_3	$0.8\,V_{\max} < V_3 \leq 1\,V_{\max}$	The rotation speed at $R = 1.0\,\mathrm{R_{max}}$.
I_0	$0 < I_0$	The intensity at $R = 0$.
h_r	$0.1 < h_r < 0.3\,\mathrm{R_{max}}$	The scale length; the radius at which the intensity has decreased by a factor e.

4.2.2 Gas emission parameters

The model also needs to take into account the emission of light from the cold gas, since that obviously affects the observed flux. The two parameters, I_0 and h_r (table 4.1), determine how the emission intensity $I(R)$ varies with R. I assume $I(R)$ follows an exponential of the form

$$I(R) = I_0 \exp(-R/h_r) \tag{4.1}$$

where I_0 is the intensity at the center (where $R = 0$), and h_r is the so-called scale length, a characteristic length that tells us at what radius the intensity of light has decreased by a factor e. I assume that the gas density is directly proportional to the emission intensity. The plot on the right-hand side of figure 4.2 shows an example where $I_0 = 1$ and $h_r = 0.2\,\mathrm{R_{max}}$.

4.3 Constructing the model

I divided the model galaxy from which the global profile is inferred, into sections that each have distinct velocity, intensity and area values. Geometrically speaking, I divided the circular disk into a number of equidistant annuli, each with a width dR. I then further subdivided the annuli azimuthally into a number of angular segments with widths $d\phi$. The parameters dR and $d\phi$ together determine how finely the disk is partitioned. Programatically speaking, the sections are indexed by incrementing anti-clockwise through the sections of the first annulus, then moving outward to the next annulus and so on. This overarching index k describes a section as a whole and starts at 0. See the left panel of figure 4.3 for a simple, but instructive example where $d\phi = 45^\circ$ and $dR = 1/3\,\mathrm{R_{max}}$.

My ultimate goal is to calculate the flux and radial velocity in every single section of the disk. Given the discrete nature of the problem, choosing which value to use for R and ϕ in the calculation of V_r can be a little ambiguous. To eliminate any bias, I chose to take the average between R_i and R_{i+1}, as well as the average between ϕ_j and ϕ_{j+1}, and use those middle values $R_{\mathrm{mid}} = \frac{1}{2}(R_i + R_{i+1})$ and $\phi_{\mathrm{mid}} = \frac{1}{2}(\phi_j + \phi_{j+1})$ as the exact position where I define and compute the radial velocity $V(R)$ and intensity. The indices i and j are different from k in that they increment only radially and azimuthally, respectively. For example, a

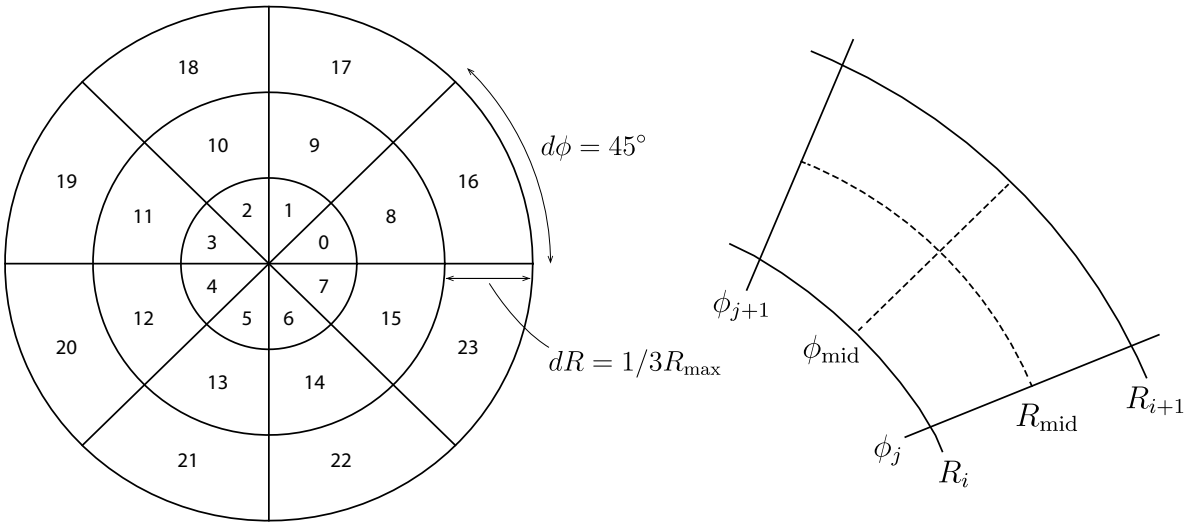

Fig. 4.3: Left: A simple example of a galaxy disk divided into 24 sections, as determined by dR and $d\phi$. The index k is incrementing counter-clockwise from 0 to 23. Right: A close-up of a single section, to show $R_{\rm mid}$ and $\phi_{\rm mid}$ used in the model calculations.

$k = 2$ section is also identified by the indices $i = 0$ and $j = 2$. The right panel of figure 4.3 shows a close-up of a single section. Assuming $V_{\rm sys} = 0$, the radial velocity in a given disk-section is therefore

$$V_{r,k}(R_{{\rm mid},i}) = V(R_{\rm mid}) \sin i \cos \phi \tag{4.2}$$

I assume the flux in any given section is proportional to both the area and intensity of that section:

$$F_k = A_k I_k(R_{\rm mid}) \tag{4.3}$$

This essentially means that the intensity at $I = I(R_{\rm mid})$ is uniformly distributed across the area in each section. If gas is distributed evenly in the disk, a larger section (with a bigger area) contains more gas, and consequently emits more light. The area A of any given annulus (enclosed by the radii R_i and R_{i+1}) is

$$A_k[\text{Annulus}] = \pi \left(R_{i+1}^2 - R_i^2\right)$$

The number of sections each annulus is divided into is $2\pi/d\phi$. So the area of a single section is therefore the total area of the annulus divided by the number of sections in that annulus:

$$A_k[\text{Section}] = \frac{\pi \left(R_{i+1}^2 - R_i^2\right)}{2\pi/d\phi} = \frac{1}{2} d\phi \left(R_{i+1}^2 - R_i^2\right)$$

The intensity of light in any given section at some radius $R_{{\rm mid},i}$ is given by

$$I_k(R_{\rm mid}) = I_0 \exp(-R_{\rm mid}/h_r) \tag{4.4}$$

All area, intensity, and radial velocity values are each stored in separate arrays, each indexed by k. This allows easy removal or modification of individual sections if needed, as any index can easily be accessed in this manner. All that's left to do is integrate the flux

over the whole galaxy (i.e., integrate azimuthally over ϕ and radially over R), and display it as a function of line-of-sight velocity, in a velocity resolution that matches the observed data.

To check if the model does what I expect, I made simulations. I predicted what the global profile and spider-diagram would look like based on a rotation curve that rises steeply and then flattens out (left and right panels of figure 4.4). I expect the contours in the central region of the spider-diagram to be parallel to the minor axis (the axis perpendicular to AB in figure 4.1), as a result of the linearly increasing part of the rotation curve between $R = 0$ and $R = 0.2R_{\rm max}$. I also expect the constant velocity at radii greater than $R = 0.2R_{\rm max}$ (Figure 4.4, middle panel) to produce contours that move radially away from the center (Figure 4.4, right panel). This is indeed what the simulation shows.

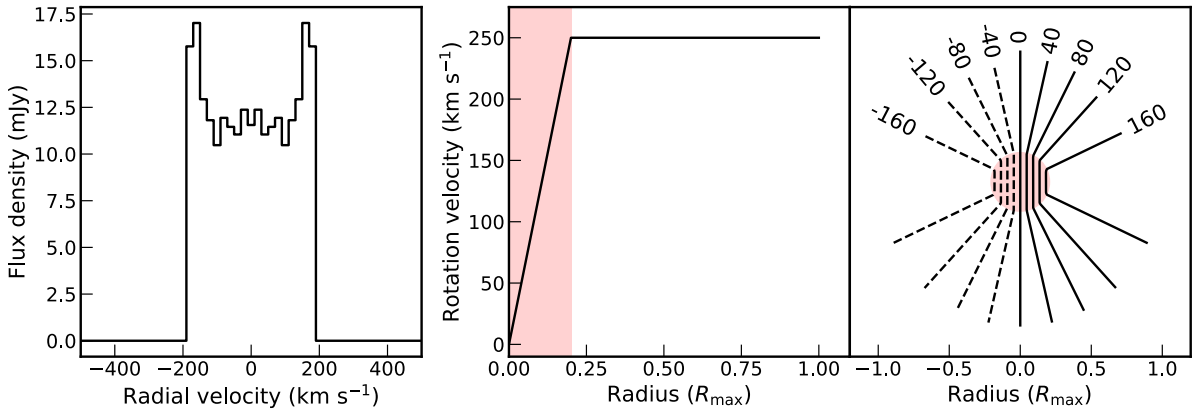

Fig. 4.4: Left: The simulated global profile of a galaxy tilted at an angle $i = 45°$, with $V_{\rm max} = 250$ km s^{-1}, $b_0 = 0.2R_{\rm max}$, $I_0 = 1$ and $h_r = 0.2R_{\rm max}$. Middle: The rotation curve. Right: Spider-diagram. Contours of constant V_r connect points with the same value of $V(R)\cos\phi$. The kinematic major axis shown by the central contour line where $V = 0$ is the azimuth where V_r deviates the most from $V_{\rm sys}$. The dashed contours indicate negative velocities (gas moving towards us). The pink shaded areas indicate regions of the galaxy inside the radius $0.2R_{\rm max}$.

4.4 Asymmetry parameters

The seven core parameters in the model are not capable of producing asymmetry in the profile, since the rotation curve and intensity profile are azimuthally invariant. The global profile is essentially symmetric around $V = 0$ km s^{-1}. This is a problem, because there are a number of sources in my sample that are clearly asymmetric. The way I try to solve this problem is to introduce an additional set of parameters, that have the power to alter the flux from one side of the galaxy.

I experimented with introducing a spiral structure in the distribution of gas, and having one or more spiral arms contribute less or more to the overall flux. However, introducing an extra set of parameters on top of the core parameters mentioned in the last section increases the complexity of an already complex model even further. So if the model can yield reliable fits without the addition of these extra parameters, then that is always preferred.

Instead of masking the flux in radial ranges of annuli, I tried to introduce masks in the shape of spiral arms. Because we see spiral structures in nature, a more intuitive solution

is to mimic density variations from real galaxies, by masking out flux in the general shape of spiral arms. Figure 4.5 shows that asymmetry can be achieved in this way. I did this by adding four new parameters responsible for modifying the spiral structure in different ways: S_{thick}; it determines the thickness of the masked spiral arms and is limited to $0 \leq S_{\text{width}} \leq 80$. The bigger this number is, the thicker the masked regions are. (note to self: change code so this is between 0 and 1 for brevity?) The second parameter is S_{bulge}. It determines the radius at which the spiral arms start to grow. It essentially insulates a circular part of the center from any masking effects. The third parameter is the asymmetry parameter S_{as}. It is a factor by which the thickness of one arm is increased, and the other decreased. Technically, the thickness of one arm is multiplied by S_{as} and the other is divided by it. It is limited to $0 < S_{\text{as}} \leq 2$. The last parameter is S_{flux}, limited to $0 \leq S_{\text{flux}} \leq 1$ and is, just like R_{flux}, a factor that simply modifies how much flux is allowed to pass through the masked regions. $S_{\text{flux}} = 0$ would completely block out the flux, while $S_{\text{flux}} = 1$ would cause the mask to be completely transparent and let all the flux through.

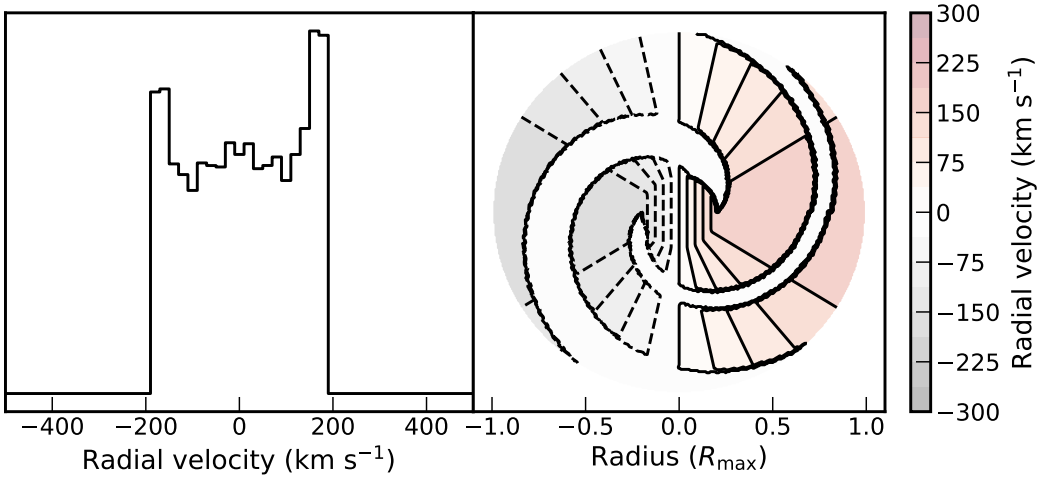

Fig. 4.5: Left: Global flux profile constructed from the same core parameter values as in figure 4.4, with the addition of spiral parameters $S_{\text{width}} = 50$, $S_{\text{bulge}} = 0.2R_{\text{max}}$, $S_{\text{as}} = 1.5$ and $S_{\text{flux}} = 0$. The profile has reduced flux at the negative peak, because the mask filtered out more flux from the left side than the right. Right: Spider-diagram of the model. The spiral mask overlayed on top is purely for visualization purposes; it does not alter the radial velocity of gas at the position, only the flux amplitude.

Table 4.2: Overview of the spiral parameters.

Parameter	Limits	Description
S_{thick}	$0 \leq S_{\text{width}} \leq 1$	The thickness of the spiral mask
S_{bulge}	$0 \leq S_{\text{bulge}} \leq 1$	The size of the central bulge unaffected by the spiral mask
S_{as}	$0 < S_{\text{as}} \leq 2$	A factor by which the thickness of one arm is increased, and the other decreased.
S_{flux}	$0 \leq S_{\text{flux}} \leq 1$	A factor that modifies how much flux passes through the spiral mask

5. Model simulations

To get a feel for the flexibility and limitations of the model, I experimented with changing the parameter values to see the impact on the line profile. I find that changing a single parameter can actually have a significant impact on the shape of the emission line profile. It is not trivial to predict which parameter to tweak to obtain a certain profile change, so I will focus on a single parameter at a time, and keep every other parameter fixed.

In the following, I have fixed $V_{\rm max} = V_1 = V_2 = V_3 = 250$ km s^{-1} , $b_0 = 0.2R_{\rm max}$, $I_0 = 1$ and $h_r = 0.2R_{\rm max}$. The radial velocity $V_{\rm max}$ and inclination i are degenerate, since changing either of them has the same qualitative effect on the width of the profile, via the relation $W = 2V_{\rm max} \sin i$. Because of this degeneracy, and the fact that I do not a priori know what the actual inclination of my sources are, I adopt a value of 45° for the inclination in these experiments.

This combination of parameters produces the global profile shown in the left panel of figure 4.4, and will serve as the baseline that I compare profiles to as I change individual parameters throughout this section. I am purposefully not showing the flux scale on the y-axis in these figures because the shape of the line profile is the more important information.

5.1 Core parameters

If I increase $V_{\rm max}$, I expect the width of the global profile to increase as well. This evolution is exactly what we see in figure 5.1. The total flux does not change, so the peak flux values should be higher when $V_{\rm max}$ is small, and lower when it is bigger. As $V_{\rm max} \to 0$, the emission line becomes extremely narrow and the double-horn shape is lost.

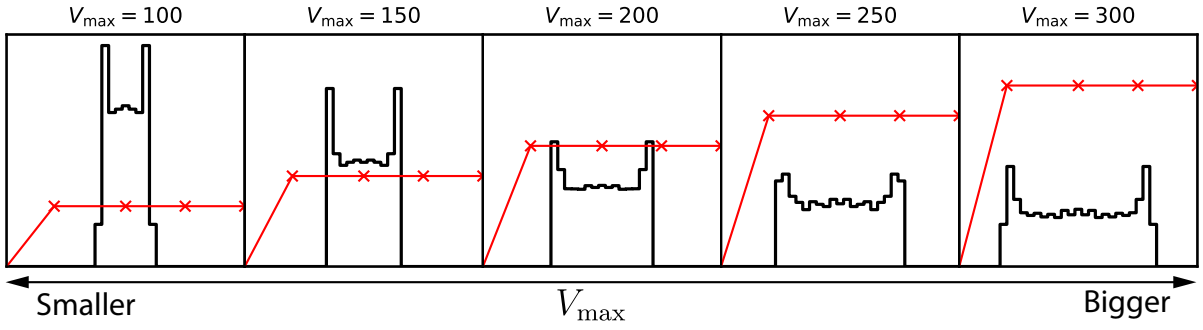

Fig. 5.1: Illustration of how the shape of the global profile changes when $V_{\rm max}$ is increased. Note that because $V_1 = V_2 = V_3 = V_{\rm max}$, the flat part of the rotation curve is essentially moving up and down as $V_{\rm max}$ is changed.

When it comes to tweaking b_0, increasing its value from 0 to $0.5R_{\rm max}$ has a significant effect on the ratio between the flux at the central and extreme velocities. As b_0 increases, the flux gradually migrates inward from the extreme velocities toward the center. When b_0 is small, the flux at the extreme velocities is huge in comparison to the flux at the center ($V = 0$), as shown in figure 5.2. As b_0 changes from 0 to $0.5R_{\rm max}$, the double-horn profile morphs into a centrally peaked profile. In the case where $b_0 = 0.5R_{\rm max}$, all the gas at $R > 0.5R_{\rm max}$ rotate at the peak velocity. However, because the emission intensity in the outer regions is very small, the flux contribution is also very small.

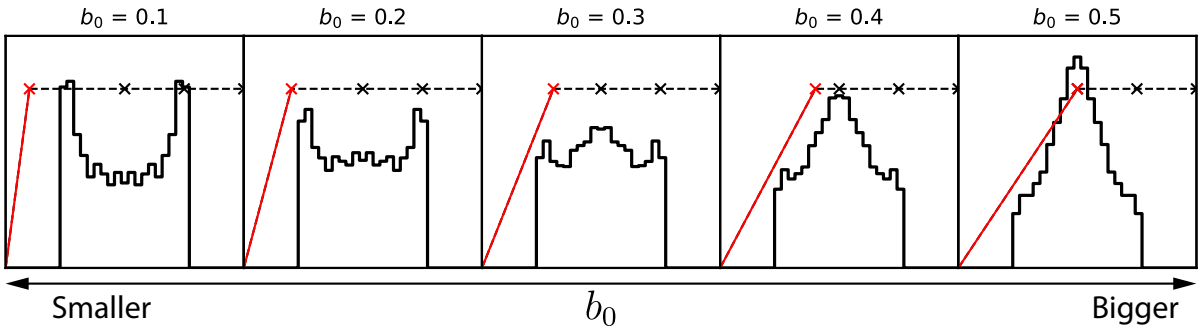

Fig. 5.2: Illustration showing the evolution of the global profile as b_0 changes. The dotted black line shows the rotation curve, and the red line highlights the part of the rotation curve directly affected when b_0 is tweaked.

When I change either of the velocities V_1, V_2 and V_3, the shape of the global profile changes in predictably: In general, V_1 is going to have the strongest effect on the profile since it is closer to the center of the galaxy where the emission intensity is higher (Eq. 4.1). The effect is less for V_2 and even less for V_3. Decreasing V_1 to 50 kms^{-1} as shown in figure 5.3 effectively removes a large portion of gas that rotates at $V_{\rm max}$, so most of the emission is crowded at the center forming a peak. There's still a small double-horn profile at the very top, with a very small width compared to the overall width of the profile. This is a result of the oddly shaped rotation curve, where most of the emission is centered at $V = 0$, but a significant amount still rotates at speeds slightly higher than $V = 0$. The triangular shape of the overall flux also means that there's still gas moving at $V_{\rm max}$, but not a lot. When V_1 increases, the shape approaches a double-horn profile.

Altering V_2 affects the profile in similar ways that V_1 does: Modifying the velocity of gas farther out where the emission intensity of that gas is weaker, consequently results in less of an impact on the shape of the line profile. In contrast to V_1, there is no triangular shape in the case where $V_2 = 50$ km s^{-1}. This is expected, because the gas inside $R = 0.5R_{\rm max}$ emits light at a much higher intensity than gas at larger radii. What is especially interesting to note here, is that I have the ability to produce a nearly flat-topped profile with the right combination of parameters.

Decreasing the value of V_3 decreases the orbital velocity of gas at $R = 1R_{\rm max}$. Since the emission intensity is negligible at the very edge of the galaxy, the effect is noticeably muted in comparison to the effects of V_1 and V_2.

Let's now play with the scale length of the galaxy h_r, and see how the global profile responds. The illustration in figure 5.4 shows the appearance of the global profile when increasing h from $h_r = 0.05R_{\rm max}$ to $h_r = 0.25R_{\rm max}$. When the scale length is extremely small, most of the intensity comes from the very center of the disk. The result is a centrally peaked profile. Increasing the scale length rapidly causes the flux to migrate into two peaks near the extreme velocities. If the rotation curve (not shown on the figure) were to rise linearly throughout the whole disk, we would see a centrally peaked profile, no matter what value h_r assumes. The reason for that is, if the rotation curve rises linearly throughout the whole disk, then the only parts of the disk that are actually rotating at $V_{\rm max}$ (or close to it), are the parts at the very edge of the galaxy. So while a large value of h_r raises the intensity at larger radii slightly, it is just not enough to compete with a linearly increasing rotation curve that indirectly amplifies the flux at lower velocities, and dimninishes flux at higher velocities.

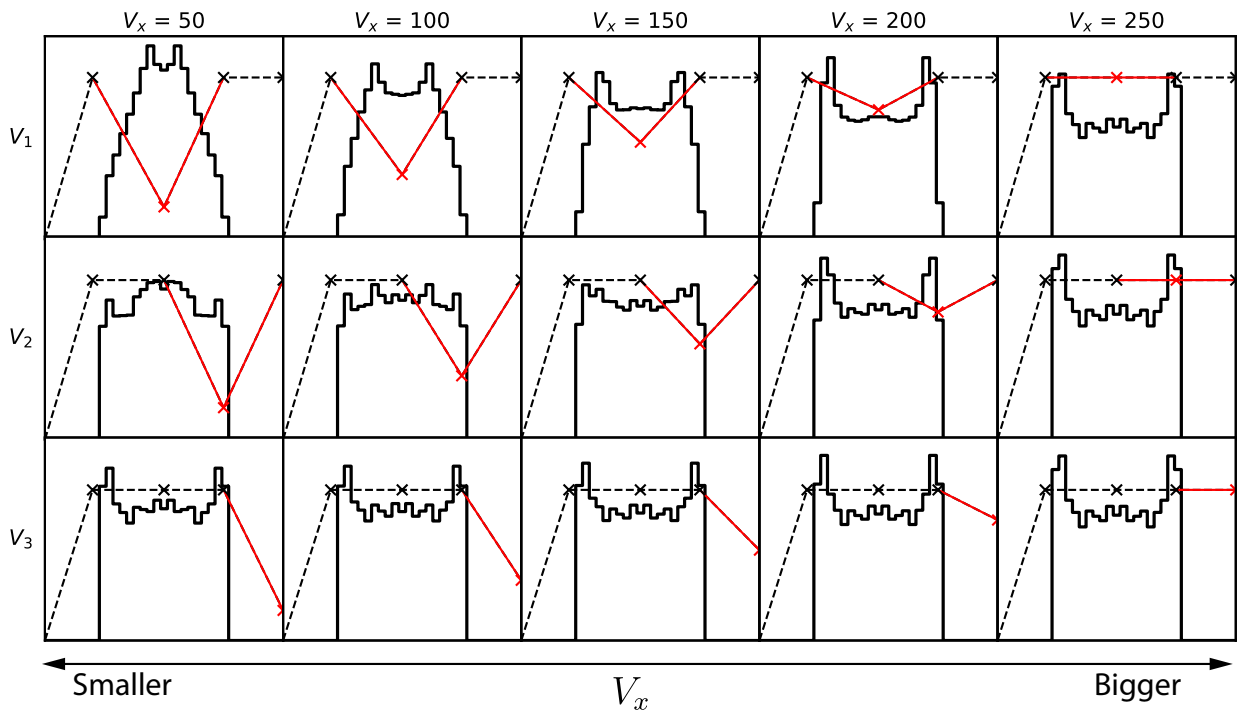

Fig. 5.3: Illustration showing the evolution of the global profile as V_1, V_2 and V_3 changes. For brevity, the velocities are denoted as V_x where $x = 1$, 2 or 3. The black dotted line shows the rotation curve, and the red line highlights the part of the rotation curve directly affected when V_x is tweaked.

The rotation curve that rises linearly and then becomes flat, is solely responsible for the characteristic double-horn shape that we see when integrating the emission over the whole galaxy. When h_r is very small, the outer parts of the rotation curve become insignificant: It still influences the shape of the line profile, but it doesn't matter because the intensity is so low. So when h_r is extremely small, the only part of the rotation curve that matters is the central part, which happens to be a linearly increasing function. This also explains why the profile is so narrow when h_r is small. There's still gas moving at $V_{\max}$, but the flux we get from that gas is just so insignificant that we almost do not see it; We only see the emission from gas moving at velocities close to $V = 0$.

The final parameter is the intensity at the center I_0. It scales the overall intensity throughout the disk, and consequently the flux of the profile. Because it does not alter the shape of the line profile, but merely scales the amplitude of it, I have not included a figure that illustrates the evolution of the line profile as I_0 is tweaked.

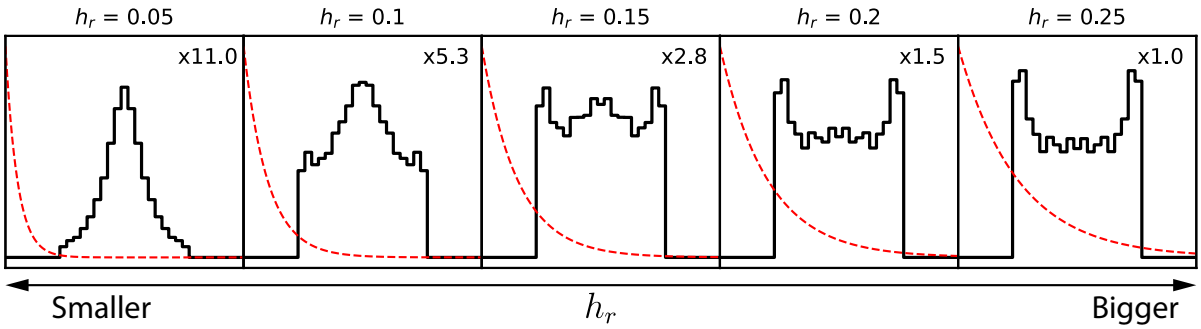

Fig. 5.4: Illustration showing the evolution of the global profile as h_r increases. The dotted red line shows the corresponding intensity profile. In order to better illustrate the differences in the shape of the profile, I scaled the amplitude by the number shown in the upper right corner of each box.

5.2 Asymmetry parameters

When there is a flux deficit on one side of the galaxy, the result is an asymmetric global profile. Let's explore how modifying the various asymmetry parameters introduced in section 4 affects the shape of the global profile.

The way in which I constructed the spiral masks is inherently symmetric, such that out of all the spiral parameters (table 4.2), the only parameter that directly causes asymmetry in the global profile is $S_{\rm as}$: When $S_{\rm as} < 1$ the spiral mask on the right side of the galaxy is much thicker compared to the spiral on the left side, which results in an asymmetric profile shape where the flux is much greater at negative velocities (figure 5.5). When $S_{\rm as} = 1$, the flux masks on both sides of the galaxy block equal amounts of light, and while the global profile has overall less flux, there is no asymmetry. When $S_{\rm as} > 1$ the situation is reversed and the spiral mask on the left side of the galaxy is much thicker and the resulting profile therefore exhibits a flux deficiency at negative velocities.

The width of the spiral arms are modified by $S_{\rm width}$ (figure 5.6). If $S_{\rm as} = 1$, then increasing the width of the arms only serve to scale the overall flux, since both sides of the galaxy are masked equally as much. On the other hand, when $S_{\rm as} \neq 1$ then $S_{\rm width}$ amplifies the asymmetry in the global profile.

Given the complexity of all the interactions between model parameters, it is not trivial to find degeneracies by manually changing one variable at a time. To explore how degenerate my parameters are, I chose to create simulated data sets using the model, and use a Markov Chain Monte Carlo (MCMC) routine to fit the simulated data. This allows me to create a set of posterior probability distributions for each parameter in the form of a corner plot. I let the computer do all the legwork of painstakingly cross-checking every possible combination of parameters. Any resulting degeneracy will then show a clear pattern that I can manually check by eye. (note to self: I have not done this yet. Good idea?).

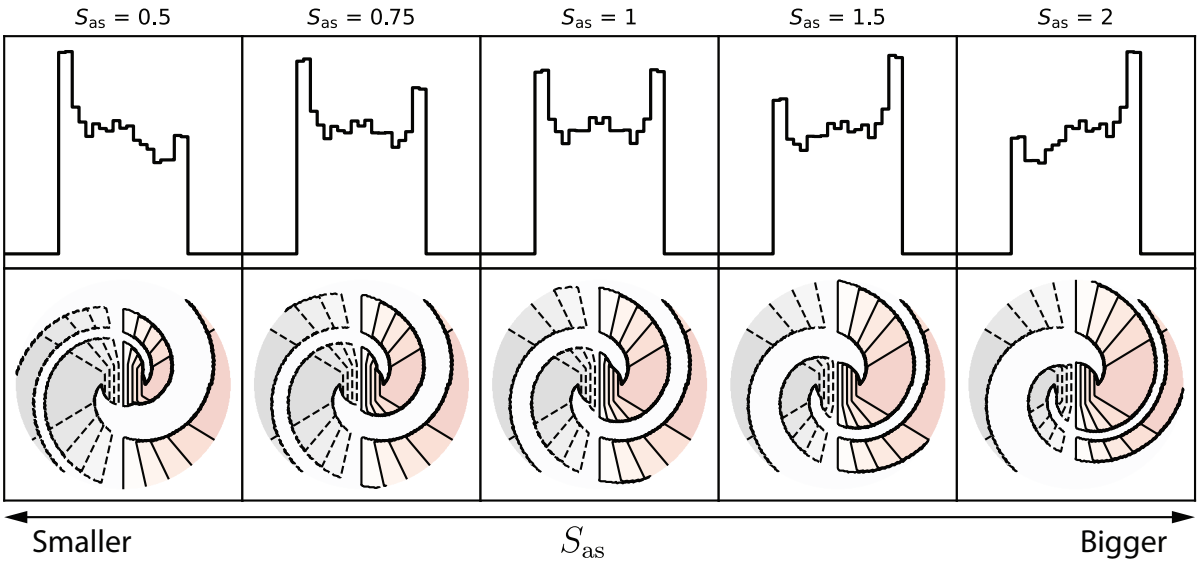

Fig. 5.5: Top: The evolution of the global profile as S_{as} increases. Bottom: Spider-diagram with the masked regions superimposed. The masked regions are shown purely for visualization purposes; they do not alter the radial velocity of gas at the position, only the flux. Parameter values used in this simulation: $S_{\text{width}} = 60$, $S_{\text{bulge}} = 0.2R_{\text{max}}$ and $S_{\text{flux}} = 0$.

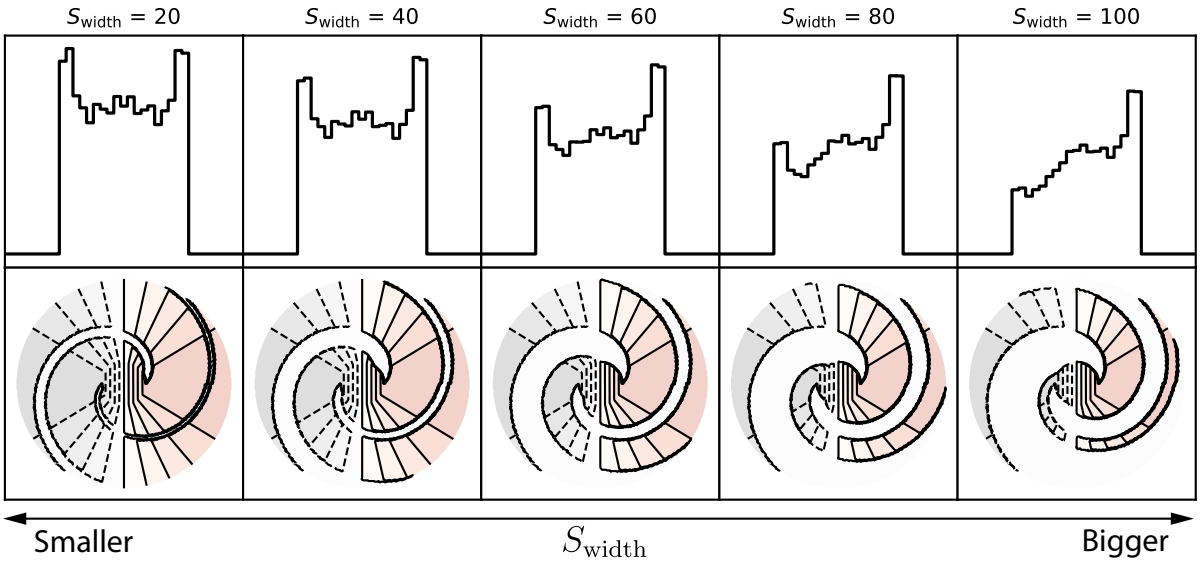

Fig. 5.6: Top: The evolution of the global profile as S_{width} increases. Because S_{as} is fixed at 1.5 in this simulation, the asymmetry is inherently present no matter the thickness of the spiral masks. When S_{width} becomes larger, it therefore only serves to intensify the inherent asymmetry. Bottom: Spider-diagram with the the masked out regions superimposed. The masked regions are shown purely for visualization purposes; they do not alter the radial velocity of gas at the position, only the flux. Parameter values used in this simulation: $S_{\text{bulge}} = 0.2R_{\text{max}}$, $S_{\text{as}} = 1.5$ and $S_{\text{flux}} = 0$.

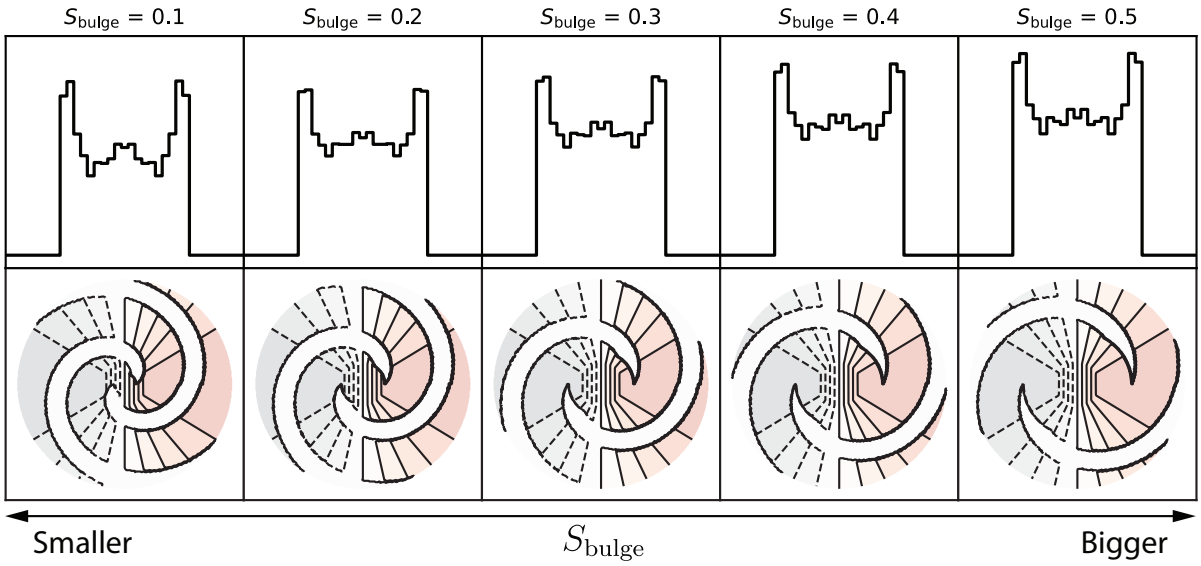

Fig. 5.7: Top: The evolution of the global profile as S_{bulge} increases. As the bulge becomes larger, a larger portion of the center is insulated from the spiral mask. In this case $S_{\text{as}} = 1$ (meaning there is no asymmetry in the masks), so the overall effect it has on the profile is to amplify the flux of the gas in the central regions of the galaxy $< 0.5R_{\text{max}}$. Bottom: Spider-diagram with the the masked out regions superimposed. The masked regions are shown purely for visualization purposes; they do not alter the radial velocity of gas at the position, only the flux. Parameter values used in this simulation: $S_{\text{as}} = 1$ and $S_{\text{flux}} = 0$.

6. Markov Chain Monte Carlo

This chapter is organized as follows: In Section 6.1 I outline the fundamental Bayesian problem that I attempt to solve using a Markov Chain Monte Carlo (MCMC) algorithm to test my model. In Section 6.2 I briefly describe how a typical MCMC algorithm operates. In Section 6.3 I explain in detail which MCMC package I chose to use, and how exactly I implemented it in practice. Finally, in Section 6.4 I outline and discuss the results obtained using MCMC.

6.1 Introduction

I opted for a Bayesian approach to find a set of model parameters that describe the data. A Markov Chain Monte Carlo method is a technique that utilizes probabilities to infer the posterior probability density function (pdf) given by

$$p(\theta|D) = \frac{p(D|\theta)p(\theta)}{p(D)} \tag{6.1}$$

where $p(\theta|D)$ is the probability of the model θ (which is actually a vector of the model parameters) given the data D, and is found by multiplying the so-called prior $p(\theta)$ (our prior knowledge of θ without having seen the data) and the likelihood $P(D|\theta)$, i.e. how we think the data is distributed. The constant $p(D)$ is called the "evidence", or sometimes the "marginal likelihood" and is very hard to calculate in practice, as it involves solving an intractable integral in multiple dimensions. The good news is that because $p(D)$ is just a constant, $p(\theta|D)$ is always known up to a constant factor. The ratios of the pdf at pairs of points can always be computed, but not the precise value at any individual point. In other words, the evidence cancels out in-between subsequent steps of the Markov Chain.

It should be noted that MCMC methods are essentially only good for one thing: sampling hard-to-sample pdfs. If the goal is to find the optimum of the likelihood or posterior pdf, an optimizer would be better suited for the task. In this work, the goal is not to determine accurate nor precise "best-fit" model parameters; The goal is to figure out how the different model parameters are connected, what their covariances are and to what extent they are degenerate. These are the main questions I will attempt to answer using MCMC.

6.2 A typical MCMC algorithm

The first step is to establish a function that outputs a model given a set of input parameters. This is described in section 4. The next step is to initialize a walker as defined by the choice of starting values for the model parameters θ. In practice this is a vector that contains n parameters θ_j, as used by the model-generating function.

The walker then starts to explore the parameter space, within the prior ranges defined. The walker takes a "step" to a new set of values of θ, and generates a model with that set of θ. It then compares the model to the data, via some likelihood function. Not to be confused with the likelihood, the likelihood function takes the data points as input, and represents the "likeliness" of different parameters of our distribution (D does not change). A likelihood on the other hand, is a probability density function that depends on the data only (θ is

fixed). The likelihood function, together with the prior pdf, can for all intents and purposes be considered a "model" in the context of MCMC. Because, under this definiton, the model can always generate parameters and parameters can generate data, the model is effectively a pdf over all possible data.

Generally speaking, the MCMC then compares the likeliness generated by the new model with the data vs. the current model. If the new model is a better match to the data, the walker moves there and repeats the process. If the new location is worse however, the walker either retreats to the previous position and tries a new direction, or it still moves (albeit with a lower chance) to the new position and repeats the process. The reason for not always retreating to the old position when the new model is worse, is that it can ultimately end up trapping the walker in a local minimum. The idea behind MCMC is that there is always a chance for the walker to explore the entirety of the posterior if given enough steps (in reality this will never happen, as the algorithm has to stop sampling at some point). Not giving it the chance to do so even though a certain direction may seem worse at first, will trap it in the first minimum it encounters. However, there is a possibility that if the walker were to take a chance on a "bad" step, it might encounter an even lower minimum in the future, and ultimately produce a better set of model parameters that describes the data.

At the end of an MCMC run, I have sampled from (hopefully) the posterior distribution. The walker keeps a record of the steps it took, including the likelihoods of the models given the data at those values of θ, in what is called a "chain".

The above is a very high-level description of what an MCMC algorithm generally does. In practice, there are many different algorithms that determines how a "move" of a walker is performed. The oldest and most well-known algorithm is the Metropolis-Hastings algorithm (Metropolis et al. 1953), on which the above description is loosely based.

6.3 Implementation

In this study, I utilize the package `emcee`[1] (Foreman-Mackey et al. 2013), an MIT licensed pure-Python implementation of the Affine Invariant Markov Chain Monte Carlo (MCMC) Ensemble sampler developed by Goodman and Weare (2010). The advantage of this package in particular is its Ensemble Sampler. Without going into details, it allows running a whole ensemble of samplers (or walkers) in parallel and they "feel out" the shape of the parameter space. As a bonus, multi-processing is built-in. As the efficiency of MCMC algorithms are often limited by computational power, being able to distribute work-loads across multiple CPUs drastically speeds up the usually slow sampling. This allows the walkers to go on extremely long field trips in the multidimensional parameter space in a relatively short time.

My data sample consists of a set of (x, y) pairs, $\{(x_i, y_i)\}$. The x_i (velocity) are known exactly, whereas the y_i (flux density) have been measured, each with some known resolution σ_i. By constructing the model described in section 4, I inherently choose to believe that y is given by some $f(x)$, which also depends on the model parameters θ. This is the ideal y, however, and our actual measurements have been smeared by the resolution. Because of the simplicity of the model I constructed, in reality y is most likely far from ideal, but this is what I intrinsically assume when I construct a model. Assuming that the distribution of measured y values about their ideals is Gaussian, the probability of a particular y_i, for a given x_i, is

[1] `https://emcee.readthedocs.io/en/stable/`

$$p(y_i;\theta) = \frac{1}{\sigma_i\sqrt{2\pi}} e^{-[y_i - f(x_i;\theta)]^2/2\sigma_i^2}$$

The algorithm needs a way to check if a given model is a good match to the data sample $\{y_1, \ldots, y_N; \theta\}$. I applied the principle of maximum likelihood here. The likelihood $\mathcal{L}$, is given by

$$\mathcal{L}(y_1, \ldots, y_N; \theta) = \prod_i^N p(y_i, \theta)$$

The idea is to determine the set of parameters θ that makes the probability of the actual results obtained, $\{y_1, \ldots, y_N\}$, as large as it can possibly be. For computational reasons, I maximize the logarithm of $\mathcal{L}$, which is the sum of the logarithms of the probabilities $p(y_i;\theta)$:

$$\ln \mathcal{L} = -\frac{1}{2}\sum_i^N \left[\frac{y_i - f(x_i;\theta)}{\sigma_i}\right]^2 - \sum_i^N \ln \sigma_i\sqrt{2\pi} \tag{6.2}$$

In fact, `emcee` *requires* the likelihood function to be given in logarithms. So to *maximize* the likelihood I have to *minimize* the quantity

$$\sum_i^N \left[\frac{y_i - f(x_i;\theta)}{\sigma_i}\right]^2 \tag{6.3}$$

i.e., to make the weighted sum of the squared differences as small as possible.

Starting off with just the "core" parameters outlined in table 4.1, θ is given by the vector

$$\theta = \begin{pmatrix} V_{\max} \\ b_0 \\ \vdots \\ h_r \end{pmatrix}$$

and is uniquely responsible for determining the model $f(x_i;\theta)$. Given my limited a priori knowledge of θ, I have chosen flat priors $p(\theta)$ for all the parameters, which means that the probability of any given parameter θ_j is the same over a specified range, and equal to 0 outside of that range. This is illustrated in Fig. 6.1. This type of prior is known as an ignorance prior, as it expresses our state of ignorance and is very non-restrictive (i.e., it gives `emcee` a lot of freedom). These types of uninformative priors are ideal in this study, as I have very little knowledge about the parameters I wish to constrain.

Finally, the posterior distribution that I wish to sample from, according to Eq. (6.1), is then given by

$$\ln p(\theta|D) = \ln p(D|\theta) + \ln p(\theta)$$

Because σ_i is assumed to be the same in every channel, the second term in Eq. (6.2) is effectively just a constant, and is irrelevant in the context of minimizing the likelihood. So the final equation for the posterior pdf I implemented in `emcee` is

$$\ln p(\theta|D) = -\frac{1}{2}\sum \left[\frac{y_i - f(x_i;\theta)}{\sigma_i}\right]^2 + \ln p(\theta) \tag{6.4}$$

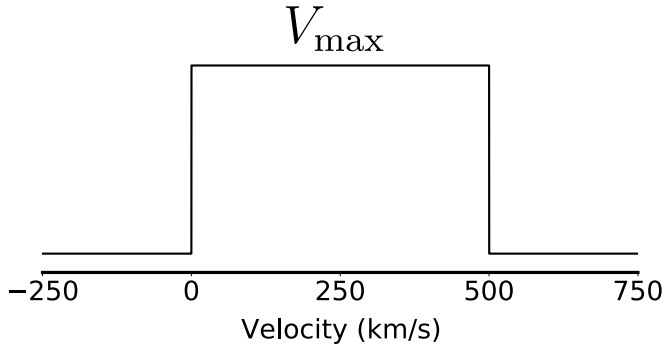

Fig. 6.1: Visual illustration of a so-called top-hat prior probability distribution for $V_{\rm max}$. The probability of $V_{\rm max}$ assuming any of the values in the range $V \in (0, 500)$ km s^{-1} is constant, and 0 anywhere else.

Table 4.1 gives an overview of the prior ranges (or limits) for each parameter of $p(\theta)$ used in the MCMC algorithm.

I used the same MCMC configuration for every galaxy in my sample to keep results consistent. I configured `emcee` in the following way: I used 15 walkers that were given random starting values for θ in the ranges defined in Table 4.1. The random values were drawn from a flat probability distribution in the prior range for each parameter θ_j (Fig. 6.1). I experimented with different "moves" offered by `emcee`[2] and found that the default Stretch Move (Goodman and Weare 2010; Foreman-Mackey et al. 2013) gave me the best result. I considered an MCMC run a good result if two conditions were satisfied: (1) the chain of steps involved had converged, (2) the acceptance fraction of proposed moves was in the region 0.2-0.5. Gelman et al. (1996b) found that best performance for high-dimensional problems is achieved when the acceptance fraction hovers around 0.234, so this is what I aimed for in my choice of moves.

To determine when a chain had converged, I opted for a qualitative approach: I looked at so-called "trace plots" and determined by eye whether or not the chain had converged. Trace plots show the model parameter values as a function of step number. A sample trace plot for the parameter $V_{\rm max}$ for NGC 3227 is shown in Fig 6.2. I considered a chain converged when the walkers stopped chaotically moving around the parameter space and settled in a stable "orbit" around some value. The example shown by the chain in Fig. 6.2 is very well-behaved, and it is not always this easy to recognize when a chain has converged. Sometimes the walkers settle in multiple "lanes" of θ_j values and never converge on a single one. Other times the walkers simply never converge, and just flail around the entire prior range. This can be indicative of degeneracy with other parameters, or it can mean the chain is too short. It could also mean that my parametrization of the model could have been done in a better way.

Diagnosing whether or not a chain has converged is a whole science in itself. A common approach that I did not utilize in this study is to look at the integrated autocorrelation time of the chain. Every step in a chain $(\theta_1, \theta_2, \theta_3, ...)$ generated by a Markov process naturally depend on the previous step. This means that the chain does not consist of independent samples. However, when enough steps have been taken, the chain eventually "forgets" its earlier state, and the new sample can be considered independent if enough steps are taken in between the two. The number of steps it takes for two samples to be considered independent,

[2] `https://emcee.readthedocs.io/en/stable/user/moves/`

is exactly what the integrated autocorrelation time measures. It is then possible to "thin" the chain by only considering every n'th step in the cain, as determined by the autocorrelation. This method is very advanced, and is mostly used in situations where a trace plot inspection is not sufficient to root out issues.

In this study, as will be made clear in chapter 6.4, there are very major issues in some MCMC runs that are obvious, without the need of advanced diagnostic procedures to tell me that.

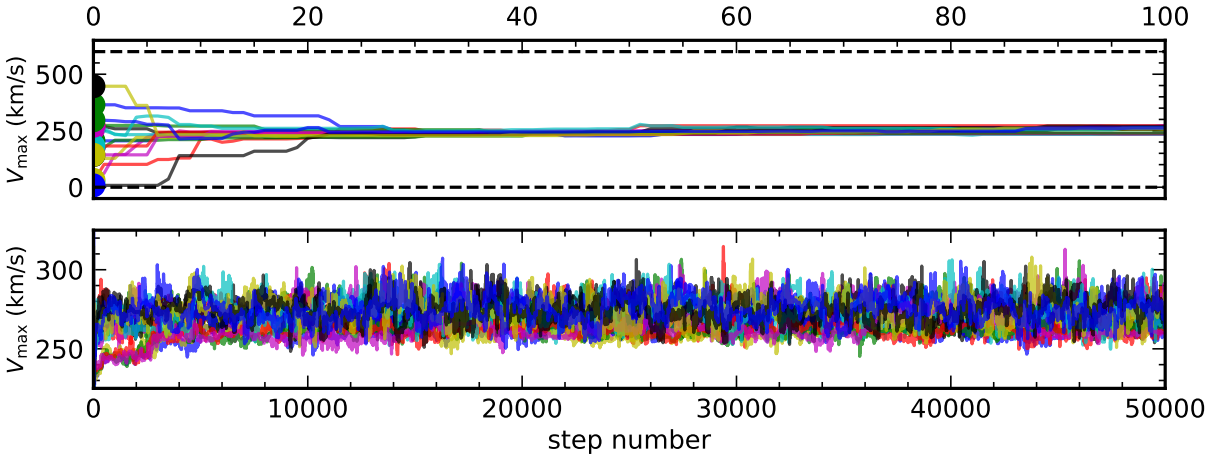

Fig. 6.2: Top: Sample trace plot showing the first 100 steps of 15 walkers that have been initialized to random starting values for $V_{\max}$ in the range 0 to 600 km s^{-1}. The filled colored circles indicate the starting positions for each walker. The horizontal dashed lines indicate the prior range. The walkers quickly converge on a single value and start to orbit around the value 270 km s^{-1}. Bottom: The same trace plot as above, but with a tigher y-range and 50000 steps.

6.4 MCMC results

6.4.1 MCMC diagnostics

In the world of probability, there is no single "answer"; there are only probability density functions. Because MCMC is a tool for integration, I will limit the "results" that I report in the following to integral-based statistics that can be computed with the sampling, such as expectations, medians and quantiles. This does not include the "best" sample or mode or optimum. My best integral-based option for a "measurement" is the median of the posterior (the 50$^{\text{th}}$ percentile). Compared to the average, the median is a more robust statistic to extract, as it is less influenced by heavily skewed distributions, of which there are plenty in this study. If the posterior probability distribution is skewed enough, it is actually possible for the posterior average to be outside the 1σ interval (this is actually the case for some of my sampled distributions). My best options for "errors" or "limits" are variances or posterior quantiles. In this work I will use quantiles: The 1σ error is half the central interval of the parameter that contains 68% of the posterior samples. The so-called 1σ "credible" region around the median is therefore bounded by the $0.50-0.68/0.5 = 0.16$ and $0.50+0.68/2 = 0.84$ quantiles (or 16% and 84% percentiles). With all the above in mind, when I report a specific "measurement" of a parameter, it is the median value of the posterior distribution

belonging to that parameter. Similarly, when I report $\pm 1\sigma$ uncertainties on these median measurements, they are the 16% and 84% percentiles of the posterior, respectively.

Even if the model turns out to match the data well, and the posterior pdf is well-behaved (unimodal), the median of the posterior pdf for each of the parameters θ_j, when taken together as a "best-fit" parameter, will not necessarily be a good representation of the data. For one, it could very well be that the walkers never actually found the "right" minimum that describes the data. Perhaps the algorithm did not run for long enough, or the proposal move—on which the movement of the walkers is ultimately based—does not allow the walkers to explore the posterior pdf fully. Secondly, if the posterior pdf has multiple modes (i.e., multiple peaks in the probability distribution), or has substantial "curvature" (i.e., heavily skewed distributions) in the parameter space, the mean or median of sampling does not necessarily lie at high probability locations in parameter space. This all relates to the point made in Section 6.1, namely that `emcee` is not an optimizer, it is merely a sampler that lets us get a taste (or sample) of how the multidimensional posterior looks and behaves. With this in mind, I will in the following describe the results obtained with MCMC.

6.4.2 Model representations

I will present results obtained with MCMC in the form of diagrams, known as "posterior predictive plots", "trace plots" and "corner plots". Additionally, the resulting inferred rotation curves, intensity profiles and spider diagrams are also included. Appendix B showcases all three of these figures associated with every galaxy in my sample, after running MCMC with 15 walkers and 250 000 steps, using the seven core parameters listed in Table 4.1.

The posterior predictive plots (e.g., Fig. B.1) show the predictive distribution for the model in data space. I extracted 1000 random samples from the chain of a completed run that was applied to a given data set. I then displayed the predicted model that each extracted sample makes for this data set, by superimposing these models on the observed data. Additionally, I superimposed the model constructed from the 50^{th} percentile (across all parameters) of the posterior distribution. This model can for all intents and purposes be considered the most representative (of the data) line profile. In the bottom part of the figure, I show the residuals. The residual is calculated as the difference between the data and the model, in units of the data RMS:

$$\text{Residual} = \frac{\text{Data} - \text{Model}}{\text{RMS}}. \tag{6.5}$$

The trace plots (e.g., Fig. B.3) show the model parameters as a function of step number in the Markov chain. The gray shadow indicates the burn-in region (i.e., discarded samples; half of the total 250 000 samples).

The corner plots (also known as "scatterplot matrices", e.g., Fig. B.4) show all the one and two dimensional projections of the posterior probability distributions of my parameters. The 2D histograms show the covariances between parameters. The 1D histograms along the diagonal show the marginalized distributions for each parameter.

Mrk 590

Starting off with the CO(2-1) emission line in Mrk 590, the model (Fig. B.1) is quite decent, and (mostly) stays within the $\pm 1\sigma$ residual. The corner plot (Fig. B.4) shows that most of the parameters have unimodal marginalized distributions, with the exception of I_0 and h_r. I_0 and h_r are heavily correlated, as can be seen from their covariances. So if either one

of them is ill-defined, the other suffers the same fate. The unimodality of the remaining parameters is also reflected in the trace plot (Fig. B.3): The parameters that have single-peaked marginalized posterior distributions tend to "orbit" around a single value in the trace plot. If the chains looks "fuzzy", as they do in this case, it is a good sign of convergence. If the 1D probability distribution of a parameter has multiple peaks, then the chain will consist of multiple "lanes" that the walkers will move on. The rotation curve shown in the left panel of Fig. B.2 is a textbook example of a rotation curve that we have come to expect from disk galaxies (Kauffmann et al. 2015; Lang et al. 2020; Sharma et al. 2021) that have ordered rotation about the center. The initial steep ascent of the rotation curve produces the characteristic parallel velocity contours that can be seen at radial positions $R < 0.2\,\mathrm{R_{max}}$ in the accompanying spider diagram (right panel of Fig. B.2). The rotation curve decreases slightly between 0.2 and $0.5\,\mathrm{R_{max}}$. As a result, the velocity contours of the spider diagram start to close in on themselves; but this process is cut short as the rotation curve flattens out at $\mathrm{R_{max}} > 0.2$, at a velocity of $\sim 220\,\mathrm{km\,s^{-1}}$. This is reflected in the velocity contours moving radially away from the center.

This particular data set is an exceptional example of the kind of emission line that I primarily designed the model to simulate in the first place: A very clear double-horned profile with minimal asymmetry. So it is not a surprise that the model performs well in this case. In fact, the similarity between these results and the example of M31 (Figs. 1.1, 1.3 and 1.2) described in Chapter 1 is quite astounding - especially because the model is so simple.

NGC 2617

The CO(2-1) line in NGC 2617 is a curious one (Fig. B.5). MCMC has apparently found what looks like two solutions (or minima). One of them, championed by the median, represents the data quite well. The other is a single-peaked solution shown by a subsample of the 1000 random draws. Looking at the trace and corner plots (Figs. B.7 and B.8), it looks like a few of the walkers got trapped in a solution with a high velocity value. According to the defined parameter limits, this means that all the velocity break-points V_1, V_2 and V_3 follow suit as well and get trapped in a high V_{max} solution. Additionally, the tiny amount of samples corresponding to this solution, seen on the marginalized distributions of the velocity parameters, is also a testament to the low-probability of this particular solution. Without looking at either the trace or corner plot, the single-peaked solution is obviously erroneous, as it does not match the data at all. It can safely be ignored. The CO(3-2) line (Fig. B.9) tells a similar story to the CO(2-1) line, and it appears that the parameters found are extremely similar, with the exception of I_0. This is to be expected, as both the CO(2-1) and CO(3-2) observation share the same RMS, but different S/N ratios (Table 3.2). This suggests that the kinematics of both transitions are quite similar, and they differ exclusively by a flux emission factor. The associated rotation curve and spider diagram shown in Fig. B.6 are quite similar to the ones produced for Mrk 590. The big difference here is that the break-point b_0 is much smaller, meaning that the initial rise of the rotation curve is much steeper. This fact is also reflected in the smaller (compared to Mrk 590) central region consisting of parallel velocity contours.

NGC 3227

MCMC has trouble modelling the CO(3-2) emission line in NGC 3227 (Fig. B.13). The residuals flail wildly between $\pm 5\sigma$ over the line profile. There has been indications that some of the hot H_2 gas (which CO is a tracer of) in NGC 3227 is influenced by outflows

(Davies et al. 2006). The model does not account for such non-rotational motions in the disk, and it is therefore not a big surprise that it has trouble finding a set of model parameters that represent the data. Despite this limitation of the model, it still manages to do the best it can, and produces something that is not too terrible, all things considered. In fact, the MCMC walkers quickly managed to find a minimum (read: areas of high likelihood) and stay there for the entirety of the MCMC chain. The trace plot (Fig. B.15) shows that the chain converged almost immediately at the start of the run, despite a couple of walkers taking a small detour at higher $V_{\rm max}$ values, but then finally joined up with the rest of the pack around 200 000 steps in. The individual 1D parameter distributions in the corner plot (Fig. B.16) are also unusually unimodal (despite the unique shape of the emission line), which suggests that the chain has converged on a solution that all 15 walkers agree on. The rotation curve in the left panel of Fig. B.14 differs somewhat from the rotation curves extracted from the remaining AGN in my sample (with the exception of NGC 4593, discussed in more detail further down). Because we know that NGC 3227 has outflows, the kinematics shown by the rotation curve and spider diagram are difficult to evaluate and interpret. The model attempts to compensate for this non-rotational velocity component by altering the kinematical parameters ($V_{\rm max}$, V_1, V_2 and V_3) that are responsible for the rotation curve and consequently, the spider diagram, at the cost of what we believe is physically reasonable.

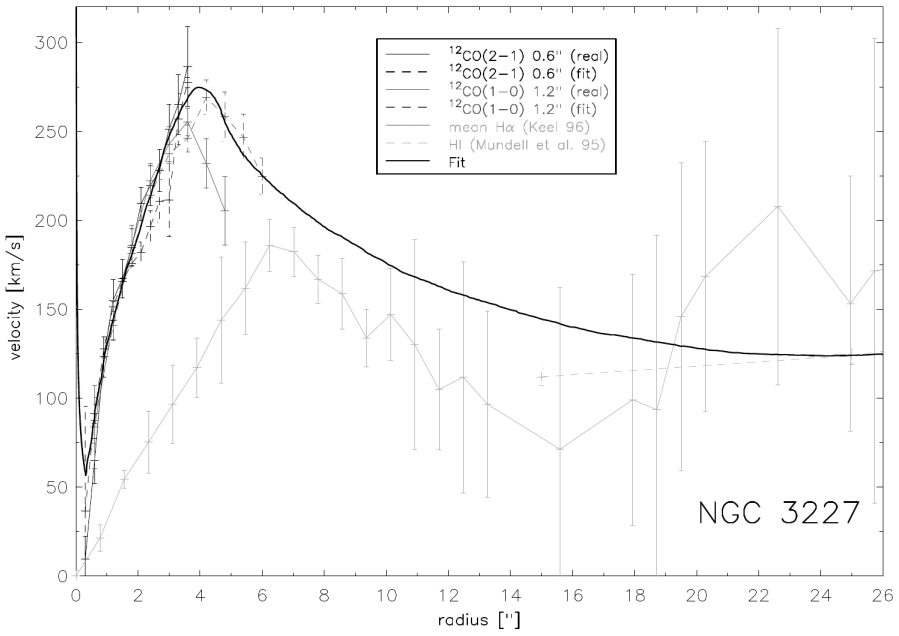

Fig. 6.3: Rotation curves of NGC 3227. The rotation curves derived from the CO data as well as curves taken from the literature are shown. The thick line is the best fit to the different curves. Source: Schinnerer et al. (2000).

This problem can be approached from another angle as well. Comparing the size of the telescope beam at 345 GHz (= 18″) to the apparent size of NGC 3227 on the sky, shown in the right panel of Fig. A.12, can fuel the discussion a bit longer. A double-horned profile (such as the one for Mrk 590), is characteristic of a rotation curve that first rises, then remains roughly flat with increasing radius from the center. If instead we consider a galaxy in which the rotation curve rises at all radii, we would see a flat-topped or centrally peaked profile instead (Sparke and Gallagher 2007). The triangular shape of NGC 3227 exhibits exactly that. What does that tell us? The small beam size of the APEX telescope will

inevitably collect flux only from the CO gas in the very central region of the galaxy. The actual rotation curve of NGC 3227, shown in Fig. 6.3, mainly consists of a steep rise in the central $\sim 9''$ (half the beam size). This means that the CO(3-2) observation that I have at my disposal, is in reality just an observation of gas motions characterised by a rising rotation curve (in the central $9''$). In that case, I would *expect* to see a centrally peaked profile. The model inherently assumes that the emission line it is trying to represent, is the result of a an integration of flux across an entire galaxy, and not just the central region. One might have expected that the MCMC model would be challenged in predicting the rotation curve. However, it is encouraging to see that the model does indeed predict a rotation curve with a central rise that extends to half the size of the beam.

NGC 3783

The CO(2-1) emission line of NGC 3783 is extremely asymmetric (Fig. B.17. As the model (using the core parameters), is inherently symmetric, the model does not represent the data all that well. MCMC also seems to have found two candidate solutions, much like NGC 2617 CO(2-1) and CO(3-2). For the same reasons described for NGC 2617, the solution with a $V_{\rm max}$ hovering around $\sim 450\,{\rm km\,s^{-1}}$ (Fig. B.20) is unrealistic and can be ignored.

To improve the model, I expanded it to include $S_{\rm width}$, $S_{\rm as}$ and $S_{\rm flux}$ (Table 4.2). The results are shown in Figs. B.45-B.48. There is surprisingly good match between the model and the data. The flux residuals are within $\pm 1\sigma$ across the emission line. Even though it is a good match, the question is whether or not the model parameters make sense physically. The spider diagram shows that MCMC found a solution that describes a galaxy with one spiral arm emitting up to $S_{\rm as} = 3.27^{+0.51}_{-0.62}$ times as much compared to the other. This should not be interpreted as how the flux of CO gas in NGC 3783 is actually distributed. The spiral aspect of the parametrization is just a means to an end: altering flux from one side of the galaxy. The data clearly shows that there is an excess of flux at positive velocities, compared to negative velocities. The exact reasons for why there is this asymmetry in the flux is not something the model can answer.

NGC 4593

The CO(2-1) line in NGC 4593 is unique in the sense that it appears to have a flat top. Despite this, MCMC does a decent job fitting the data as shown in Fig. B.21. The walkers seem to explore quite chaotically in the first "50000" steps of the Markov chain (Fig. B.23), but then settle in for the remainder of their walk after that. Additionally, the marginalized parameter probability distributions in the corner plot (Fig. B.24) are well-behaved (i.e., unimodal), suggesting convergence. As a result of the limits I imposed on the velocity parameters $V_{\rm max}$, V_1, V_2 and V_3 (Table 4.1), the model is mathematically unable to create a flat-topped distribution, no matter the combination of parameters. It would require an unrealistic rotation curve that is "not" flat (or close to being flat) at higher R to produce a flat-topped profile as the data shows. The MCMC model of the CO(3-2) line in NGC 4593 produces similar parameter values as the CO(2-1) line, once again suggesting similar kinematics between the two transitions of CO (which is to be expected). The S/N ratio is quite a bit lower for the CO(3-2) line, which inflates the uncertainties dramatically. It is worth noting that the CO(2-1) data was collected by integrating for ~ 90 minutes, whereas the CO(3-2) data was integrated for ~ 20 minutes (Table 3.2).

Interestingly, it seems that the rotation curves and spider diagrams (Figs. B.22 and B.26) share some similarities with NGC 3227 (Fig. B.14). They all have relatively shallow slopes

at small R of the rotation curve, followed by a sudden large (relatively) drop in velocity. Not surprisingly, the spider diagrams exhibit comparable characteristics such as the large central region of parallel velocity contours and contours that close in on themselves further out (as a result of the drop in the velocity at $\sim 0.5\,\mathrm{R_{max}}$). NGC 3227 and NGC 4593 have a couple of things in common: They both have an extraordinary excess of flux at small velocities (close to $V = 0$), compared to the rest of the sample of AGN. And for both galaxies, the model found a double-horned solution with a central peak.

The similarities do not stop there though. As was the case for NGC 3227, the beam size of APEX (at both 230 GHz and 345 GHz) only covers the central region of NGC 4593. The relative size of the beam and the size of the galaxy is not as extreme in this case however, which means we should expect to see a less dramatic (yet still similar) version of the centrally peaked shape of NGC 3227. This is indeed what we see. Instead of the major excess of flux at $V = 0$ that forms a peak in NGC 3227, instead forms a flat-top. This is what we expect from a situation that can be considered a middle-road between the extreme case of NGC 3227, and cases where the beam covers the entire apparent size of the galaxy, such as Mrk 590, NGC 2617 and NGC 3783. It is no surprise that we see double-horned profiles for the sources where the beam covers the entire galaxy, as this is what our theory of gas kinematics tells us to expect.

NGC 5548

The CO(2-1) line in NGC 5548 is just a tad asymmetric (Fig. B.29), having a larger concentration of flux at positive velocities. The model cannot account for this, so it tries to find the best symmetric solution it can. The scaling factor I_0 has the largest uncertainty, which is reflected by the 1000 draws that span a wide range of profile shapes around the median. Given the relatively large RMS of 0.06 Jy, this is not too much of a surprise. Given the low resolution of the spectrum, it is difficult to judge whether or not the congregation of flux in the channels around $-230\,\mathrm{km\,s^{-1}}$ is part of the signal (perhaps in the form of an outflow), or it is merely noise. This is a judgement call, and since the model was not made to simulate non-rotational velocity components, I chose not to include this in the fitting window of MCMC. It is unclear whether or not the chain has converged, as both the trace and corner plot (Figs. B.31 and B.32) show multiple multimodal distributions of roughly equal probability (neither of them overpower the other). This is evident from the 1D distributions for V_{max}, V_1, V_2 and to a lesser extent, V_3, and by the multiple lanes that never seem to join up in the Markov chain. Despite this ambiguity, the two solutions are not all that dissimilar, as they are hard to distinguish from the 1000 randomly drawn model predictions. The median, as mentioned earlier, is a very robust percentile that represents the data quite well, despite ill-behaved distributions. In this case the median seems to express a "sweet spot" between the two solutions. This is also reflected in the fact that the median (represented by the red line in Fig. B.29) rests comfortably between the two solutions, and represents the data quite well.

The CO(3-2) line is modelled as well as you could reasonably expect (Fig. B.33), given the low resolution and S/N ratio (= 4.01) of the spectrum. This is the spectrum that was initially classified as a non-detection by the 5σ cutoff that I imposed in Section 3.1, and later re-classified as a detection (simply looking at the spectrum makes it hard to call it a non-detection). Despite the low quality of the observation, MCMC managed to converge in a much more convincing manner than the CO(2-1) line: The marginalized distributions in the corner plot (Fig. B.36) are quite well-behaved. The fact that the resulting median parameter values for both CO(2-1) and CO(3-2) are nearly identical, supports the argument

that this is indeed a detection; we expect the kinematics of the gas to be similar for both CO(2-1) and CO(3-2) as they are transitions of the same molecule, spaced close together energetically.

NGC 6814

The width of the CO(2-1) line in NGC 6814 is extremely narrow (Fig. B.37), which makes it hard to model (as it lacks resolution). I rebinned the data to a resolution of $\sim 10\,\mathrm{km\,s^{-1}}$ to alleviate this issue somewhat. Despite this, the emission line only has 9-11 data points (depending on which ones you count), and the model has seven parameters. This means that MCMC only has 2-4 degrees of freedom, which makes modelling difficult. The model still looks decent, mostly staying inside the $\pm 1\sigma$ residual, and sometimes (at the edges of the line) reaching $\sim 2.5\sigma$. The trace plot in Fig. B.39 looks good; the walkers quickly found a minimum and stayed there for the rest of the run. The marginalized parameter distributions are also mostly unimodal. The CO(3-2) line (Fig. B.41) is likewise a case of an ill-constrained problem to solve, but MCMC still managed to find a model that describes the data within $\pm 1\sigma$ flux residuals across the emission line.

7. Discussion

7.1 CO gas measurements

I have determined various properties of the CO gas in my sample of AGN, including the total velocity-integrated flux density, CO luminosity and the total molecular gas mass in the form of H_2. I find an average CO luminosity of $L'_{\rm CO} = 4.35 \pm 1.09 \times 10^8 {\rm K\,km\,s^{-1}pc^2}$ with a standard deviation (SD) of $2.99 \times {\rm K\,km\,s^{-1}pc^2}$ for the sample of 6 CO(2-1) detections.

I estimate a mean molecular gas mass of $M(H_2) = 11.35 \pm 9.53 \times 10^8 M_\odot$ with a SD of $2.19 \times 10^8 M_\odot$ using the CO(2-1) observations as inference via. the r_{21} ratio (Section 3.4).

The uncertainty on the conversion factor is mostly responsible for the high uncertainty on the molecular gas mass estimate. Because I do not a priori know about the local conditions of the ISM where the CO gas resides, I followed the recommendation of Bolatto et al. (2013), and assumed a conversion factor $\alpha_{\rm CO} = 3.3 \pm 2\, M_\odot ({\rm K\,km\,s^{-1}pc^2})^{-1}$. The uncertainty is extremely huge, as it embodies my ignorance of the gas pressure, gas dynamics and metallicity in the local ISM. So while the uncertainty on the H_2 gas mass is very large, it should be seen as a conservative estimate of the ranges of H_2 gas masses for the AGN in my sample.

7.1.1 Comparisons of CO to non-active galaxies

To get a perspective on values of the CO luminosities and H_2 gas masses that I have calculated in a global context, I compare with different studies that have also measured the CO luminosities and H_2 gas masses, as well as the Milky Way and our nearest neighbor, M31. The mass of the molecular gas in M31 within a radius of 18 kpc is $M(H_2) = 3.6 \times 10^8 M_\odot$ at the adopted distance of 780 kpc. This is 7% of the total neutral gas mass in M31 (Nieten et al. 2006). So M31 has an overall lower molecular gas mass than the average value for my sample of AGN. Sparke and Gallagher (2007) argues that the Milky Way on the other hand, probably contains $4\text{-}8 \times 10^9 M_\odot$ of HI, and about half that amount of molecular gas. This means that the Milky Way contains roughly five times more molecular gas in the form of H_2 than the average of my sample of AGN.

Cicone et al. (2017) presented CO(2-1) emission line observations of 88 nearby, low-mass, star-forming galaxies that are part of the APEX low-redshift legacy survey for molecular gas (ALLSMOG). As part of their measurements of the CO gas, they calculate the line flux and CO luminosities, and also apply the beam correction described in Section 3.5. Their results for the average CO luminosity is shown in Table 7.1. Additionally, Cairns et al. (2019) performed measurements of both the CO line flux, CO line luminosity and $M(H_2)$ on 27 CO(2-1) emission lines in their sample of 72 star-forming cluster galaxies. These galaxies were selected to span a wide range of stellar masses and star-formation rates. These values are also listed in Table 7.1. Based on the CO(2-1) luminosities I find that my sample of AGN have higher masses roughly by a factor 10 compared to the study by Cicone et al. (2017) (assuming a 1:1 relationship between mass and luminosity), whereas when compared to the average CO(2-1) luminosity of Cairns et al. (2019), both results are consistent, within their uncertainties (and standard deviations). Having compared these findings with a little bit of everything (read: different types of galaxies with different properties), it seems that my sample of AGN display typical molecular gas masses across different galaxies. It is also worth noting that my H_2 gas masses may have a minor tendency to be systematically larger for the galaxies in my sample that exclusively observe the very central regions of the AGN,

e.g., NGC 3227 (Fig. A.12) and to a lesser extent, NGC 4593 (Figs. A.15 and A.16). Hicks et al. (2013) find that AGNs tend to have elevated H_2 luminosity out to a radius of at least 250 pc, and more specifically, that AGNs have four times higher H_2 luminosity within a radius of 100 pc compared to their quiescent counterparts. So while there may not be the biggest difference in molecular gas mass at large scales, this may not be the case at smaller scales.

Table 7.1: Comparisons of the average, their associated uncertainties and standard deviations of the CO(2-1) measurements between two studies targeting different galaxies. The number in the parenthesis next to each measurement is the 1σ standard deviation of the sample used to calculate the average.

Measurement	$\int S_{\mathrm{CO,corr}}\,\mathrm{d}v$ ($\mathrm{Jy\,km\,s^{-1}}$)	$L'_{\mathrm{CO,corr}}$ ($10^8\,\mathrm{K\,km\,s^{-1}pc^2}$)	$\mathrm{M}(\mathrm{H_2})_{\mathrm{corr}}$ ($10^8\,\mathrm{M_\odot}$)
This project			
Detections	227.28 ± 54.95 (95.66)	4.35 ± 1.09 (2.99)	11.35 ± 9.53 (7.8)
Non-detections	< 13.57 (4.10)	< 2.42 (1.67)	< 6.33 (4.36)
Cicone et al. (2017)			
Detections	29.51 ± 9.57 (22.26)	0.79 ± 0.37 (0.68)	–
Non-detections	< 9.36 (2.20)	< 0.37 (0.12)	–
Cairns et al. (2019)			
Detections	36.14 ± 7.53 (22.46)	1.95 ± 0.49 (1.41)	8.91 ± 1.86 (6.24)
Non-detections	< 14.02 (7.87)	< 0.55 (0.27)	< 2.26 (0.93)

7.2 Forward-model of the CO global profile

Modeling the kinematics of the gas in galaxies is not a novel idea. For example, Stewart et al. (2014) made a 6-parameter mathematical model for the global HI profiles of galaxies. They find the model to be a good fit to the 34 spiral galaxies in the HI nearby Galaxy Survey (THINGS; Walter et al. (2008)). The difference here is that I modelled an actual two-dimensional rotating disk of gas, with some inclination. Each two-dimensional subsection of the disk has a certain size (defined by how finely the disk is partitioned) and location. This method has the advantage of allowing one to discretely modify the flux, velocity, area and anything else you could think of (depending on how you define the model), of every single subsection of the disk.

By altering the flux in certain patterns of subsections, as I have demonstrated in Section 5.2, I managed to produce asymmetric shapes in the resulting global profiles produced by the model. This can further be expanded to include non-rotational velocity components such as outflows in future work. The main point is that this type of forward-model shows great promise, even in its current simple form. The model is able to produce synthetic emission line profiles that match the data that we see in practice when we integrate flux over a galaxy. It should be mentioned again that the AGN that comprise my sample, for the most part have CO observations that only cover the central circumnuclear regions of the AGN, which makes it really hard for the model to produce representative global profiles. Despite this,

it still manages to produce decent-looking models. Besides, even the MCMC runs that are uncertain (either as a result of unclear convergence or other limitations), can be explained when the rotation curves and spider diagrams are examined.

Additionally, there is a significant number of observations that are of poor quality (low resolution/SNR and very narrow profiles) that only makes life harder when attempting to infer representative models. If the question of whether or not the location of an expected emission line actually has a signal, or is just the result of random noise is ambiguous, then there is not much anyone can do. All in all, the model does produce sensible solutions and sets of parameters that we would expect from a disk galaxy with ordered rotation. The rotation curves and spider diagrams that are produced as a result of the MCMC runs, are particularly interesting as they directly tell us how the gas is distributed and moves around in the galaxy (or, at least how the "model" thinks the distribution and kinematics of the gas looks like).

7.3 Future work

The models produced with MCMC are already quite good, but can definitely be improved, especially if I want to investigate high S/N emission profiles or perhaps even spatially resolved kinematics. Adding non-rotational velocity components (such as outflows) to the model would be a logical next step. Reparametrizing the model could also yield positive results, as it is clear right now that there are some degeneracies among the model parameters (I_0 and h_r in particular), that unnecessarily complicate the model. This would ensure that the MCMC algorithm has an easier time finding minima, and allow the walkers to explore the posterior probability distribution more efficiently. This way I could determine rotation curves and spider diagrams independently of the model, and check whether or not the model would converge on a solution that approximates this "truth". In fact, it would be the perfect laboratory environment to test out a wide variety of different things, as the possibility of instant feedback on model performance would not only be a time-saver but also allow much more detailed tweaks to be made, in order to improve the model.

8. Conclusions

I have presented the APEX CO (2-1) and CO(3-2) emission line observations of 17 nearby AGN host galaxies. I have described in detail the sample selection, observations, the data reduction and analysis methods. I report a final CO(2-1) detection rate of 37.5% (6/16), and a CO(3-2) detection rate of 50% (4/8). For the detections, I have determined their total velocity-integrated flux densities, CO line luminosities and H_2 gas masses (Table 3.2). These results were further corrected for potential CO emission falling outside the primary APEX telescope beam, thereby allowing me to report the gas mass of the entire galaxy, even though the beam in many cases only covers the circumnuclear central few kpc (Table 3.3). For the non-detections I have estimated informative 3σ-upper limits on the line flux. Additionally, I have directly measured both the FWHM width, and the peak of the rotation curve for all detections in the sample, and find an average $V_{\rm max}$ of $144.62\,{\rm km\,s^{-1}}$ with a standard deviation of $86.17\,{\rm km\,s^{-1}}$, and an average FWHM line width of $198\,{\rm km\,s^{-1}}$ with a standard deviation of $86\,{\rm km\,s^{-1}}$. The individual measurements can be found in Table 3.1.

To study the motion of the gas, I wrote software code for a simple model of the gas structure and kinematics in a typical AGN. The model assumes some inclination, rotation curve and intensity distribution, in the form of variable model parameters. By simulating a single-dish radio telescope observation of a toy galaxy, with a large enough beam that includes all the gas, I simulated the distribution of gas in coordinate and velocity phase space and compared it with the data using MCMC analysis. I find that a simple model does indeed have the capability of producing emission line profiles that we see in the data. The specific set of model parameters responsible for producing the fits are tentative at best, and does not indicate a unique solution in some cases.

Bibliography

M. Aravena, J. A. Hodge, J. Wagg, C. L. Carilli, E. Daddi, H. Dannerbauer, L. Lentati, D. A. Riechers, M. Sargent, and F. Walter. CO(1-0) line imaging of massive star-forming disc galaxies at z=1.5-2.2. *Monthly Notices of the RAS*, 442(1):558–564, July 2014. doi: 10.1093/mnras/stu838.

Edward Argyle. A Spectrometer Survey of Atomic Hydrogen in the Andromeda Nebula. *The Astrophysical Journal*, 141:750, February 1965. doi: 10.1086/148159.

Misty C. Bentz and Sarah Katz. The agn black hole mass database. *Publications of the Astronomical Society of the Pacific*, 127(947):67–73, Jan 2015. ISSN 1538-3873. doi: 10.1086/679601. URL `http://dx.doi.org/10.1086/679601`.

Alberto D. Bolatto, Mark Wolfire, and Adam K. Leroy. The co-to-h2conversion factor. *Annual Review of Astronomy and Astrophysics*, 51(1):207–268, Aug 2013. ISSN 1545-4282. doi: 10.1146/annurev-astro-082812-140944. URL `http://dx.doi.org/10.1146/annurev-astro-082812-140944`.

M. S. Bothwell, J. Wagg, C. Cicone, R. Maiolino, P. Møller, M. Aravena, C. De Breuck, Y. Peng, D. Espada, J. A. Hodge, and et al. Allsmog: an apex low-redshift legacy survey for molecular gas – i. molecular gas scaling relations, and the effect of the co/h2 conversion factor. *Monthly Notices of the Royal Astronomical Society*, 445(3): 2599–2620, Oct 2014. ISSN 0035-8711. doi: 10.1093/mnras/stu1936. URL `http://dx.doi.org/10.1093/mnras/stu1936`.

J. Braine, F. Combes, F. Casoli, C. Dupraz, M. Gerin, U. Klein, R. Wielebinski, and N. Brouillet. A CO(1-0) and CO(2-1) survey of nearby spiral galaxies. I. Data and observations. *Astronomy and Astrophysics, Supplement*, 97:887–936, March 1993.

Joseph Cairns, Andra Stroe, Carlos De Breuck, Tony Mroczkowski, and David Clements. Large molecular gas reservoirs in star-forming cluster galaxies. *The Astrophysical Journal*, 882(2):132, Sep 2019. ISSN 1538-4357. doi: 10.3847/1538-4357/ab3392. URL `http://dx.doi.org/10.3847/1538-4357/ab3392`.

Claude Carignan, Laurent Chemin, Walter K. Huchtmeier, and Felix J. Lockman. The extended hi rotation curve and mass distribution of m31. *The Astrophysical Journal*, 641 (2):L109–L112, Mar 2006. ISSN 1538-4357. doi: 10.1086/503869. URL `http://dx.doi.org/10.1086/503869`.

C.L. Carilli and F. Walter. Cool gas in high-redshift galaxies. *Annual Review of Astronomy and Astrophysics*, 51(1):105–161, Aug 2013. ISSN 1545-4282. doi: 10.1146/annurev-astro-082812-140953. URL `http://dx.doi.org/10.1146/annurev-astro-082812-140953`.

Laurent Chemin, Claude Carignan, and Tyler Foster. Hi kinematics and dynamics of messier 31. *The Astrophysical Journal*, 705(2):1395–1415, Oct 2009. ISSN 1538-4357. doi: 10.1088/0004-637x/705/2/1395. URL `http://dx.doi.org/10.1088/0004-637X/705/2/1395`.

C. Cicone, M. Bothwell, J. Wagg, P. Møller, C. De Breuck, Z. Zhang, S. Martín, R. Maiolino, P. Severgnini, M. Aravena, and et al. The final data release of allsmog: a survey of co in typical local low-mstar-forming galaxies. *Astronomy & Astrophysics*, 604:A53, Aug 2017. ISSN 1432-0746. doi: 10.1051/0004-6361/201730605. URL http://dx.doi.org/10.1051/0004-6361/201730605.

R. I. Davies, J. Thomas, R. Genzel, F. Müller Sánchez, L. J. Tacconi, A. Sternberg, F. Eisenhauer, R. Abuter, R. Saglia, and R. Bender. The Star-forming Torus and Stellar Dynamical Black Hole Mass in the Seyfert 1 Nucleus of NGC 3227. *The Astrophysical Journal*, 646 (2):754–773, August 2006. doi: 10.1086/504963.

Daniel Foreman-Mackey, David W. Hogg, Dustin Lang, and Jonathan Goodman. emcee: The mcmc hammer. *Publications of the Astronomical Society of the Pacific*, 125(925): 306–312, Mar 2013. ISSN 1538-3873. doi: 10.1086/670067. URL http://dx.doi.org/10.1086/670067.

A Gelman, G. O. Roberts, and W. R. Gilks. Efficient metropolis jumping rules. *Bayesian Statistics*, 5:599–607, 1996b.

Jonathan Goodman and Jonathan Weare. Ensemble samplers with affine invariance. *Communications in Applied Mathematics and Computational Science*, 5(1):65–80, January 2010. doi: 10.2140/camcos.2010.5.65.

E. K. S. Hicks, R. I. Davies, W. Maciejewski, E. Emsellem, M. A. Malkan, G. Dumas, F. Müller-Sánchez, and A. Rivers. Fueling active galactic nuclei. i. how the global characteristics of the central kiloparsec of seyferts differ from quiescent galaxies. *The Astrophysical Journal*, 768(2):107, Apr 2013. ISSN 1538-4357. doi: 10.1088/0004-637x/768/2/107. URL http://dx.doi.org/10.1088/0004-637X/768/2/107.

Guinevere Kauffmann, Mei-Ling Huang, Sean Moran, and Timothy M. Heckman. A systematic study of the inner rotation curves of galaxies observed as part of the gass and cold gass surveys. *Monthly Notices of the Royal Astronomical Society*, 451(1):878–887, May 2015. ISSN 0035-8711. doi: 10.1093/mnras/stv1014. URL http://dx.doi.org/10.1093/mnras/stv1014.

John Kormendy and Luis C. Ho. Coevolution (or not) of supermassive black holes and host galaxies. *Annual Review of Astronomy and Astrophysics*, 51(1):511–653, Aug 2013. ISSN 1545-4282. doi: 10.1146/annurev-astro-082708-101811. URL http://dx.doi.org/10.1146/annurev-astro-082708-101811.

John Kormendy and Douglas Richstone. Inward Bound—The Search For Supermassive Black Holes In Galactic Nuclei. *Annual Review of Astronomy and Astrophysics*, 33:581, January 1995. doi: 10.1146/annurev.aa.33.090195.003053.

Isabella Lamperti, Amélie Saintonge, Michael Koss, Serena Viti, Christine D. Wilson, Hao He, T. Taro Shimizu, Thomas R. Greve, Richard Mushotzky, Ezequiel Treister, and et al. The co(3–2)/co(1–0) luminosity line ratio in nearby star-forming galaxies and active galactic nuclei from xcold gass, bass, and slugs. *The Astrophysical Journal*, 889(2):103, Jan 2020. ISSN 1538-4357. doi: 10.3847/1538-4357/ab6221. URL http://dx.doi.org/10.3847/1538-4357/ab6221.

Philipp Lang, Sharon E. Meidt, Erik Rosolowsky, Joseph Nofech, Eva Schinnerer, Adam K. Leroy, Eric Emsellem, Ismael Pessa, Simon C. O. Glover, Brent Groves, and et al. Phangs co kinematics: Disk orientations and rotation curves at 150 pc resolution. *The Astrophysical Journal*, 897(2):122, Jul 2020. ISSN 1538-4357. doi: 10.3847/1538-4357/ab9953. URL http://dx.doi.org/10.3847/1538-4357/ab9953.

Tod R. Lauer, Marc Postman, Harold A. Weaver, John R. Spencer, S. Alan Stern, Marc W. Buie, Daniel D. Durda, Carey M. Lisse, A. R. Poppe, Richard P. Binzel, and et al. New horizons observations of the cosmic optical background. *The Astrophysical Journal*, 906 (2):77, Jan 2021. ISSN 1538-4357. doi: 10.3847/1538-4357/abc881. URL http://dx.doi.org/10.3847/1538-4357/abc881.

Adam K. Leroy, Fabian Walter, Frank Bigiel, Antonio Usero, Axel Weiss, Elias Brinks, W. J. G. de Blok, Robert C. Kennicutt, Karl-Friedrich Schuster, Carsten Kramer, and et al. Heracles: The hera co line extragalactic survey. *The Astronomical Journal*, 137 (6):4670–4696, Apr 2009. ISSN 1538-3881. doi: 10.1088/0004-6256/137/6/4670. URL http://dx.doi.org/10.1088/0004-6256/137/6/4670.

Nanyao Lu, Yinghe Zhao, Tanio Díaz-Santos, C. Kevin Xu, Yu Gao, Lee Armus, Kate G. Isaak, Joseph M. Mazzarella, Paul P. van der Werf, Philip N. Appleton, and et al. A herschel space observatory spectral line survey of local luminous infrared galaxies from 194 to 671 microns. *The Astrophysical Journal Supplement Series*, 230(1):1, May 2017. ISSN 1538-4365. doi: 10.3847/1538-4365/aa6476. URL http://dx.doi.org/10.3847/1538-4365/aa6476.

N. Mashian, E. Sturm, A. Sternberg, A. Janssen, S. Hailey-Dunsheath, J. Fischer, A. Contursi, E. González-Alfonso, J. Graciá-Carpio, A. Poglitsch, and et al. High-jco sleds in nearby infrared bright galaxies observed byherschel/pacs. *The Astrophysical Journal*, 802(2):81, Mar 2015. ISSN 1538-4357. doi: 10.1088/0004-637x/802/2/81. URL http://dx.doi.org/10.1088/0004-637X/802/2/81.

Nicholas Metropolis, Arianna W. Rosenbluth, Marshall N. Rosenbluth, Augusta H. Teller, and Edward Teller. Equation of State Calculations by Fast Computing Machines. *The Journey of Chemical Physics*, 21(6):1087–1092, June 1953. doi: 10.1063/1.1699114.

Ch. Nieten, N. Neininger, M. Guélin, H. Ungerechts, R. Lucas, E. M. Berkhuijsen, R. Beck, and R. Wielebinski. Molecular gas in the andromeda galaxy. *Astronomy & Astrophysics*, 453(2):459–475, Jun 2006. ISSN 1432-0746. doi: 10.1051/0004-6361:20035672. URL http://dx.doi.org/10.1051/0004-6361:20035672.

Bradley M. Peterson. *An Introduction to Active Galactic Nuclei.* Cambridge University Press, 1997. doi: 10.1017/CBO9781139170901.

V. Ramakrishnan, N. M. Nagar, C. Finlez, T. Storchi-Bergmann, R. Slater, A. Schnorr-Müller, R. A. Riffel, C. G. Mundell, and A. Robinson. Nuclear kinematics in nearby agn – i. an alma perspective on the morphology and kinematics of the molecular co(2–1) emission. *Monthly Notices of the Royal Astronomical Society*, 487(1):444–455, May 2019. ISSN 1365-2966. doi: 10.1093/mnras/stz1244. URL http://dx.doi.org/10.1093/mnras/stz1244.

E. Schinnerer, A. Eckart, and L. J. Tacconi. Distribution and kinematics of the circumnuclear molecular gas in the seyfert 1 galaxy ngc 3227. *The Astrophysical Journal*, 533(2):826–849,

Apr 2000. ISSN 1538-4357. doi: 10.1086/308703. URL http://dx.doi.org/10.1086/308703.

Marc S. Seigar, Aaron J. Barth, and James S. Bullock. A revised λ cdm mass model for the andromeda galaxy. *Monthly Notices of the Royal Astronomical Society*, 389(4): 1911–1923, Sep 2008. ISSN 0035-8711. doi: 10.1111/j.1365-2966.2008.13732.x. URL http://dx.doi.org/10.1111/j.1365-2966.2008.13732.x.

Gauri Sharma, Paolo Salucci, C. M. Harrison, Glenn van de Ven, and Andrea Lapi. Flat rotation curves of $z \sim 1$ star-forming galaxies and evidence of disk-scale length evolution, 2021.

P. M. Solomon, D. Downes, S. J. E. Radford, and J. W. Barrett. The molecular interstellar medium in ultraluminous infrared galaxies. *The Astrophysical Journal*, 478(1):144–161, Mar 1997. ISSN 1538-4357. doi: 10.1086/303765. URL http://dx.doi.org/10.1086/303765.

Linda S. Sparke and John S. Gallagher, III. *Galaxies in the Universe: An Introduction*. Cambridge University Press, 2 edition, 2007. doi: 10.1017/CBO9780511807237.

I. M. Stewart, S.-L. Blyth, and W. J. G. de Blok. A simple model for global hi profiles of galaxies. *Astronomy & Astrophysics*, 567:A61, Jul 2014. ISSN 1432-0746. doi: 10.1051/0004-6361/201423602. URL http://dx.doi.org/10.1051/0004-6361/201423602.

Fabian Walter, Elias Brinks, W. J. G. de Blok, Frank Bigiel, Robert C. Kennicutt, Michele D. Thornley, and Adam Leroy. Things: The h i nearby galaxy survey. *The Astronomical Journal*, 136(6):2563–2647, Nov 2008. ISSN 1538-3881. doi: 10.1088/0004-6256/136/6/2563. URL http://dx.doi.org/10.1088/0004-6256/136/6/2563.

Judith S. Young, Shuding Xie, Linda Tacconi, Pat Knezek, Paul Viscuso, Lowell Tacconi-Garman, Nick Scoville, Steve Schneider, F. Peter Schloerb, Steve Lord, Amy Lesser, Jeff Kenney, Yi-Long Huang, Nick Devereux, Mark Claussen, James Case, John Carpenter, Mike Berry, and Lori Allen. The FCRAO Extragalactic CO Survey. I. The Data. *The Astrophysical Journal*, 98:219, May 1995. doi: 10.1086/192159.

Appendix A: Sample CO spectra

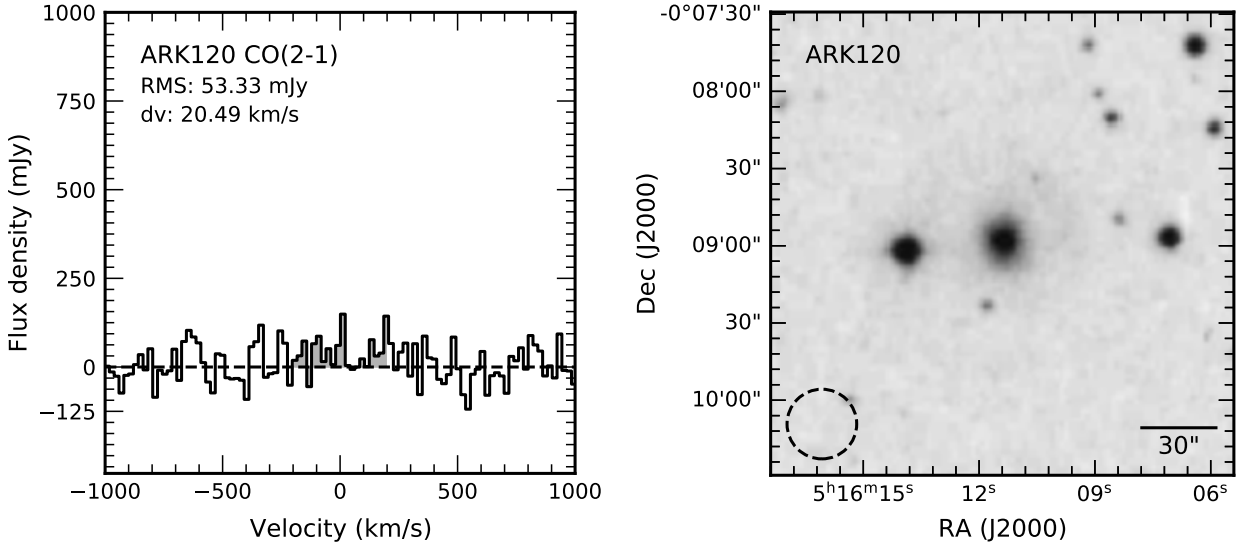

Fig. A.1: Left: The reduced APEX CO(2-1) and CO(3-2) spectra. The RMS (in mJy) and velocity resolution per channel $\delta v_{\rm chan}$ (in $\mathrm{km\,s^{-1}}$) are shown in the upper left corner. The shaded region below the flux shows the integration range used in the line flux measurements in Section 3.4. Right: Optical DSS survey cutout centered on the galaxy in question. North is up and east is left. The size of the 230 GHz and 345 GHz APEX beam is shown by the dashed circle in the lower left.

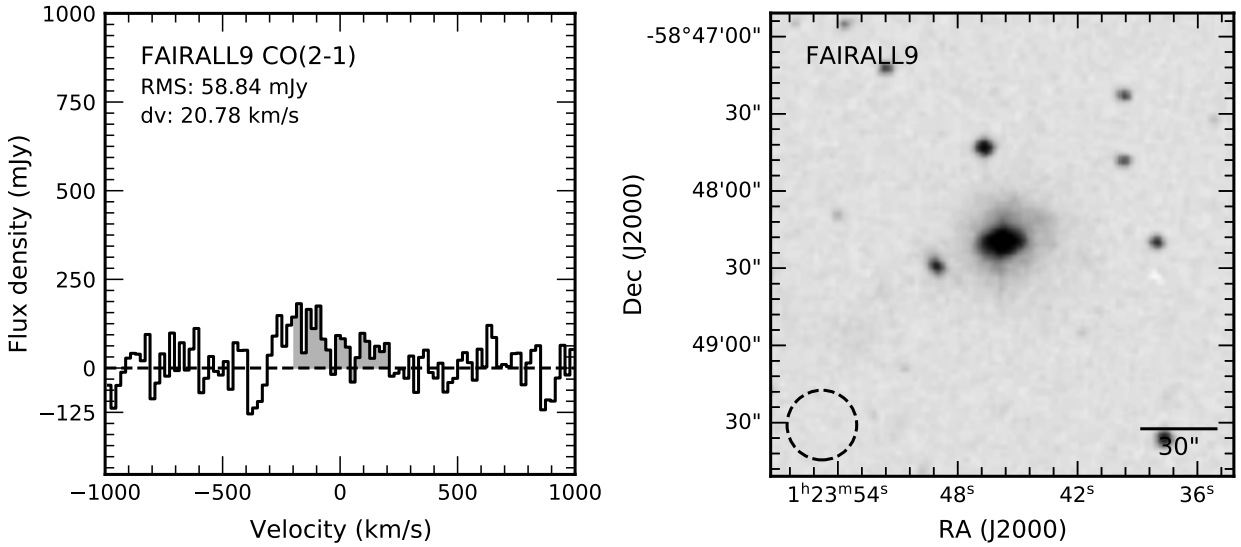

Fig. A.2: Same as in Fig. A.1, but for Fairall 9 CO(2-1).

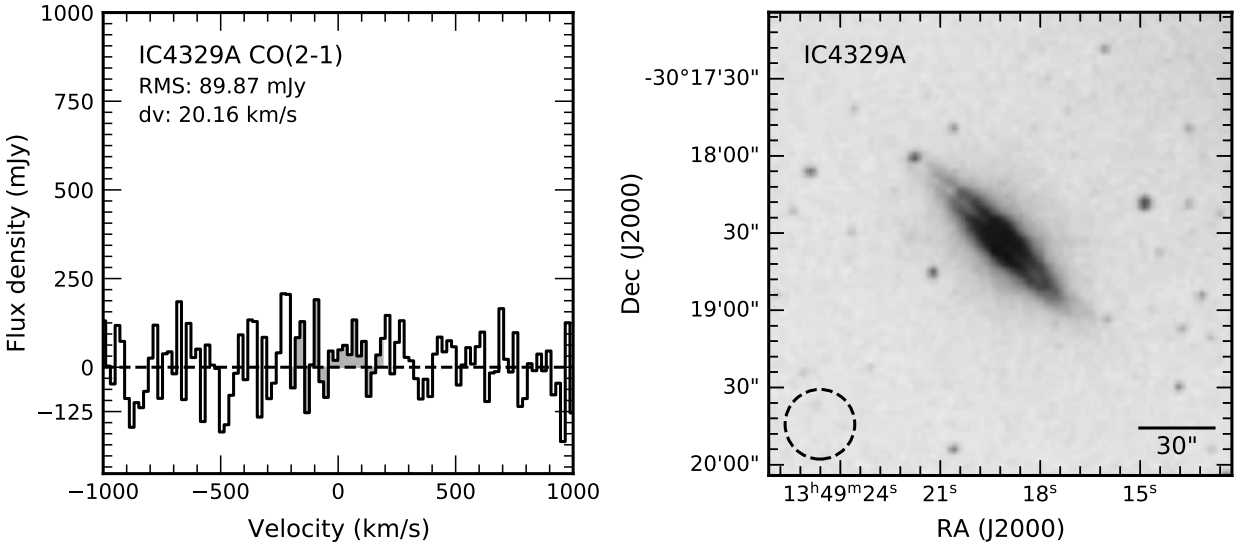

Fig. A.3: Same as in Fig. A.1, but for Fairall 9 CO(2-1).

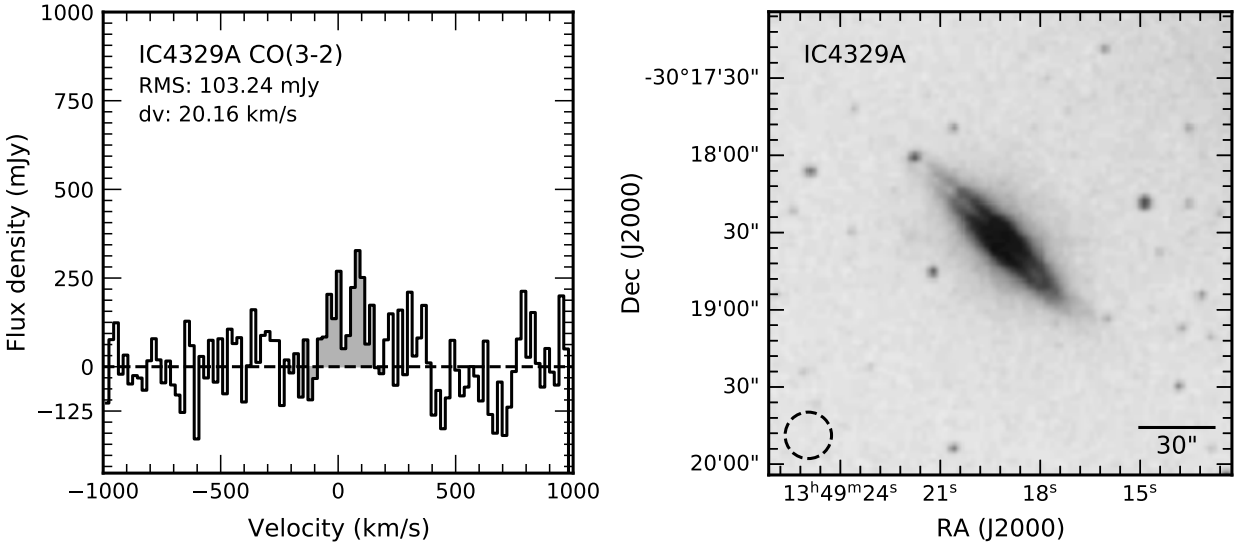

Fig. A.4: Same as in Fig. A.1, but for Fairall 9 CO(2-1).

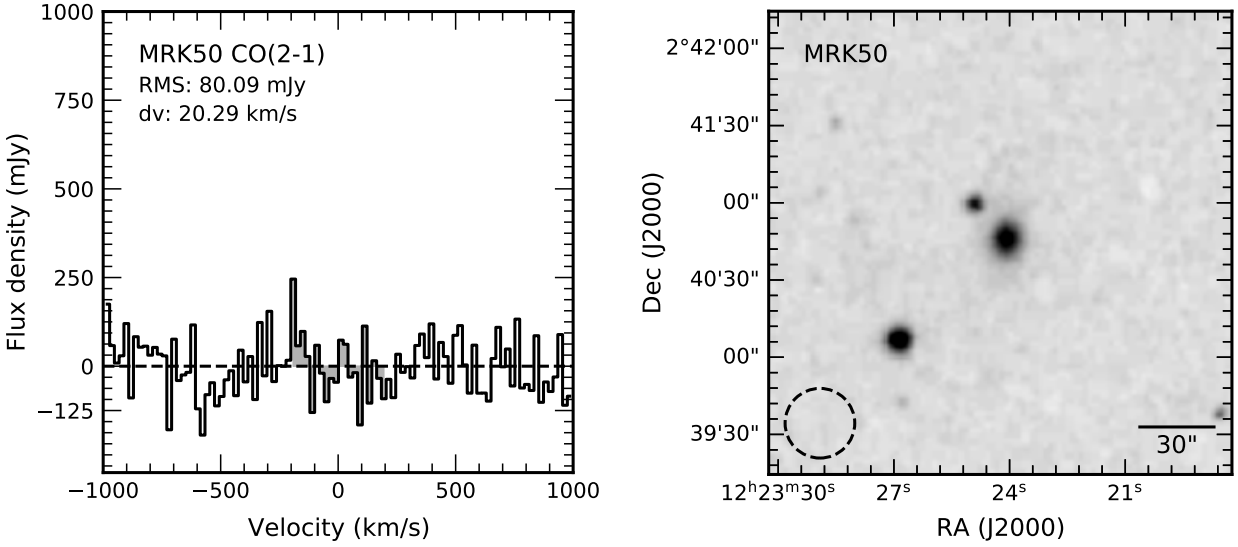

Fig. A.5: Same as in Fig. A.1, but for Fairall 9 CO(2-1).

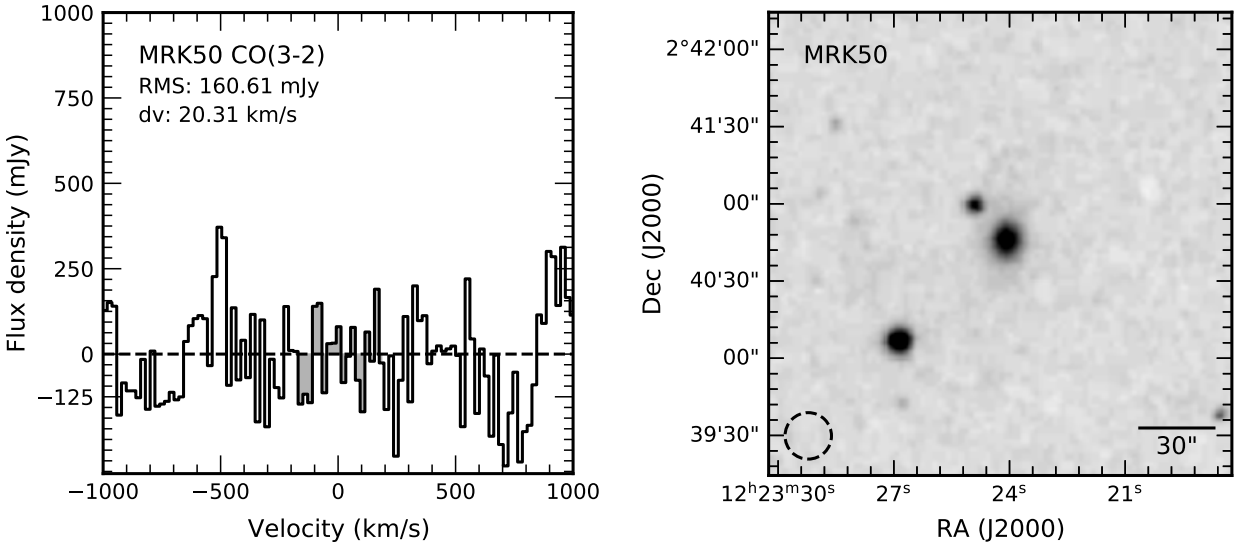

Fig. A.6: Same as in Fig. A.1, but for Fairall 9 CO(2-1).

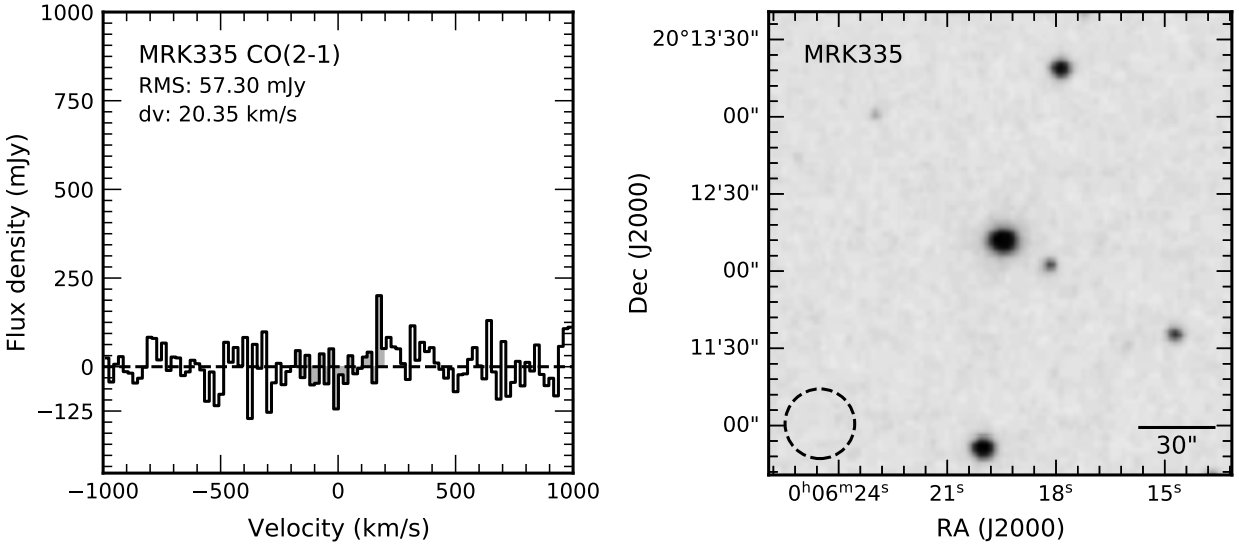

Fig. A.7: Same as in Fig. A.1, but for Fairall 9 CO(2-1).

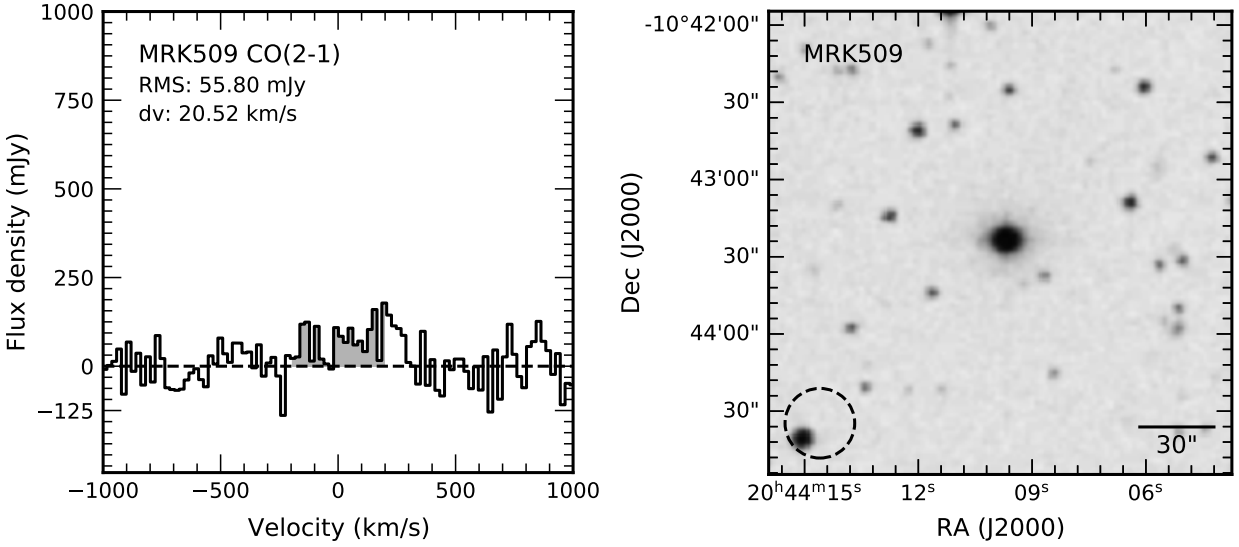

Fig. A.8: Same as in Fig. A.1, but for Fairall 9 CO(2-1).

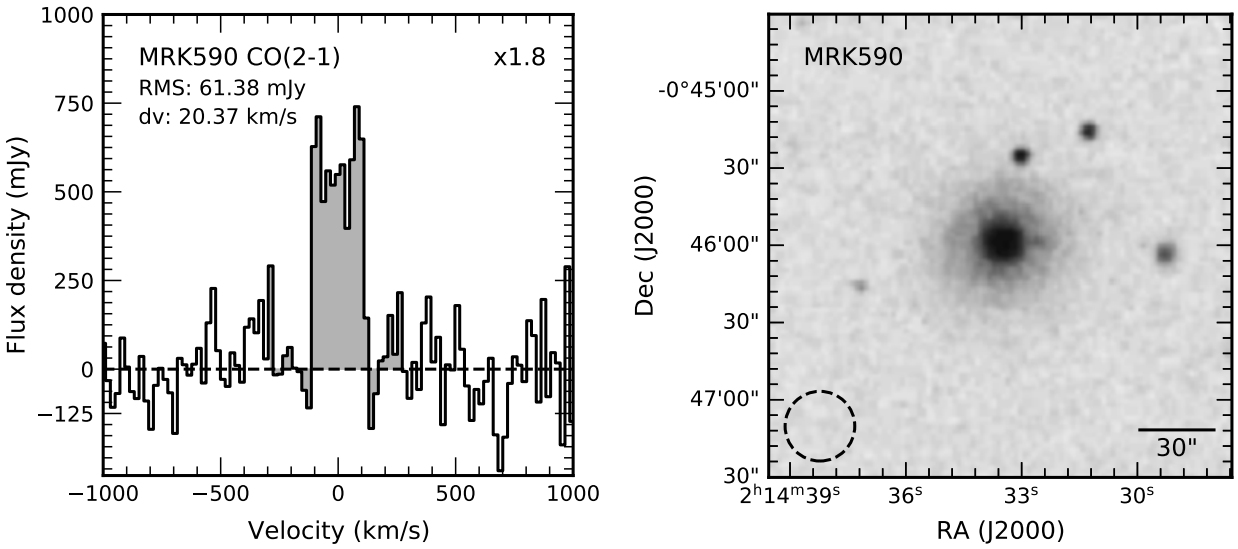

Fig. A.9: Same as in Fig. A.1, but for Fairall 9 CO(2-1).

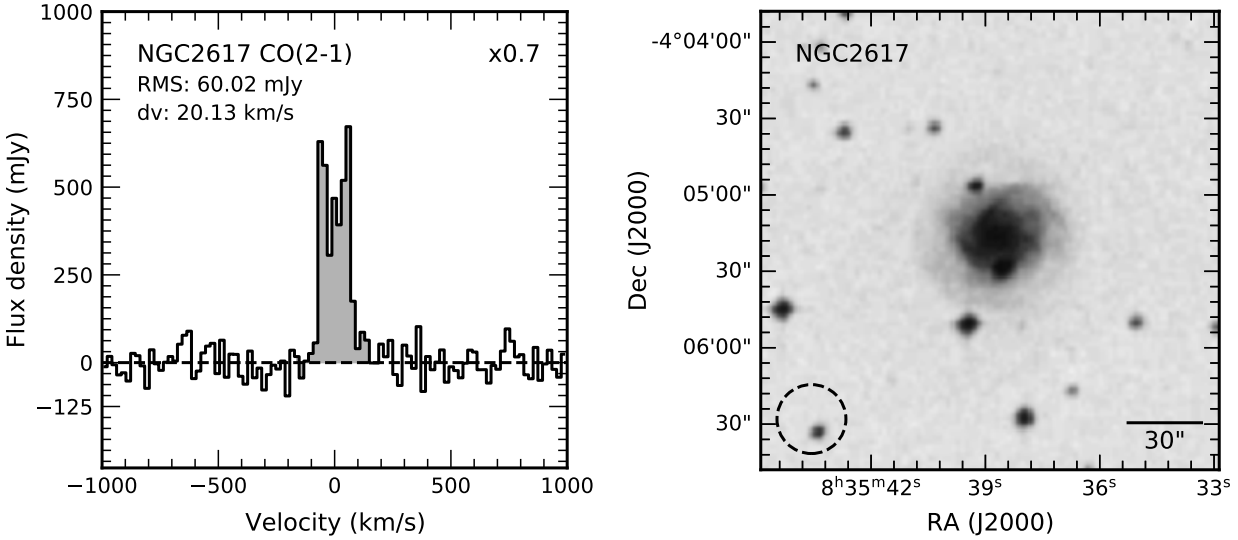

Fig. A.10: Same as in Fig. A.1, but for Fairall 9 CO(2-1).

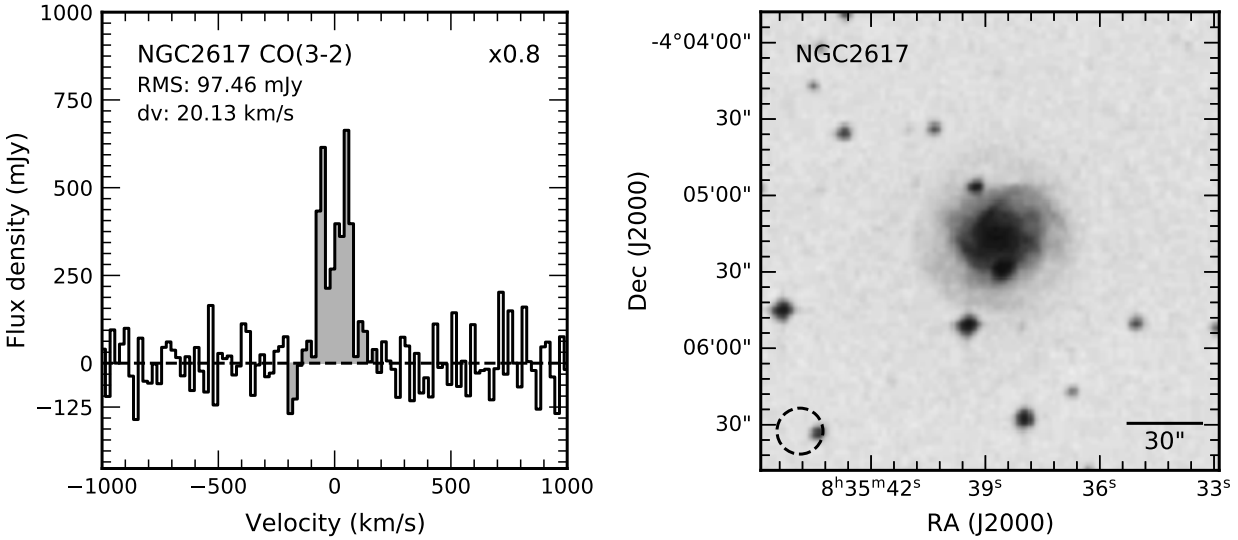

Fig. A.11: Same as in Fig. A.1, but for Fairall 9 CO(2-1).

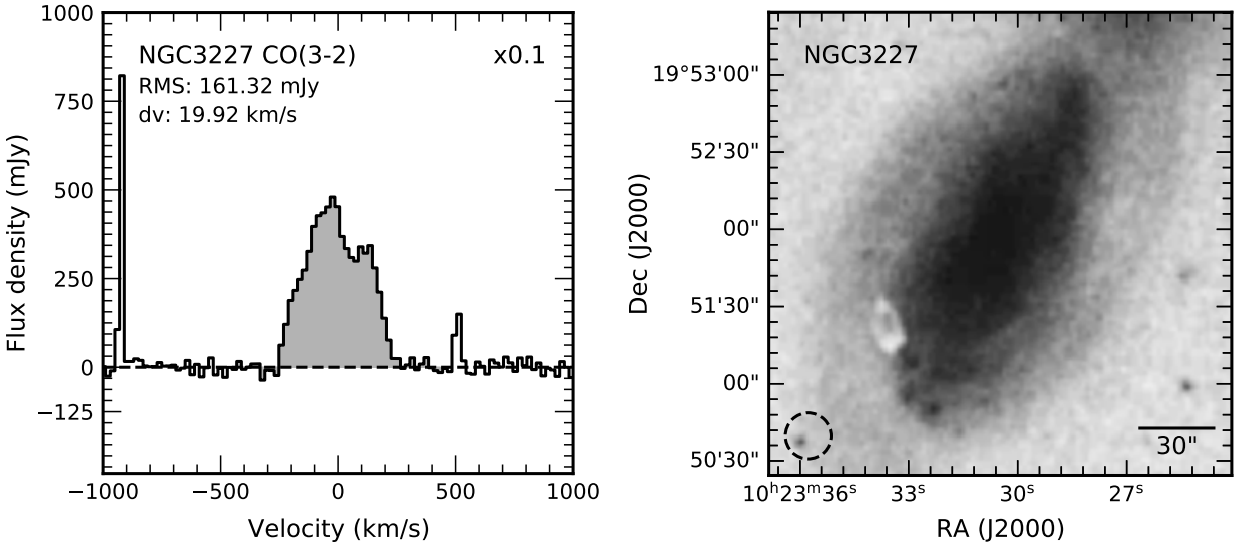

Fig. A.12: Same as in Fig. A.1, but for Fairall 9 CO(2-1).

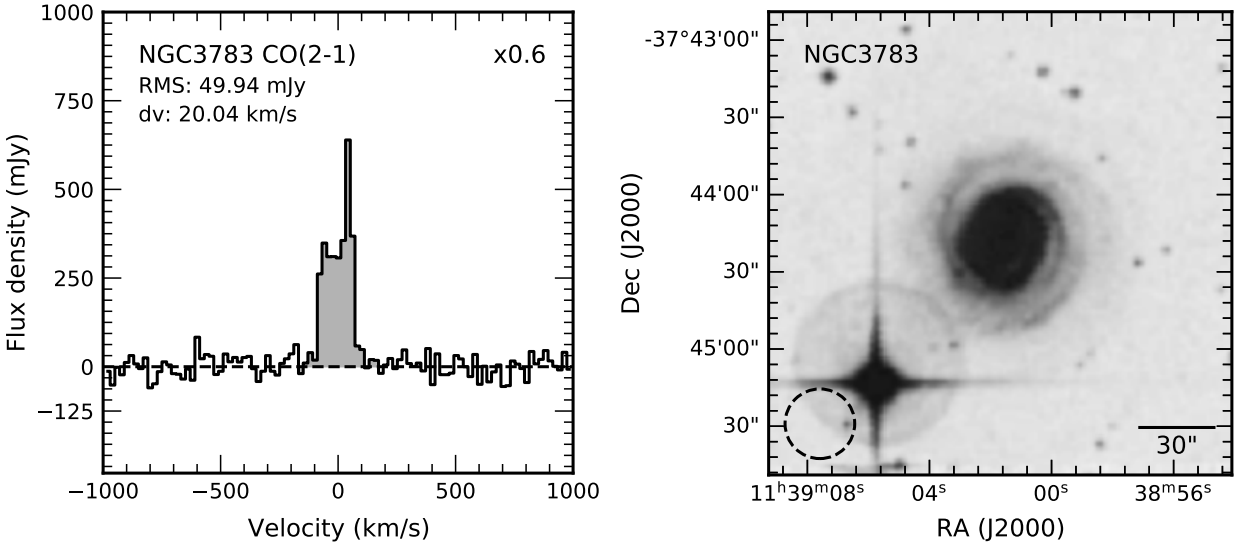

Fig. A.13: Same as in Fig. A.1, but for Fairall 9 CO(2-1).

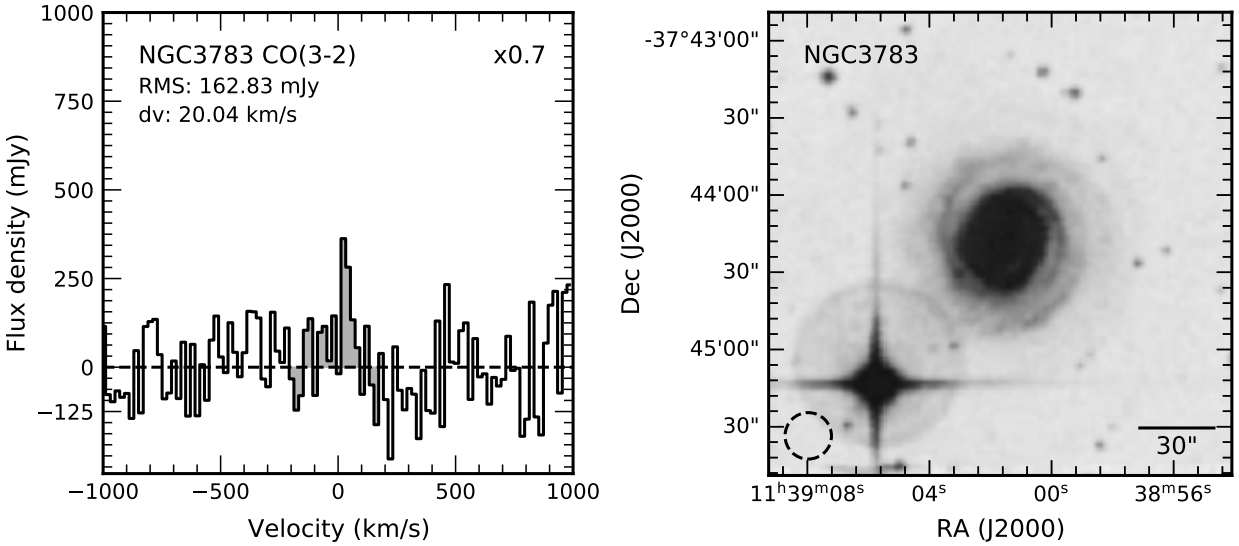

Fig. A.14: Same as in Fig. A.1, but for Fairall 9 CO(2-1).

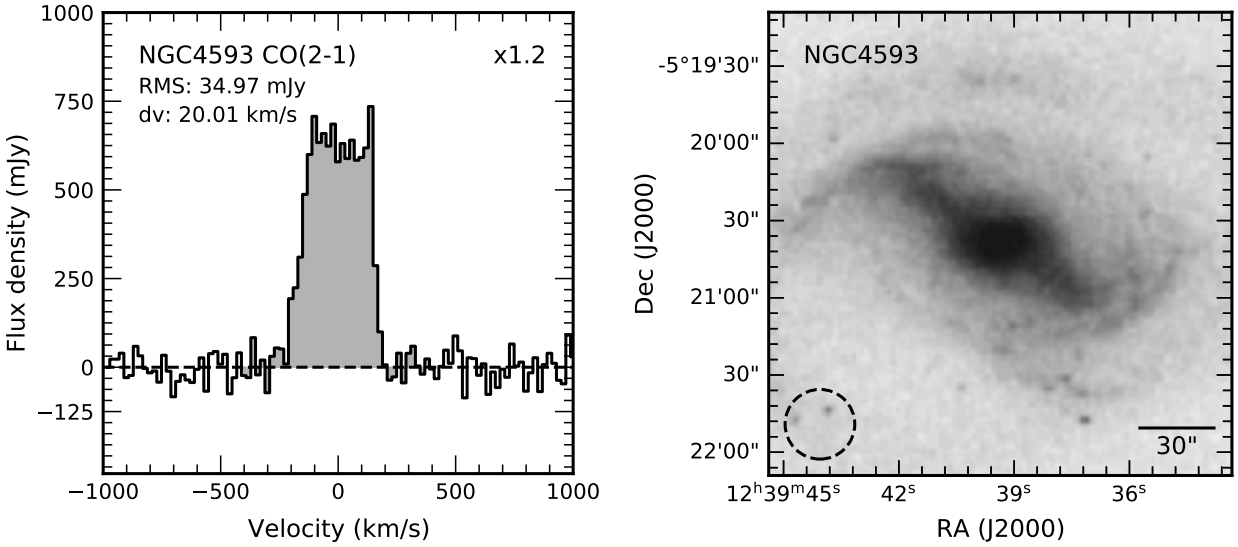

Fig. A.15: Same as in Fig. A.1, but for Fairall 9 CO(2-1).

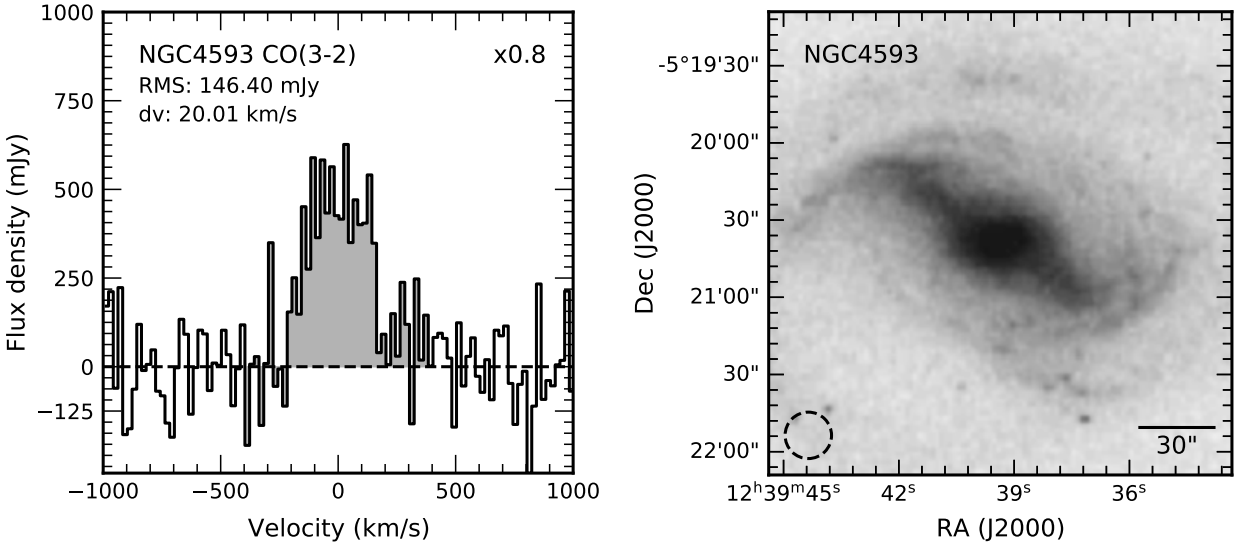

Fig. A.16: Same as in Fig. A.1, but for Fairall 9 CO(2-1).

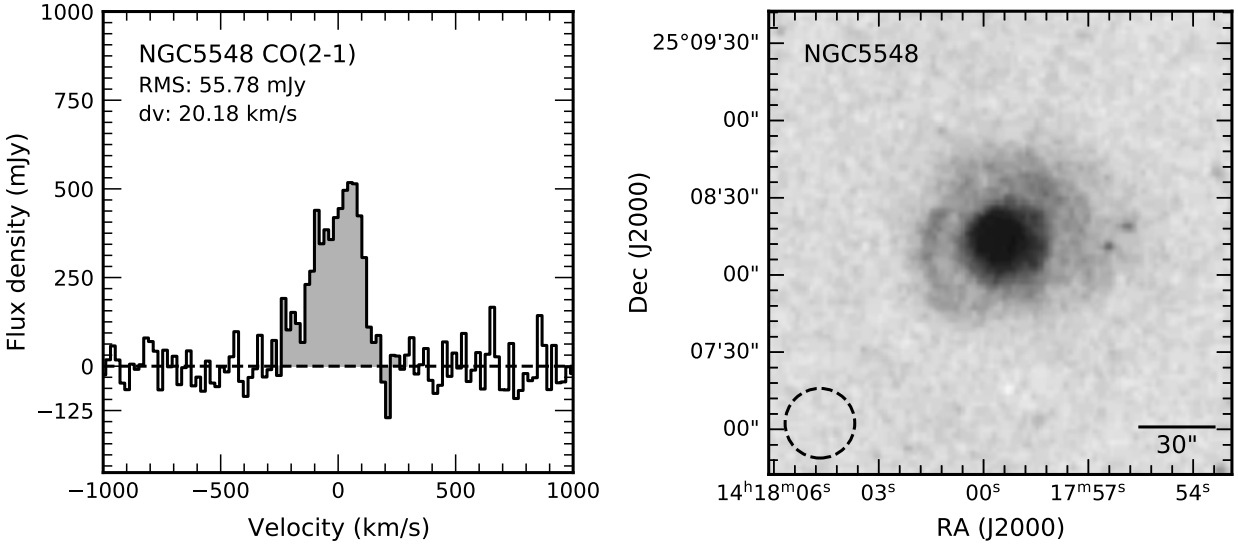

Fig. A.17: Same as in Fig. A.1, but for Fairall 9 CO(2-1).

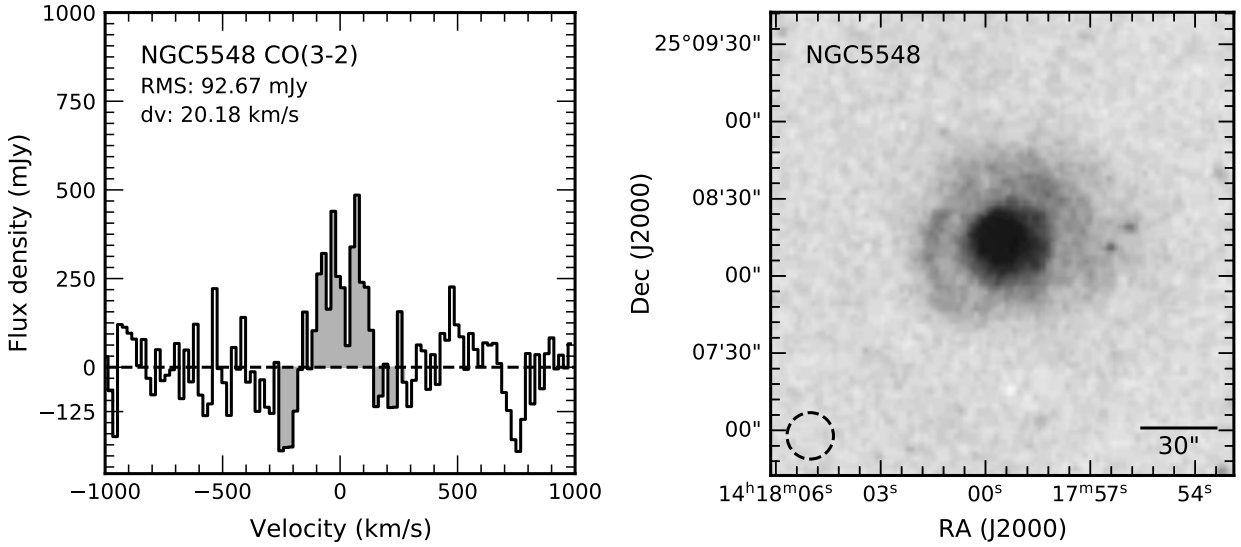

Fig. A.18: Same as in Fig. A.1, but for Fairall 9 CO(2-1).

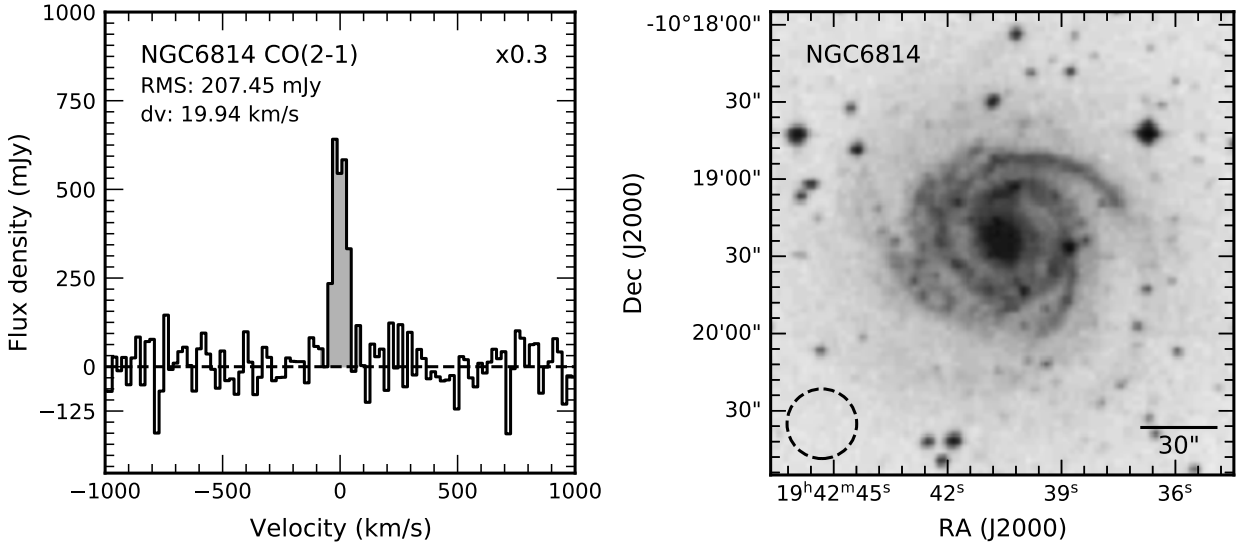

Fig. A.19: Same as in Fig. A.1, but for Fairall 9 CO(2-1).

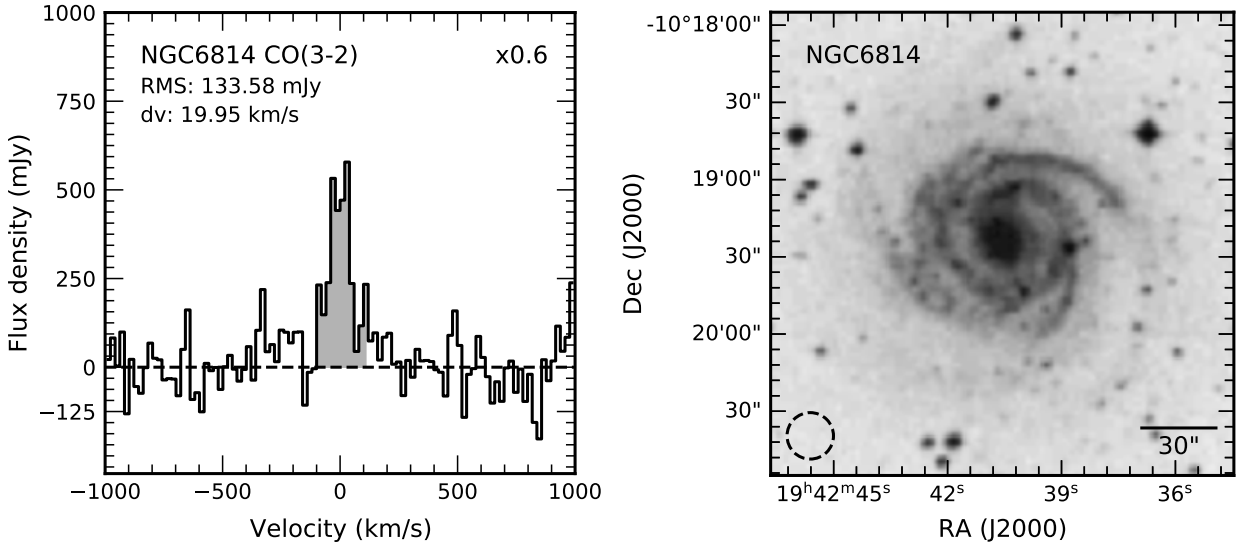

Fig. A.20: Same as in Fig. A.1, but for Fairall 9 CO(2-1).

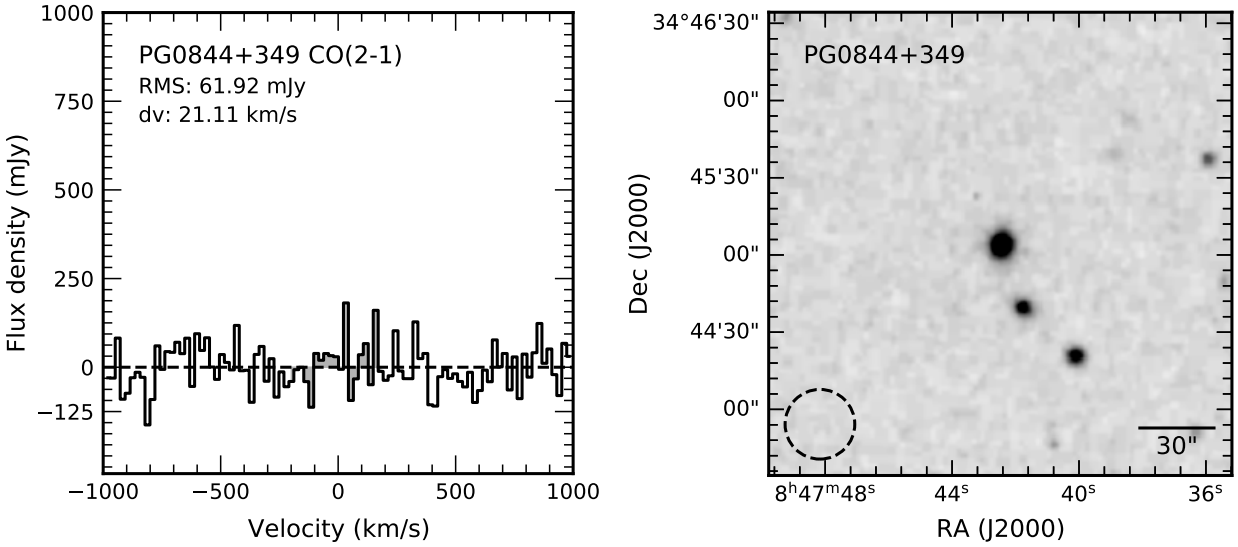

Fig. A.21: Same as in Fig. A.1, but for Fairall 9 CO(2-1).

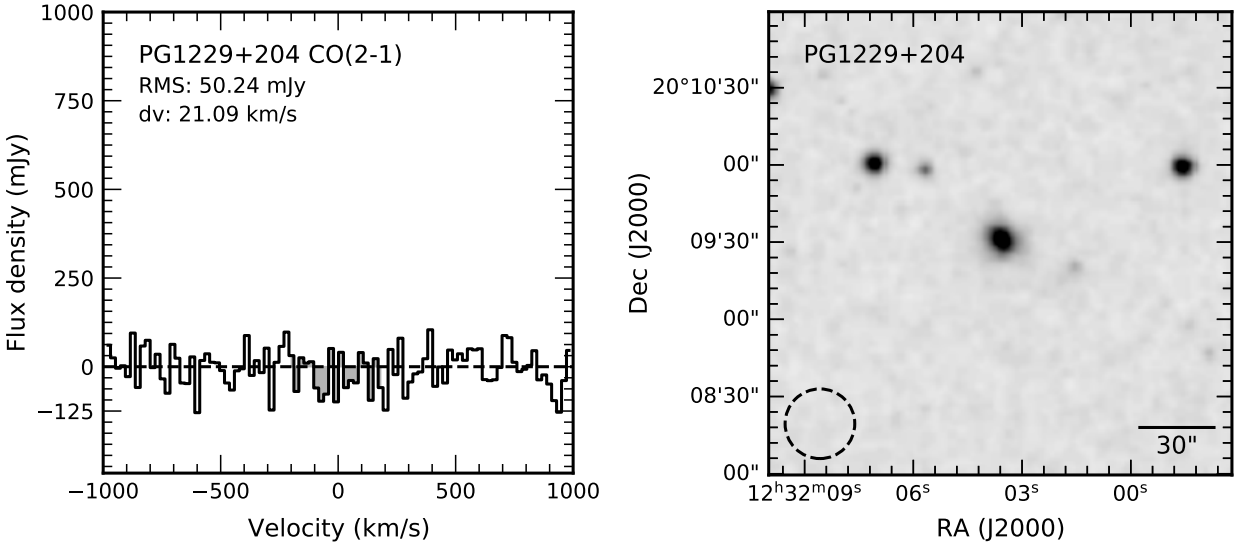

Fig. A.22: Same as in Fig. A.1, but for Fairall 9 CO(2-1).

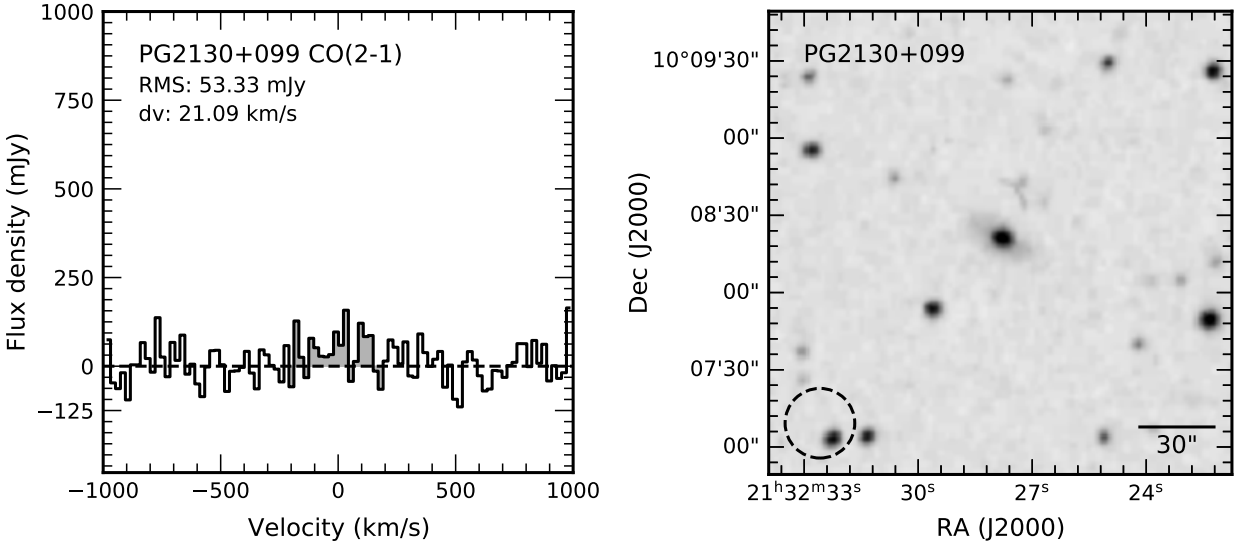

Fig. A.23: Same as in Fig. A.1, but for Fairall 9 CO(2-1).

Appendix B: MCMC plots

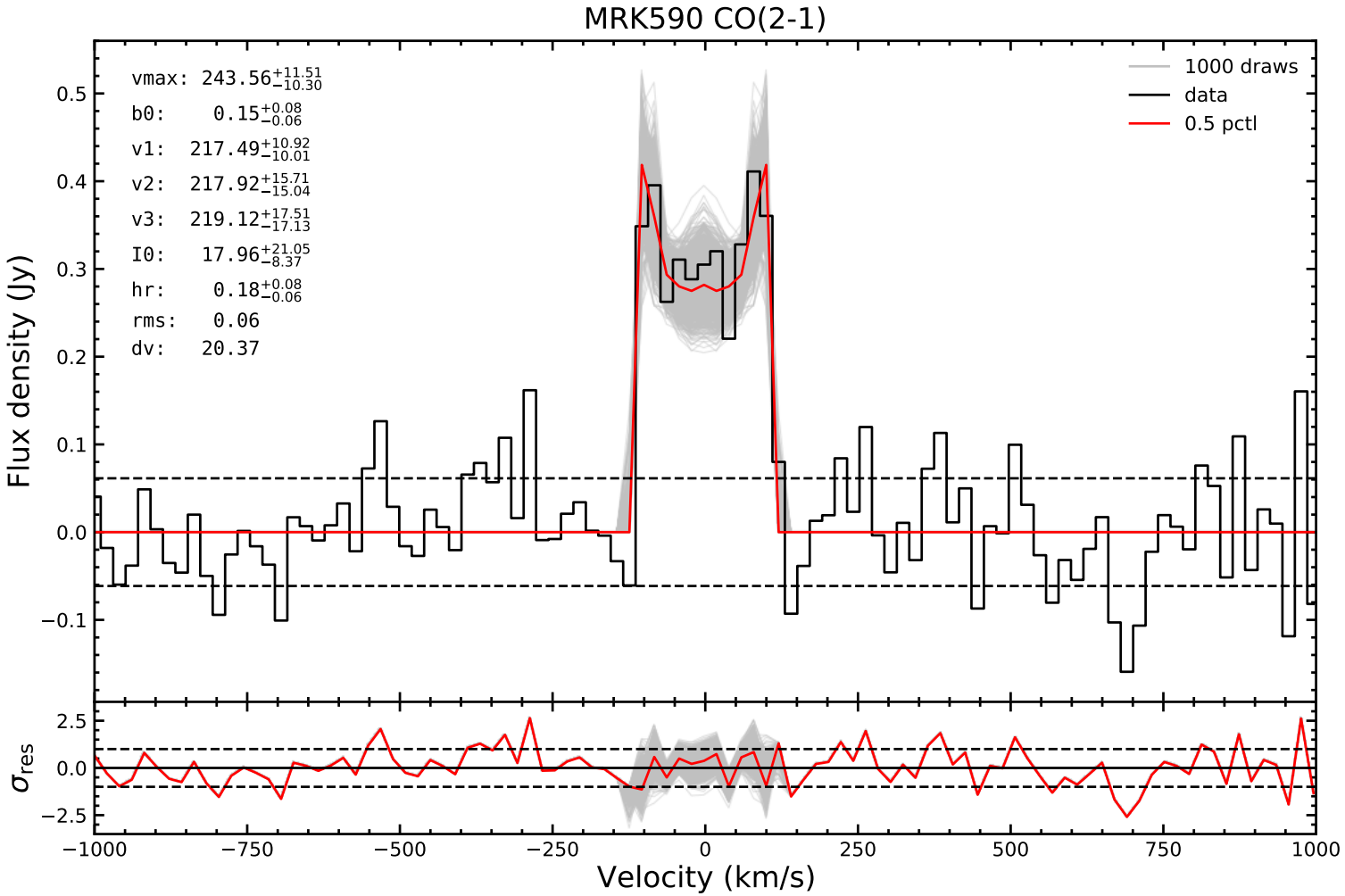

Fig. B.1: The global CO line profiles of each galaxy, along with a solid red line indicating the model produced from the 50th percentile of the posterior distribution. A set of 1000 randomly drawn samples from the posterior distribution is shown by the gray shadow. The bottom panel shows the residuals of the fit. The horizontal dashed lines indicate the $\pm 1\sigma$ residuals.

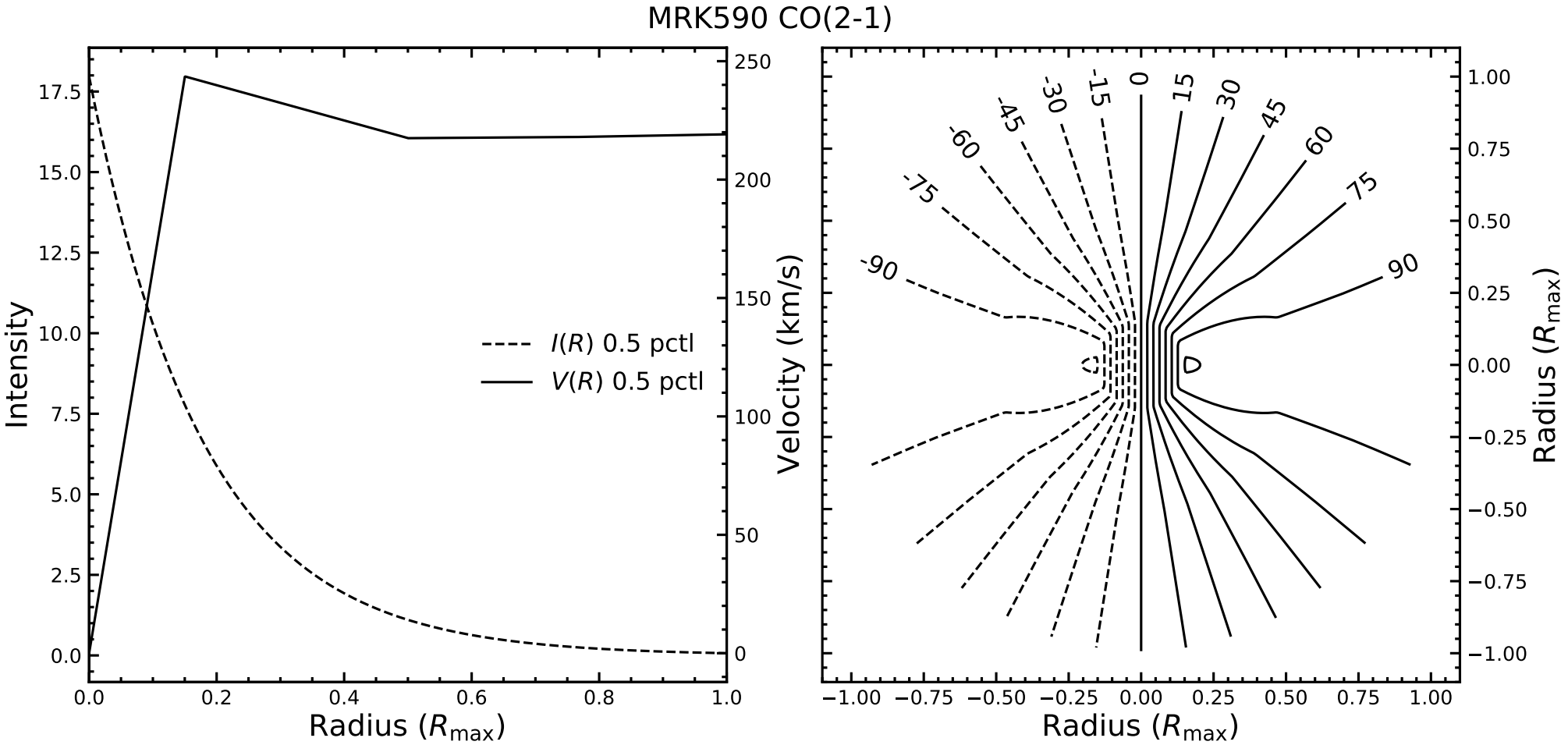

Fig. B.2: Left: Rotation curve and intensity profile constructed from the model evaluated by the 50th percentile of the posterior distribution. Right: Spider diagram showing radial velocity contours of the simulated CO gas, constructed from the model evaluated by the 50th percentile of the posterior distribution.

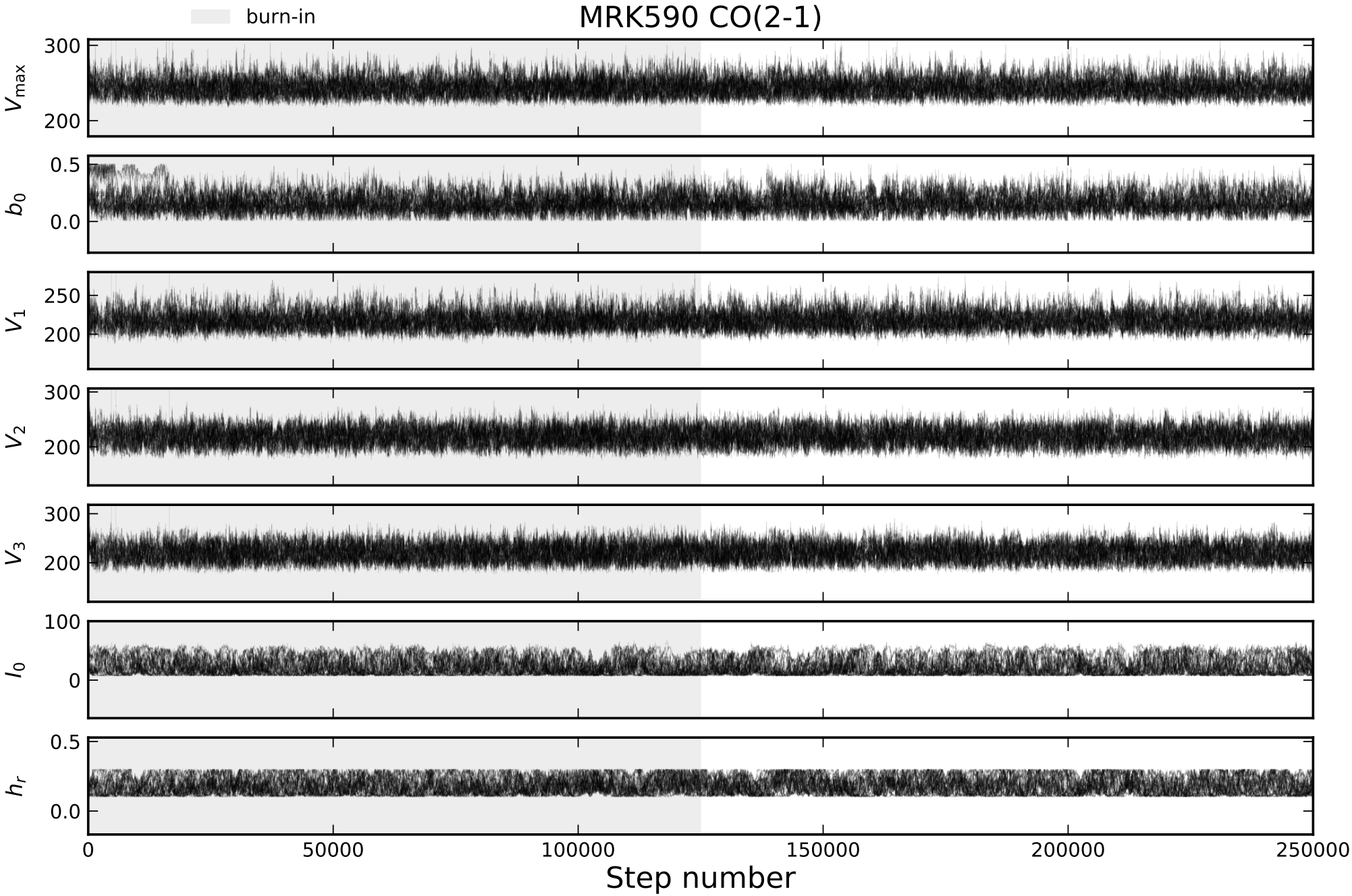

Fig. B.3: The model parameters as a function of step number, as the 15 walkers explore the posterior distribution. The gray shadow indicates the burn-in region.

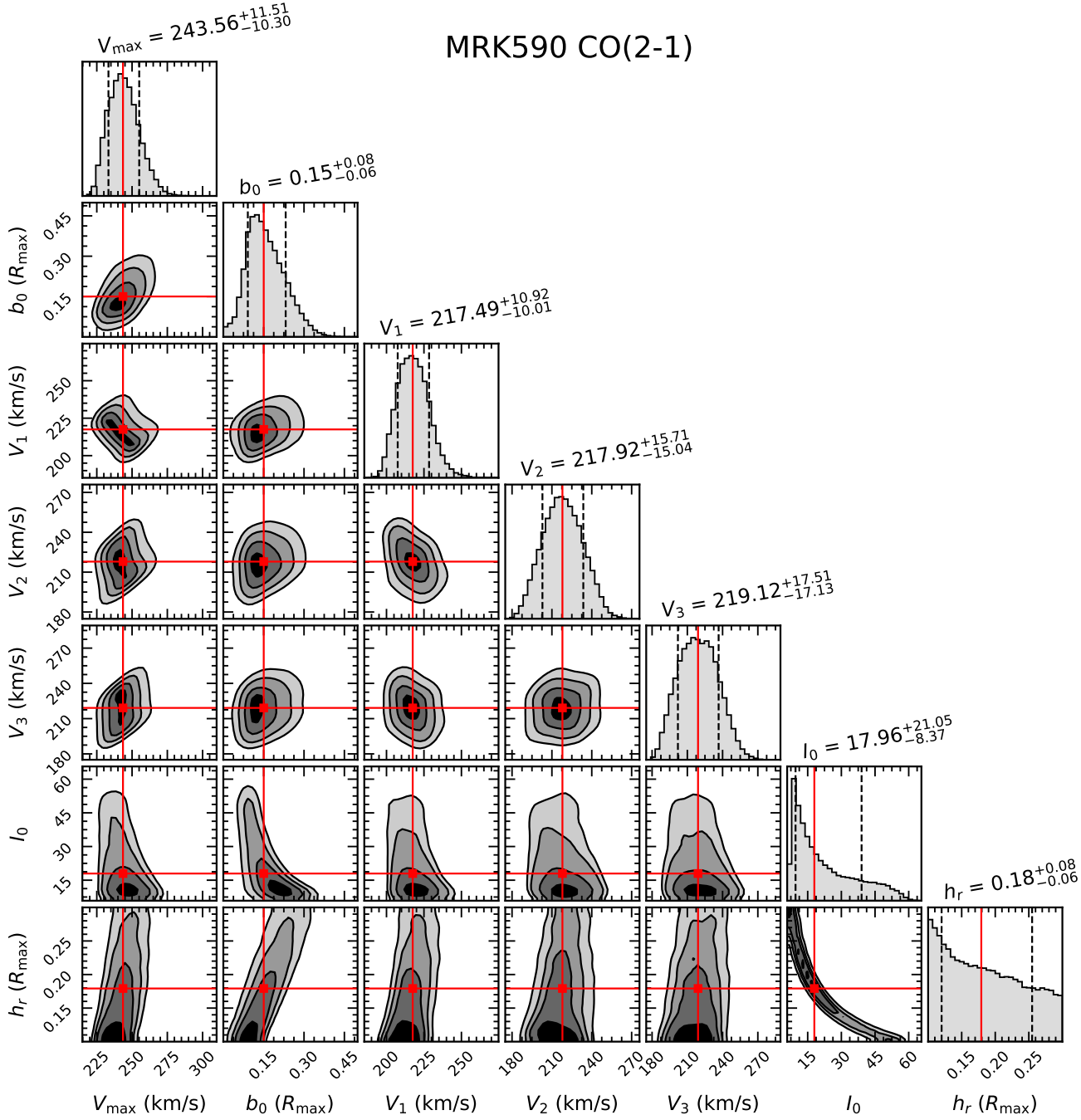

Fig. B.4: Corner plot showing both the 2D covariances among the parameters in the model, as well as the marginalized 1D distributions of individual parameters. The solid red lines indicate the 50th (median) of the marginalized posterior distributions. The vertical dashed lines indicate the 16th, and 84th percentiles (coresponding to the $\pm1\sigma$ credible intervals). Median values and their $\pm1\sigma$ errors are shown on the top of each 1D histogram.

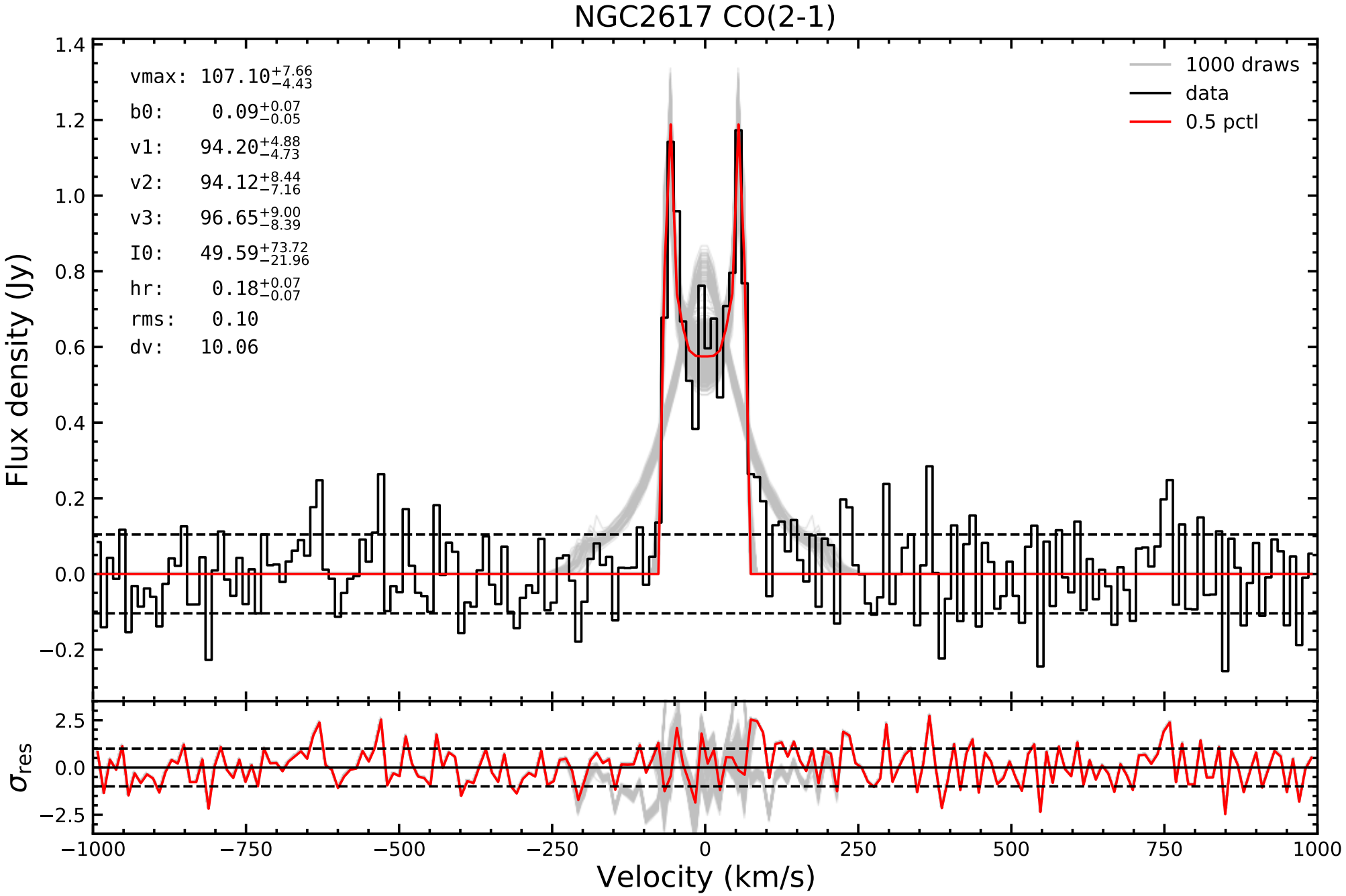

Fig. B.5: Same as Fig. B.1, but for NGC 2617 CO(2-1).

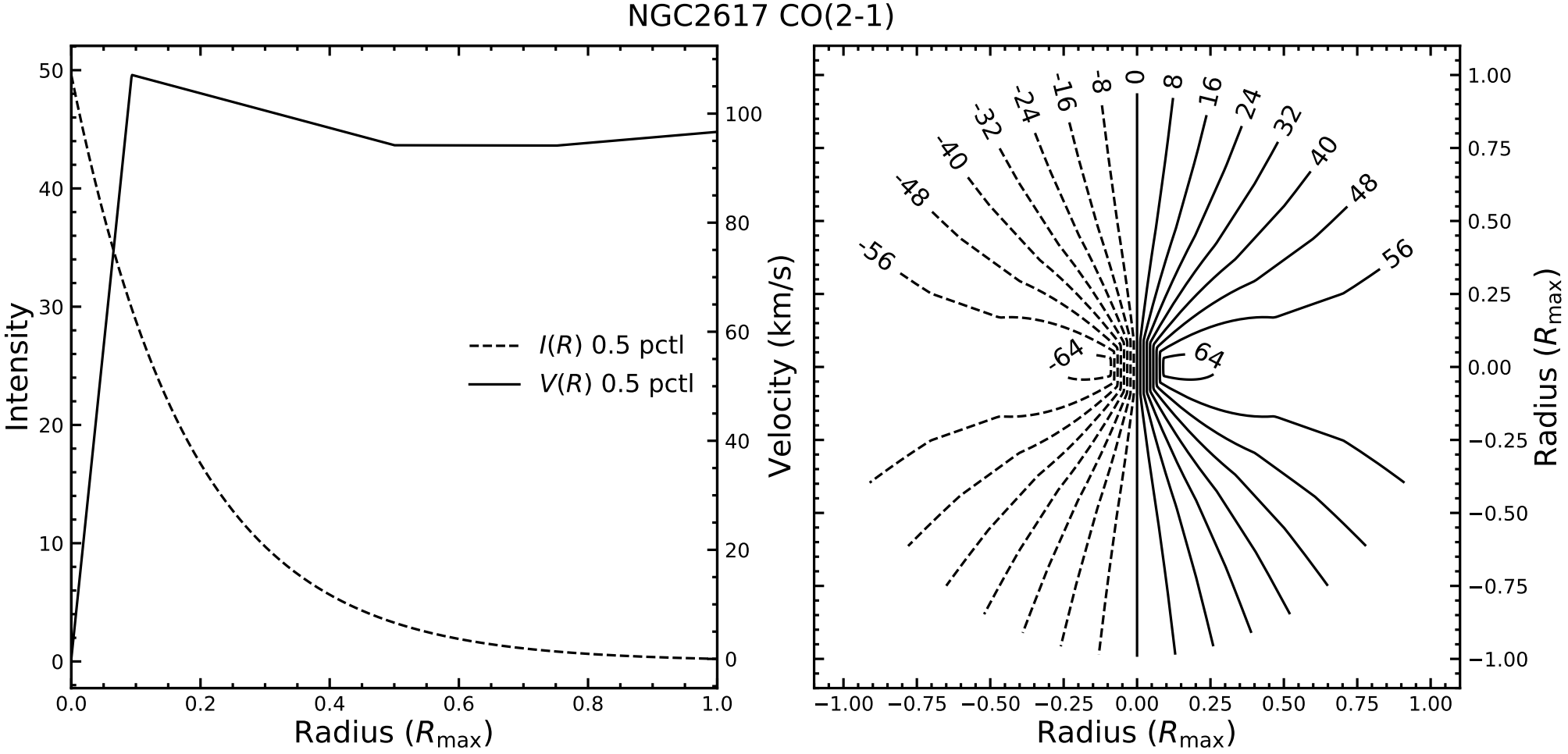

Fig. B.6: Same as Fig. B.2, but for NGC 2617 CO(2-1).

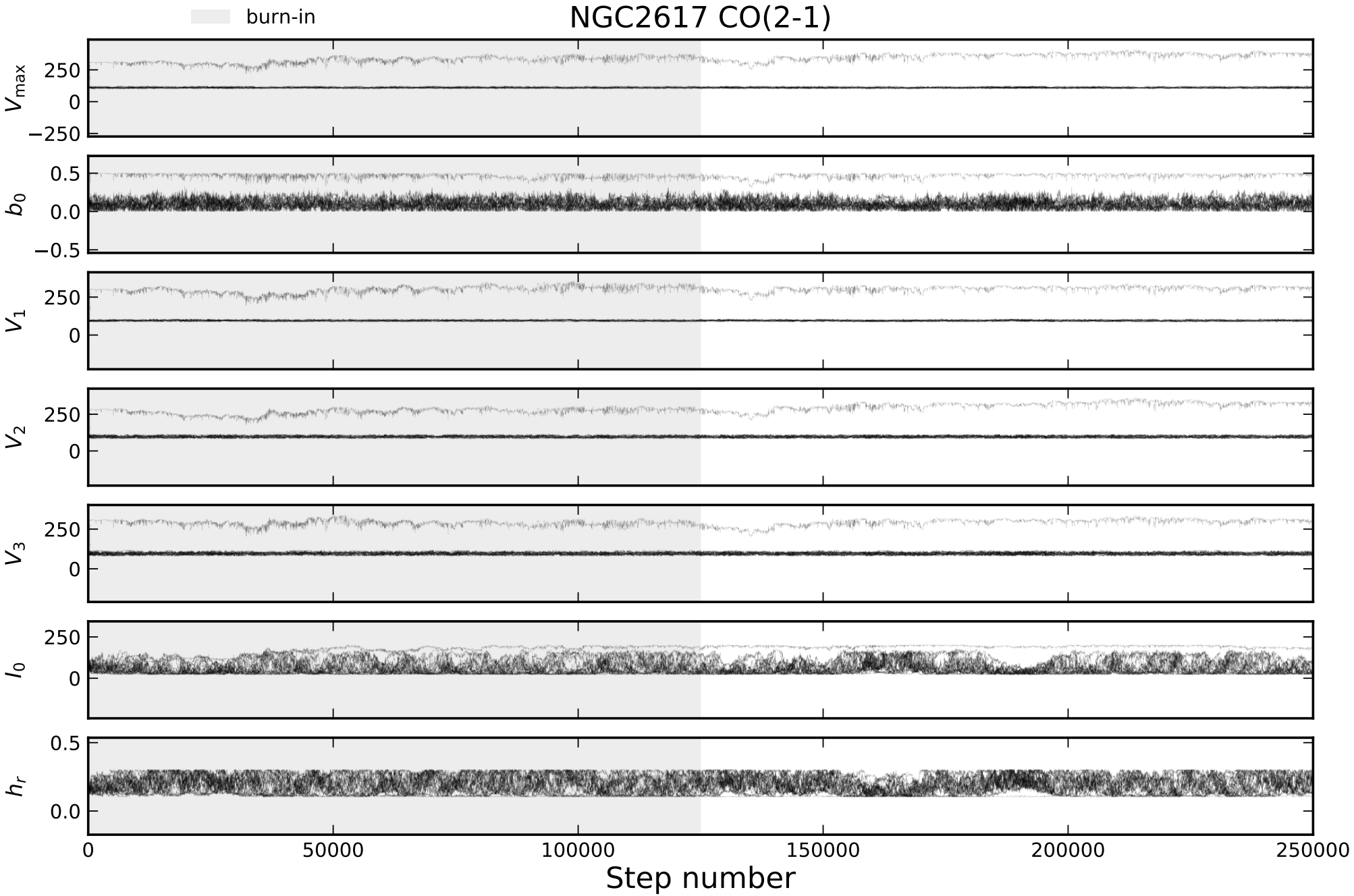

Fig. B.7: Same as Fig. B.3, but for NGC 2617 CO(2-1).

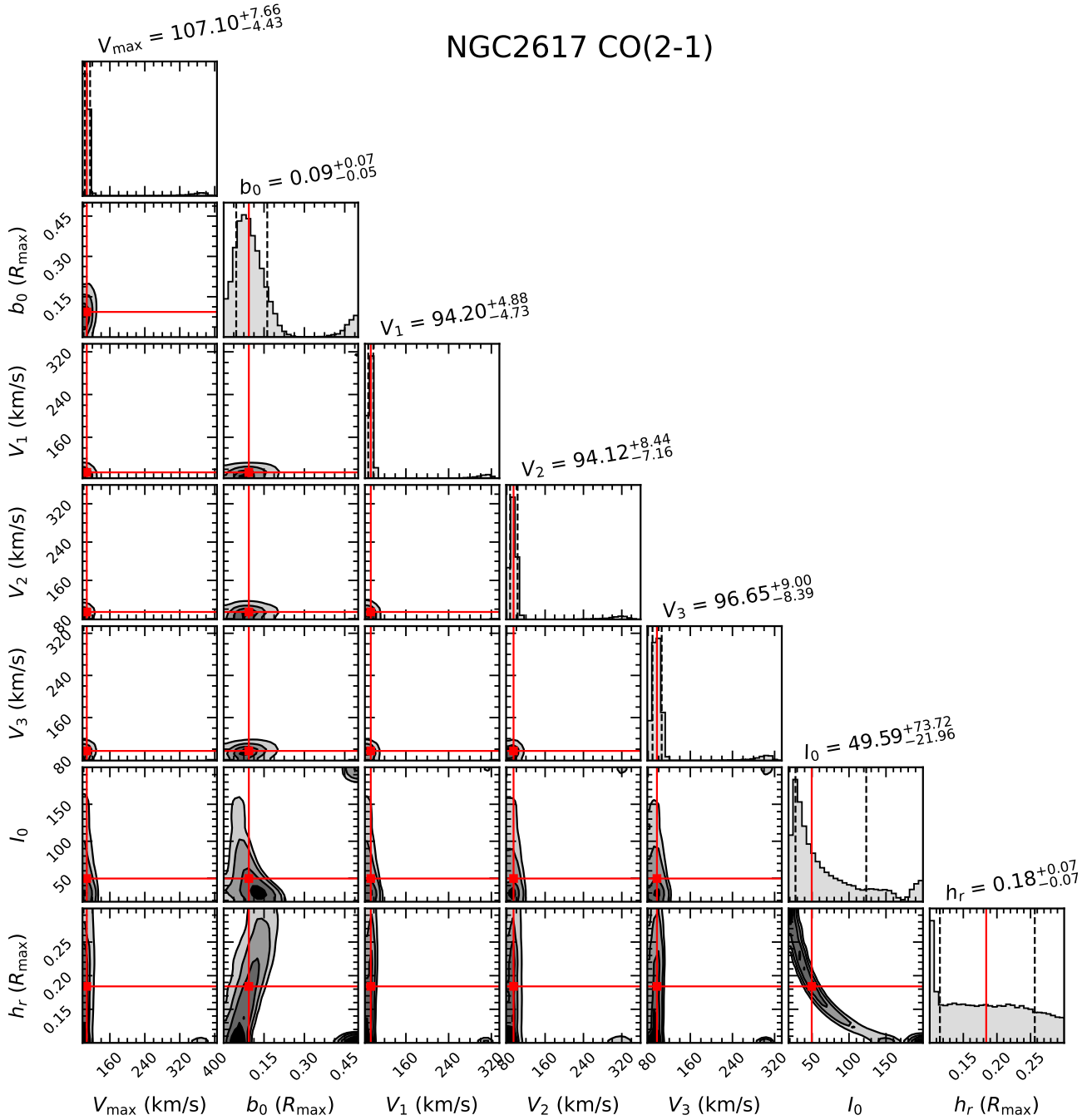

Fig. B.8: Same as Fig. B.4, but for NGC 2617 CO(2-1).

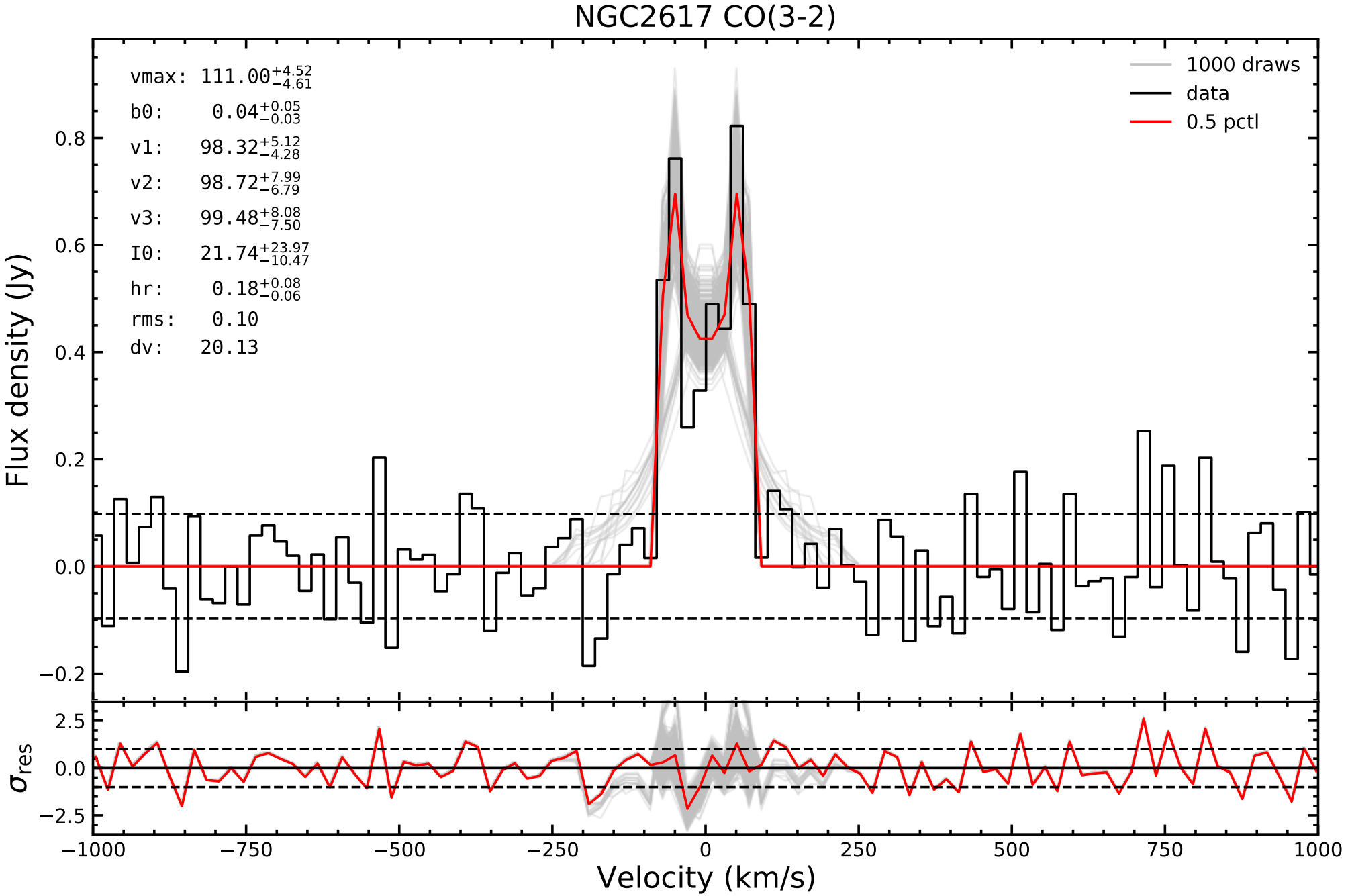

Fig. B.9: Same as Fig. B.1, but for NGC 2617 CO(3-2).

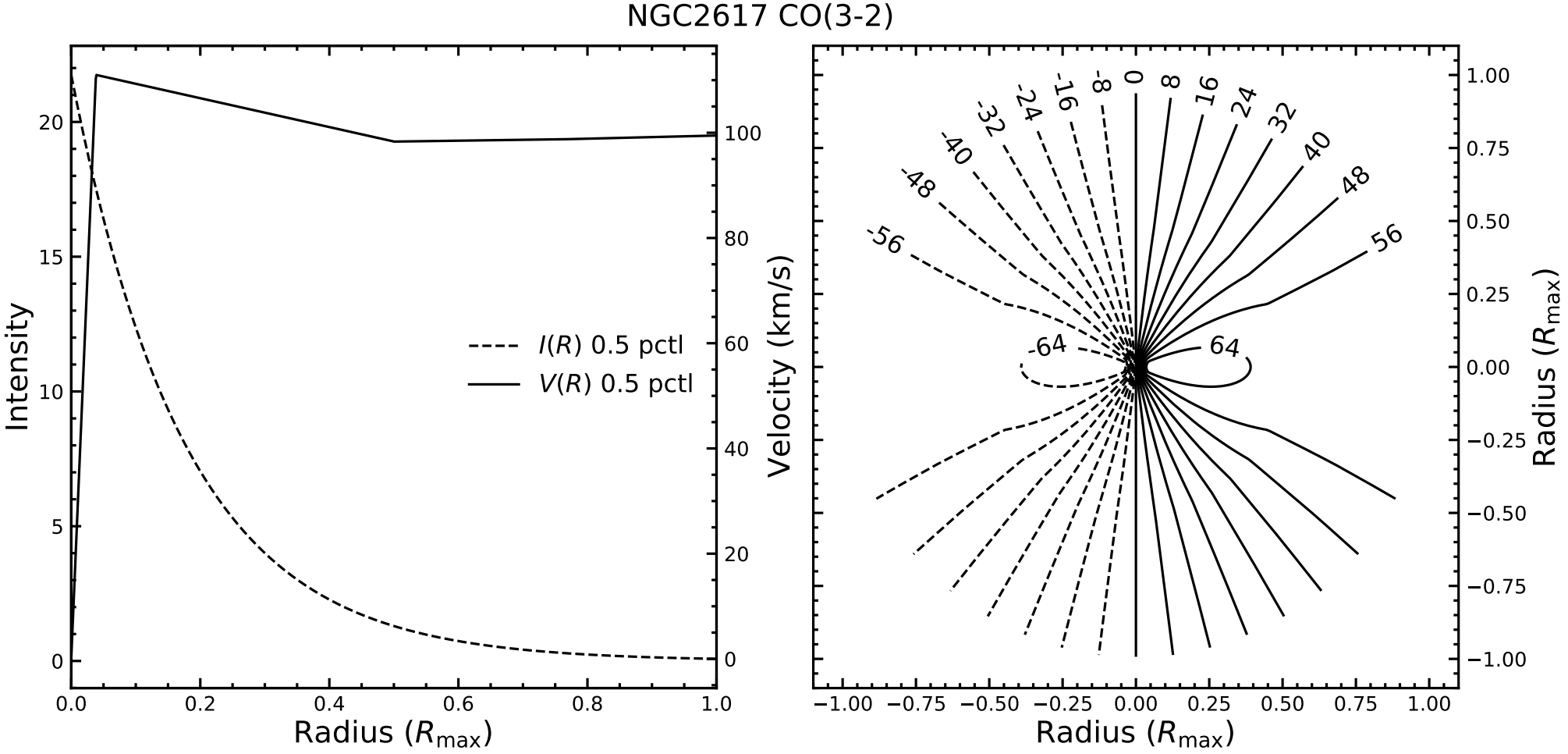

Fig. B.10: Same as Fig. B.2, but for NGC 2617 CO(3-2).

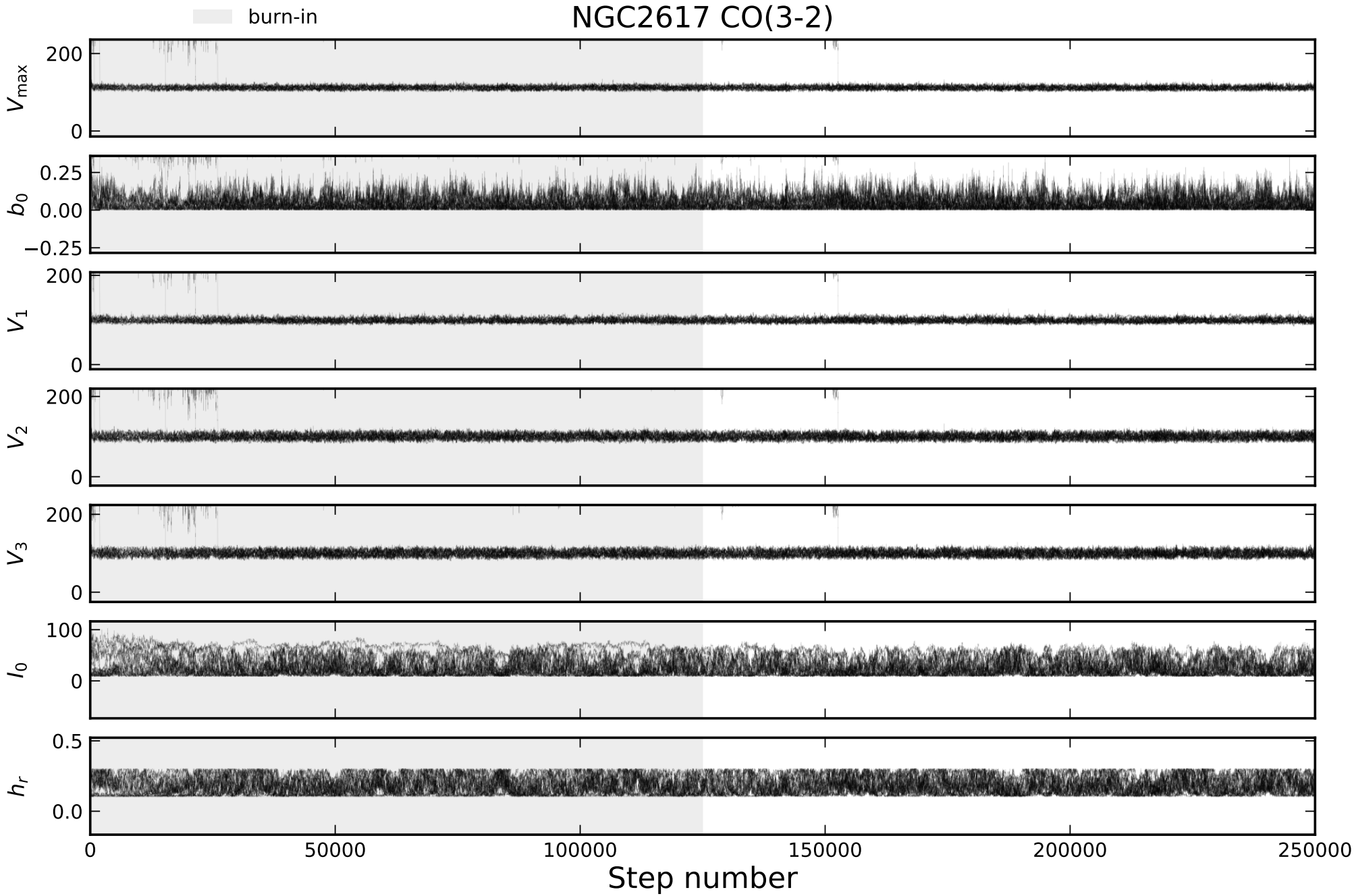

Fig. B.11: Same as Fig. B.3, but for NGC 2617 CO(3-2).

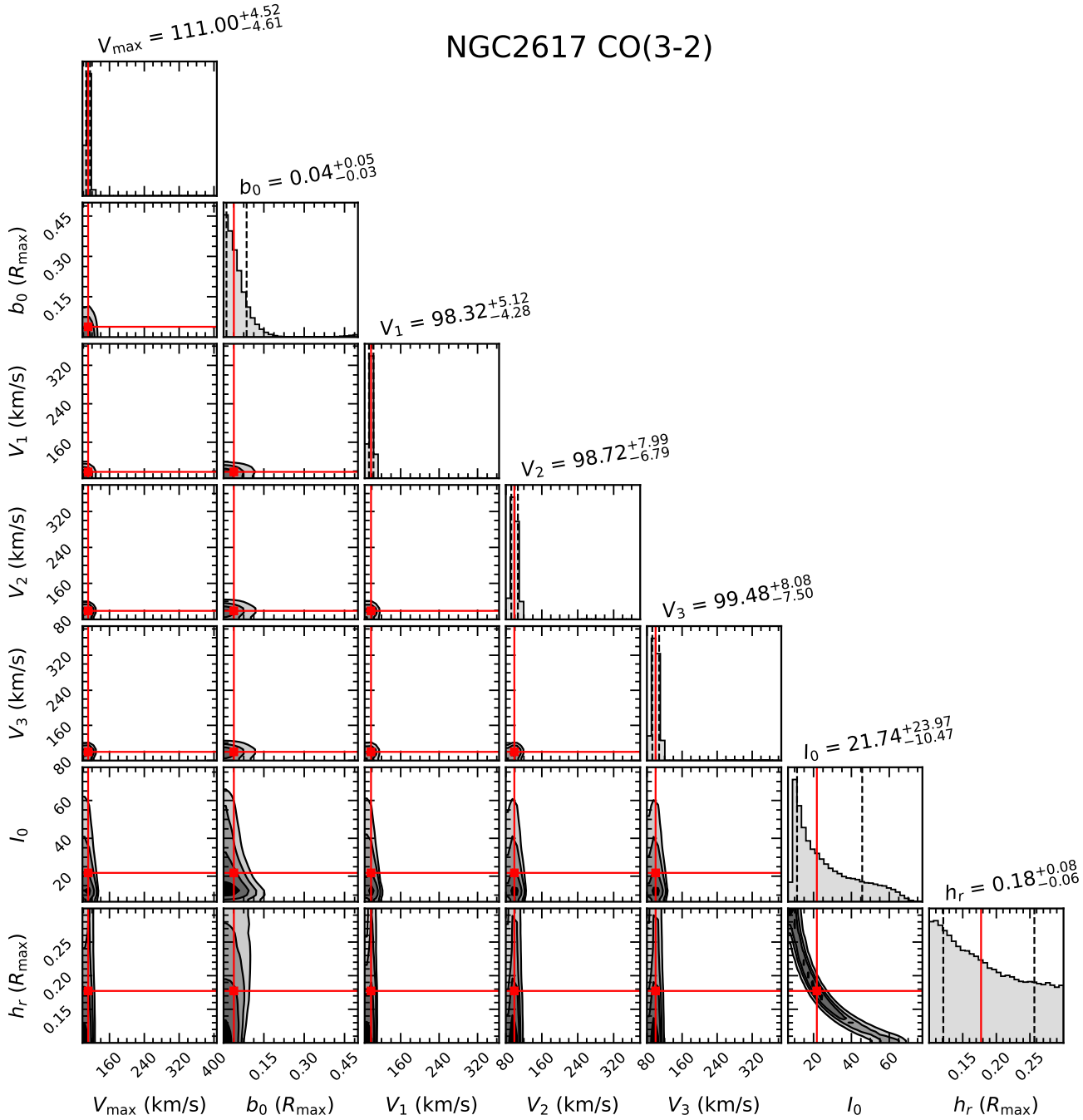

Fig. B.12: Same as Fig. B.4, but for NGC 2617 CO(3-2).

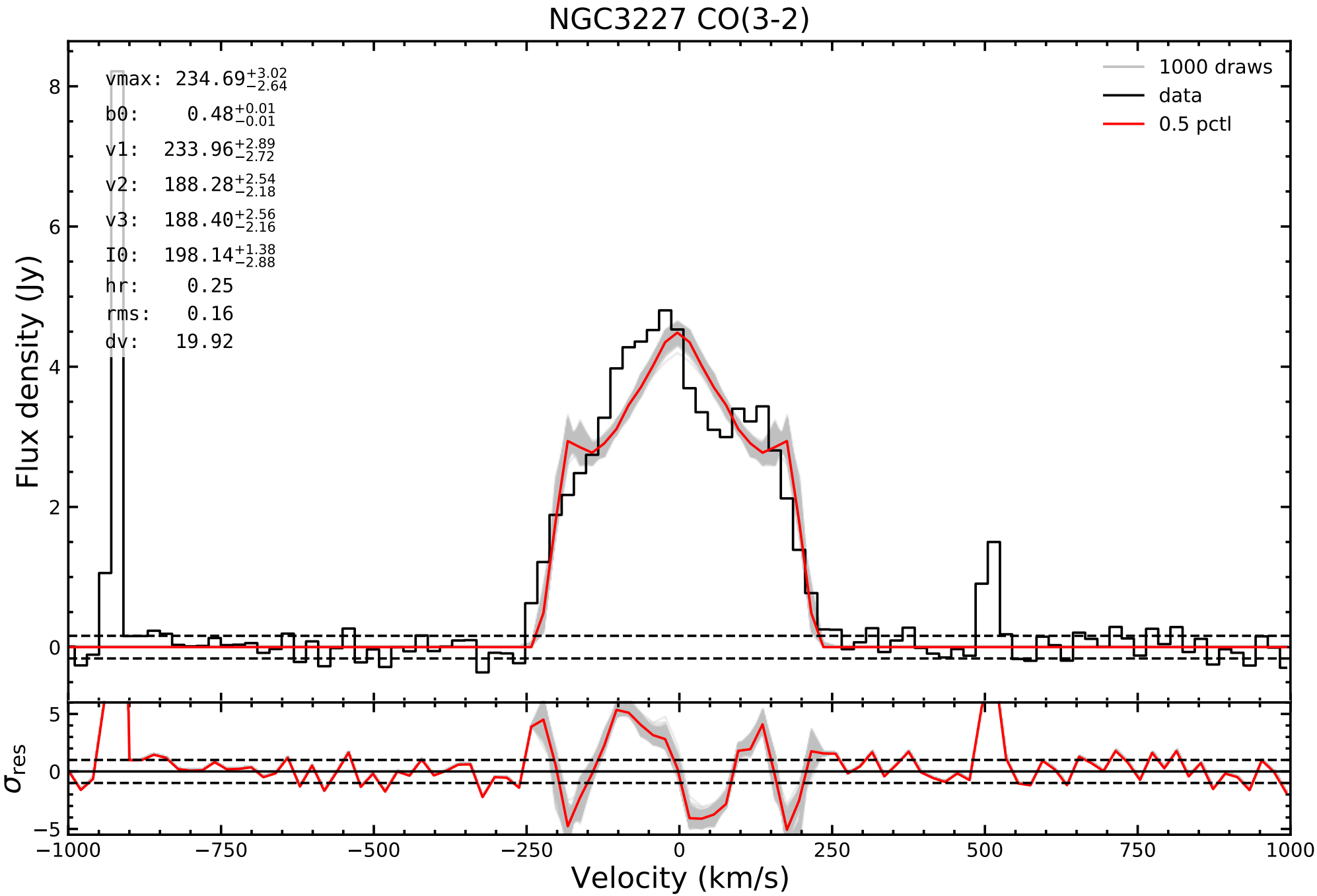

Fig. B.13: Same as Fig. B.1, but for NGC 3227 CO(3-2).

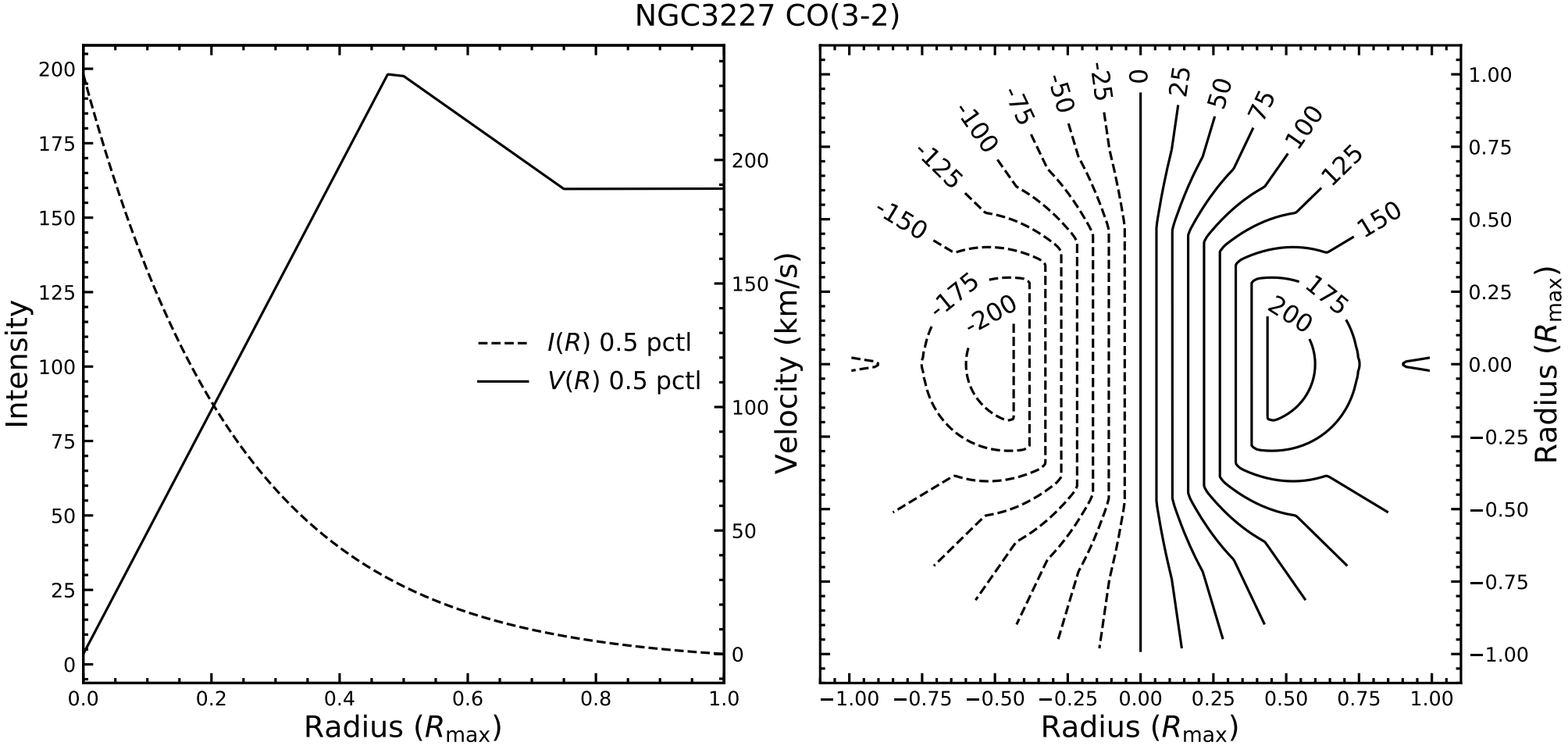

Fig. B.14: Same as Fig. B.2, but for NGC 3227 CO(3-2).

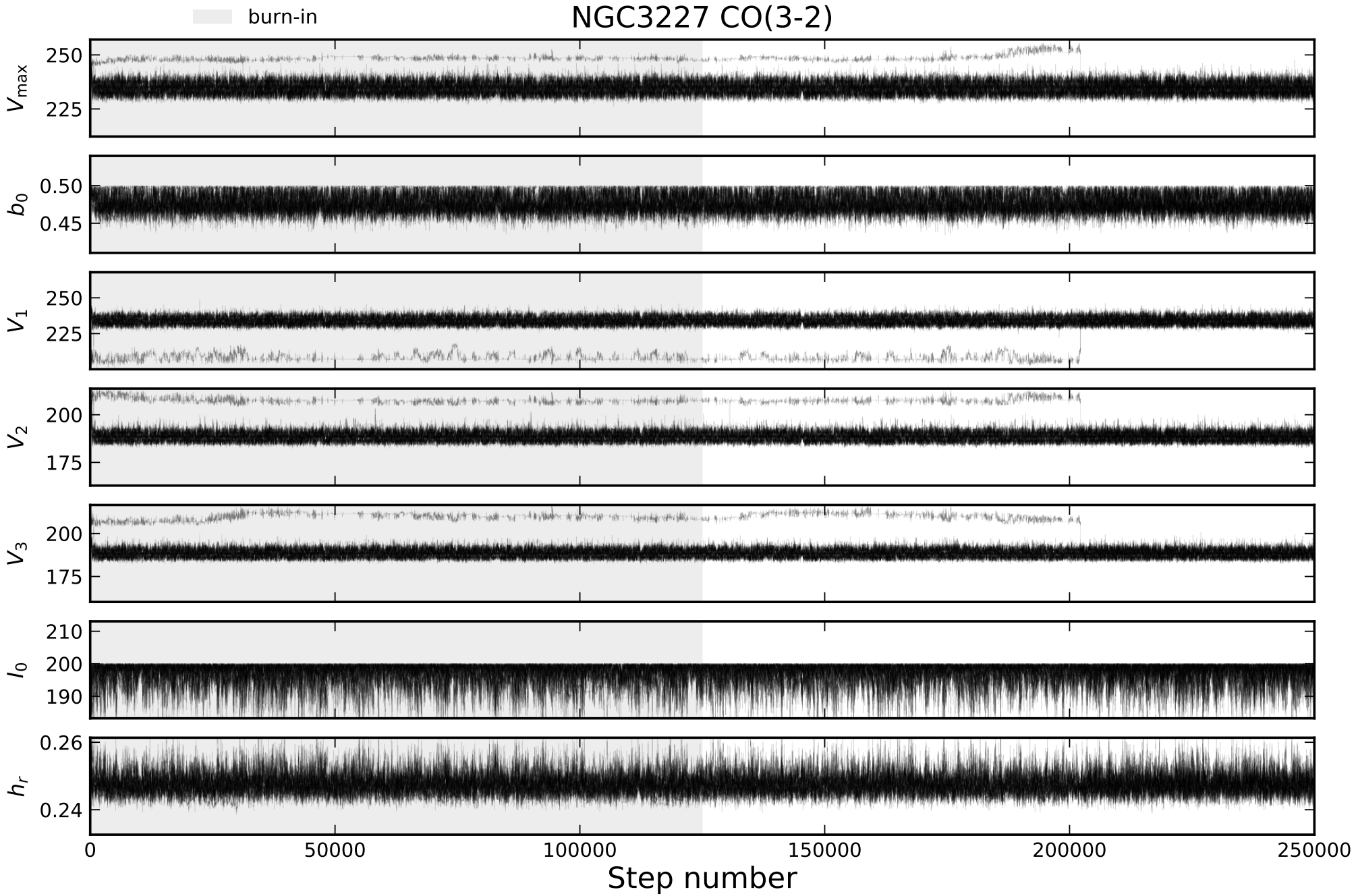

Fig. B.15: Same as Fig. B.3, but for NGC 3227 CO(3-2).

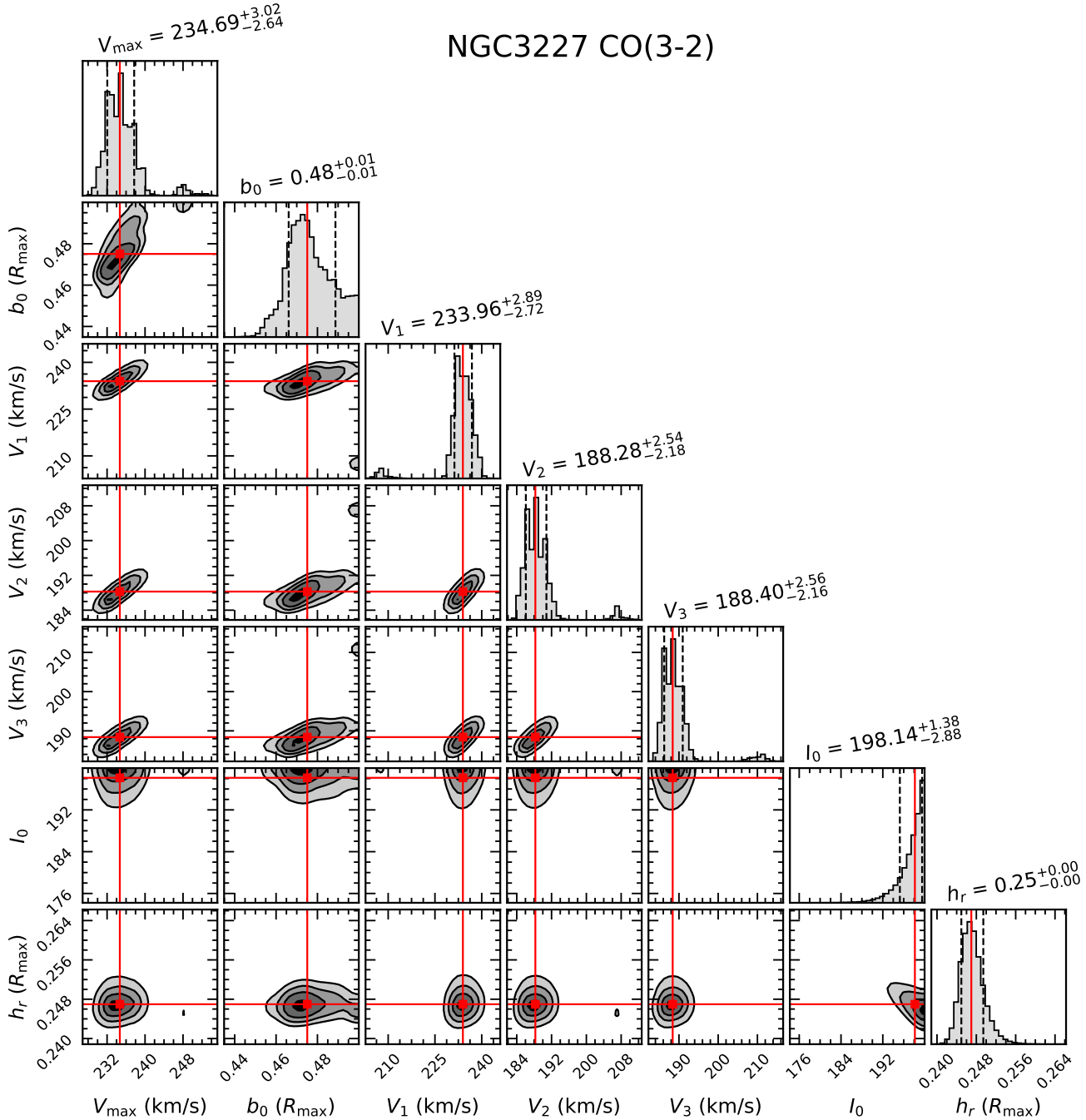

Fig. B.16: Same as Fig. B.4, but for NGC 3227 CO(3-2).

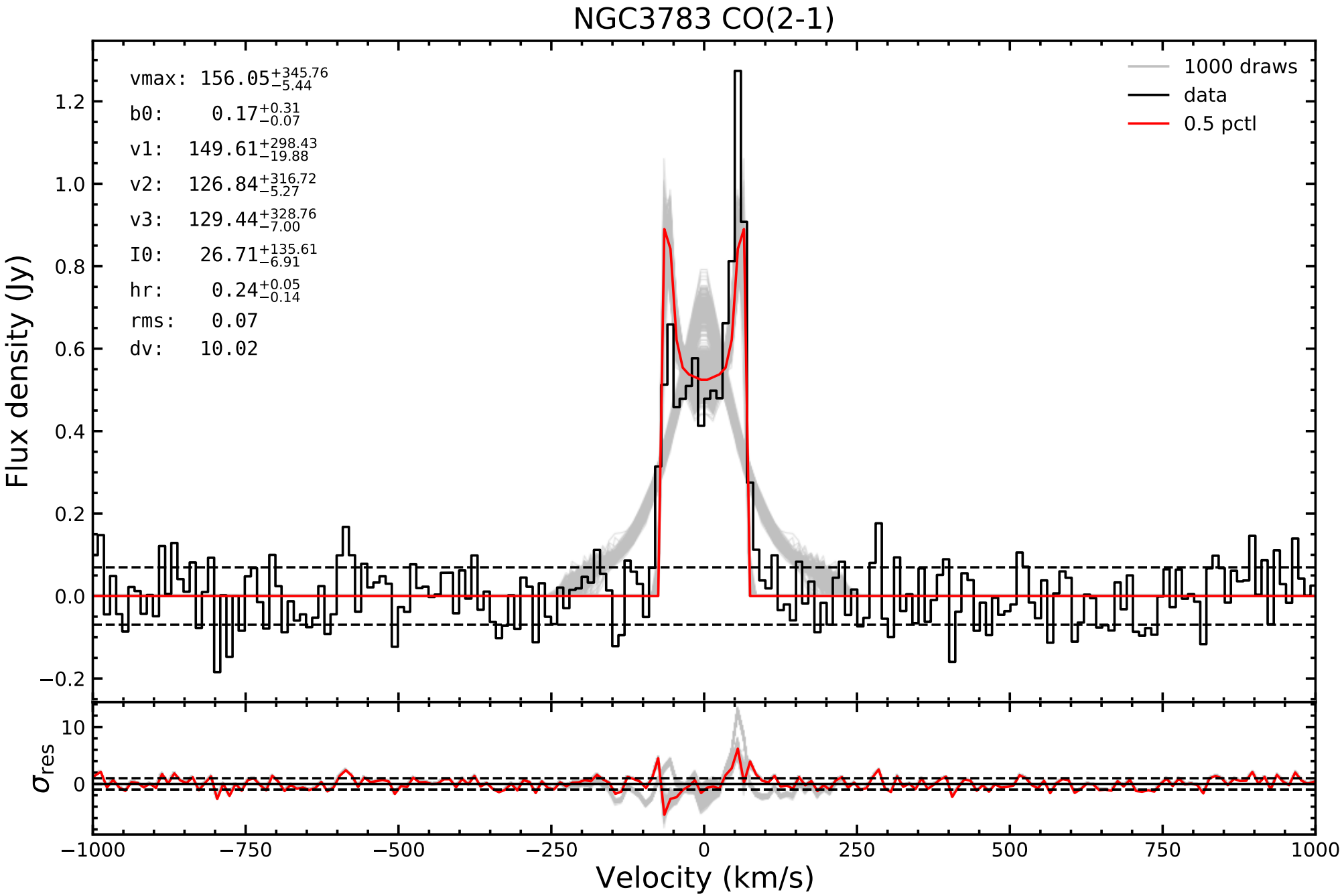

Fig. B.17: Same as Fig. B.1, but for NGC 3783 CO(2-1).

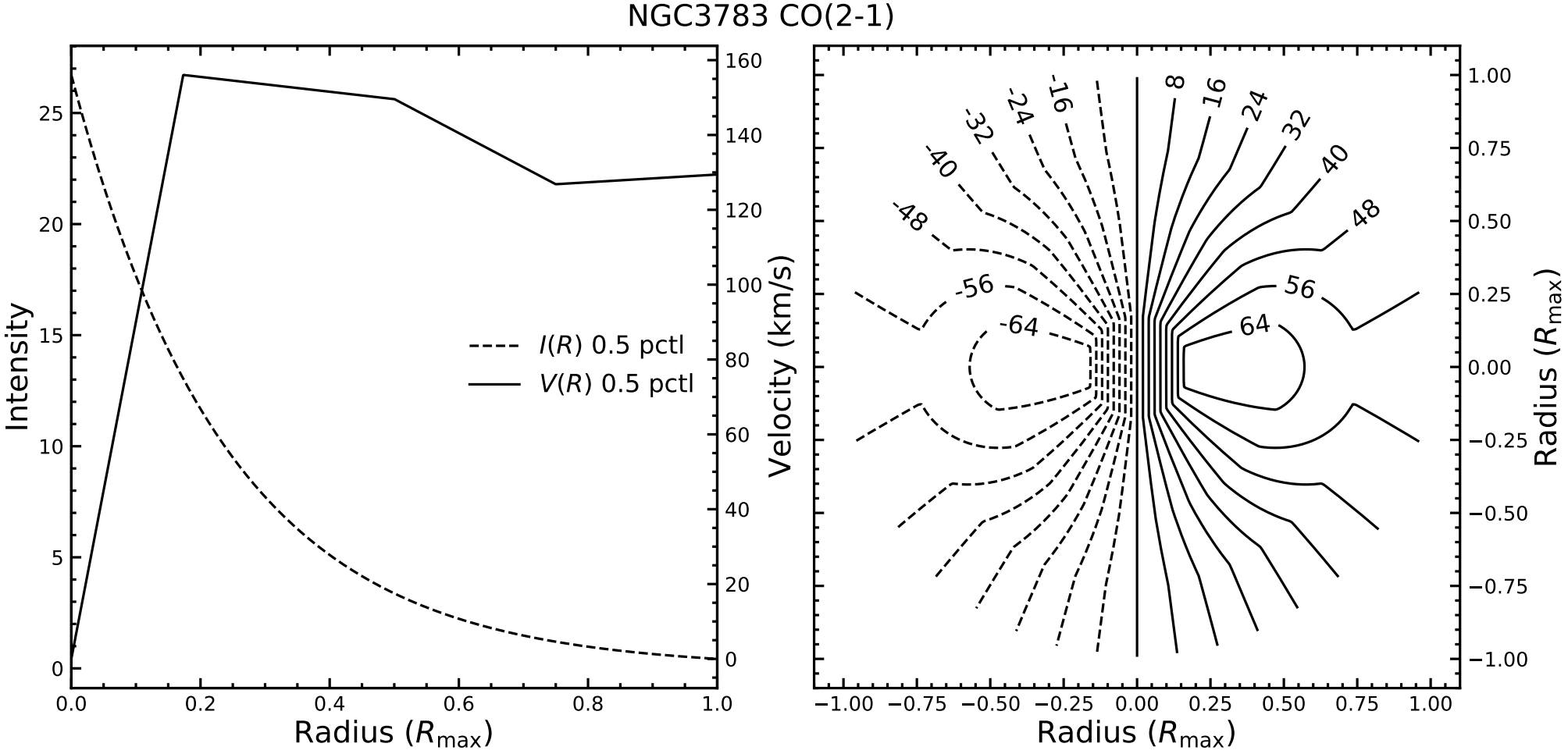

Fig. B.18: Same as Fig. B.2, but for NGC 3783 CO(2-1).

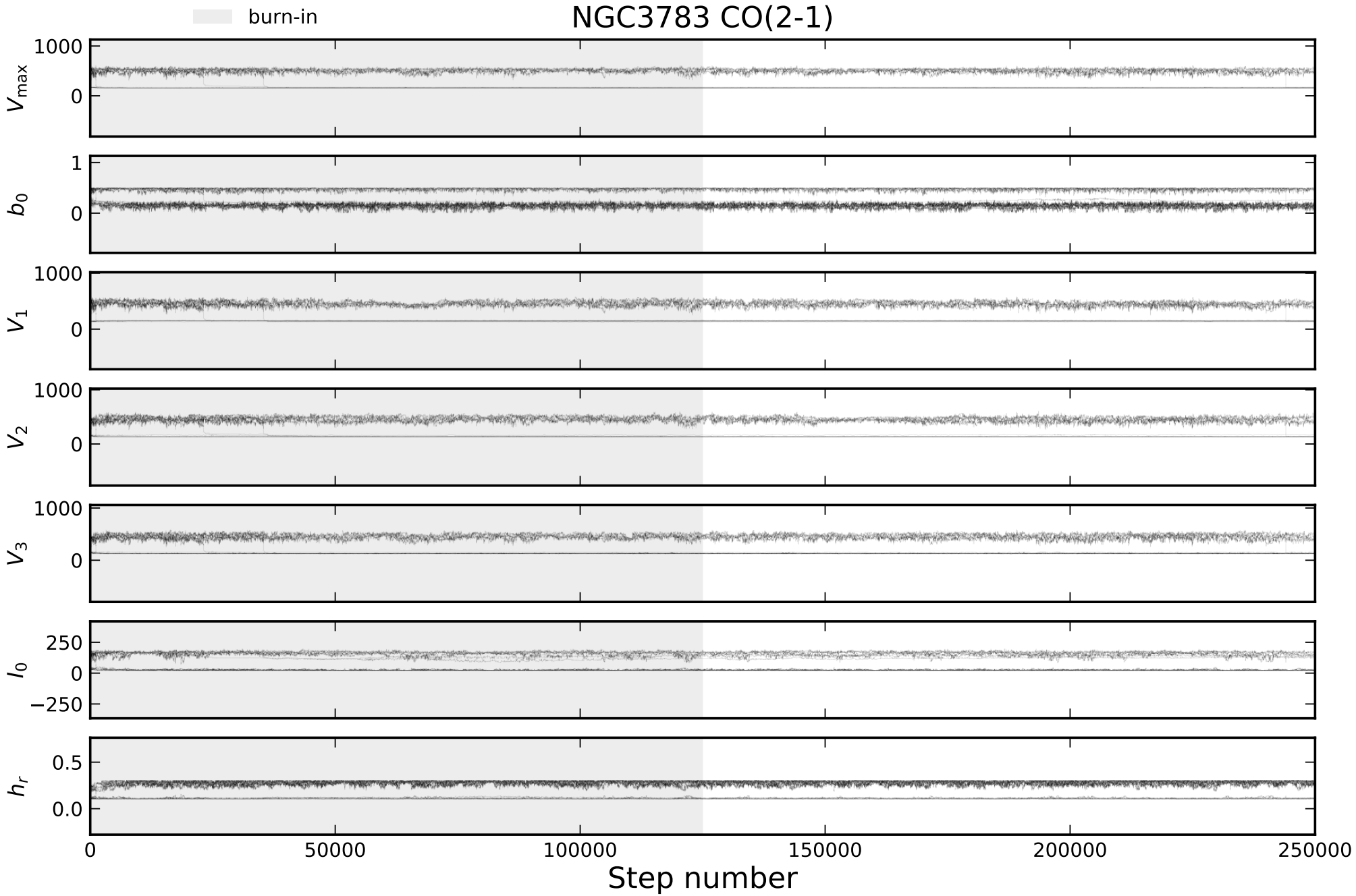

Fig. B.19: Same as Fig. B.3, but for NGC 3783 CO(2-1).

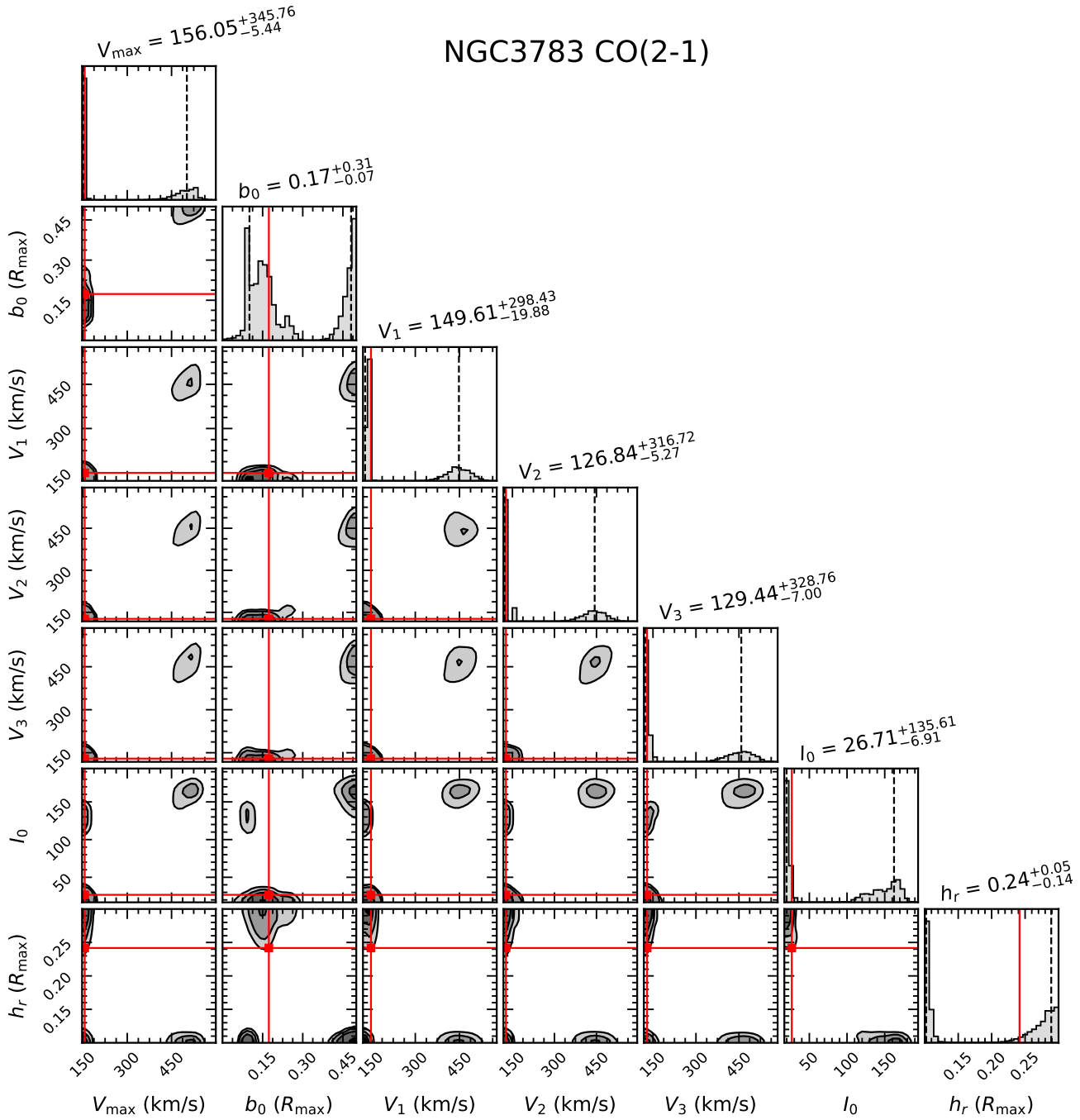

Fig. B.20: Same as Fig. B.4, but for NGC 3783 CO(2-1).

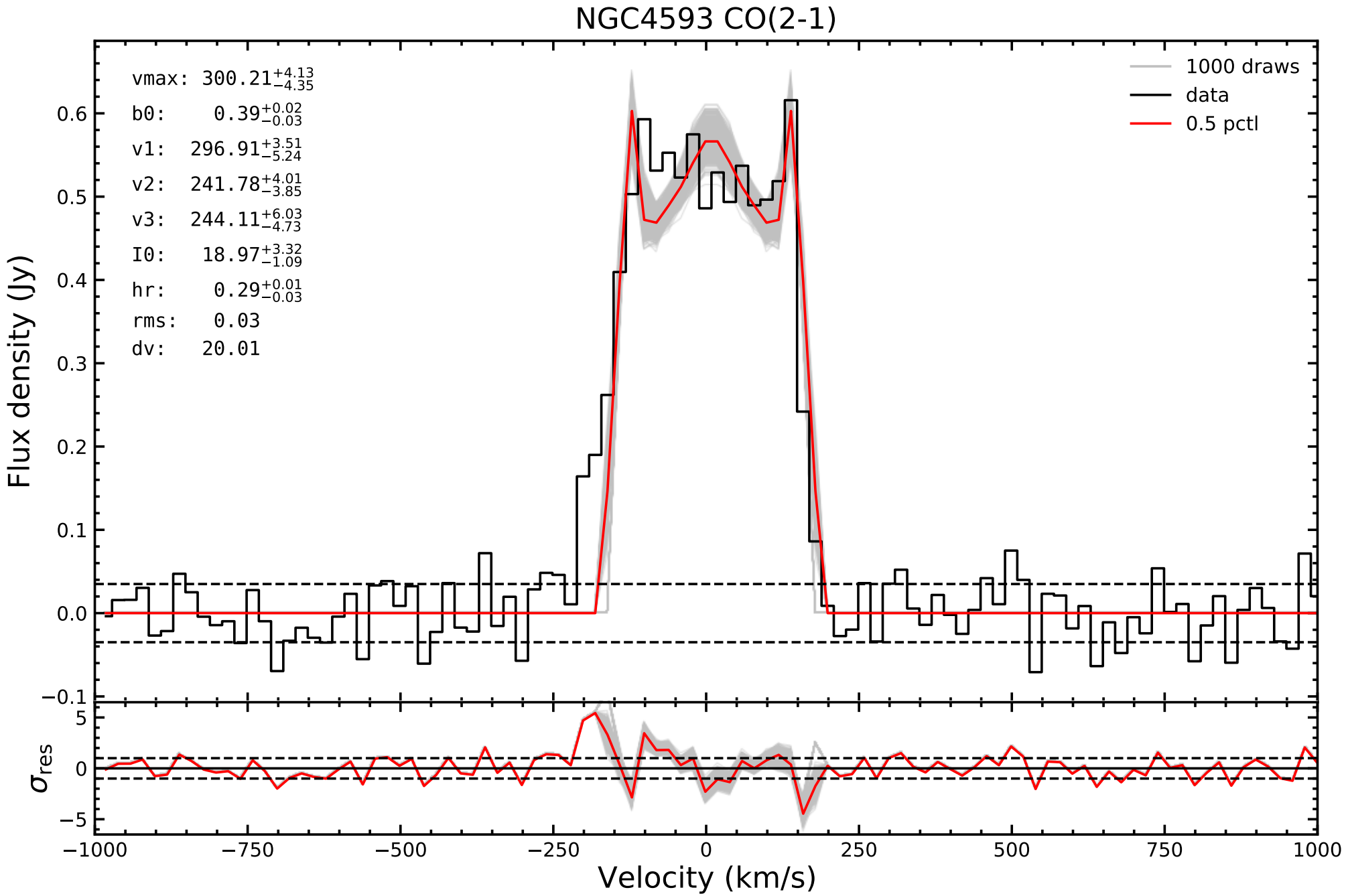

Fig. B.21: Same as Fig. B.1, but for NGC 4593 CO(2-1).

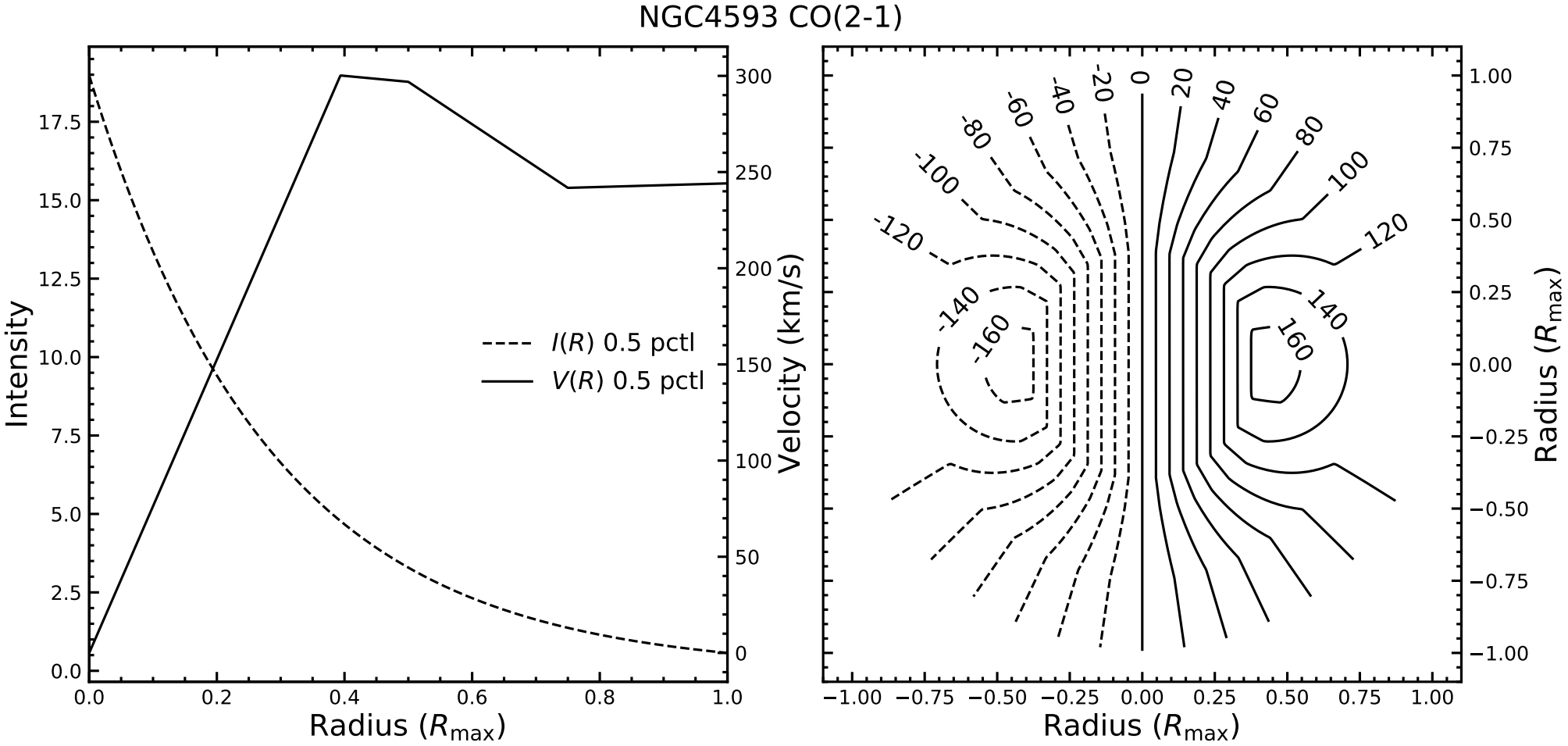

Fig. B.22: Same as Fig. B.2, but for NGC 4593 CO(2-1).

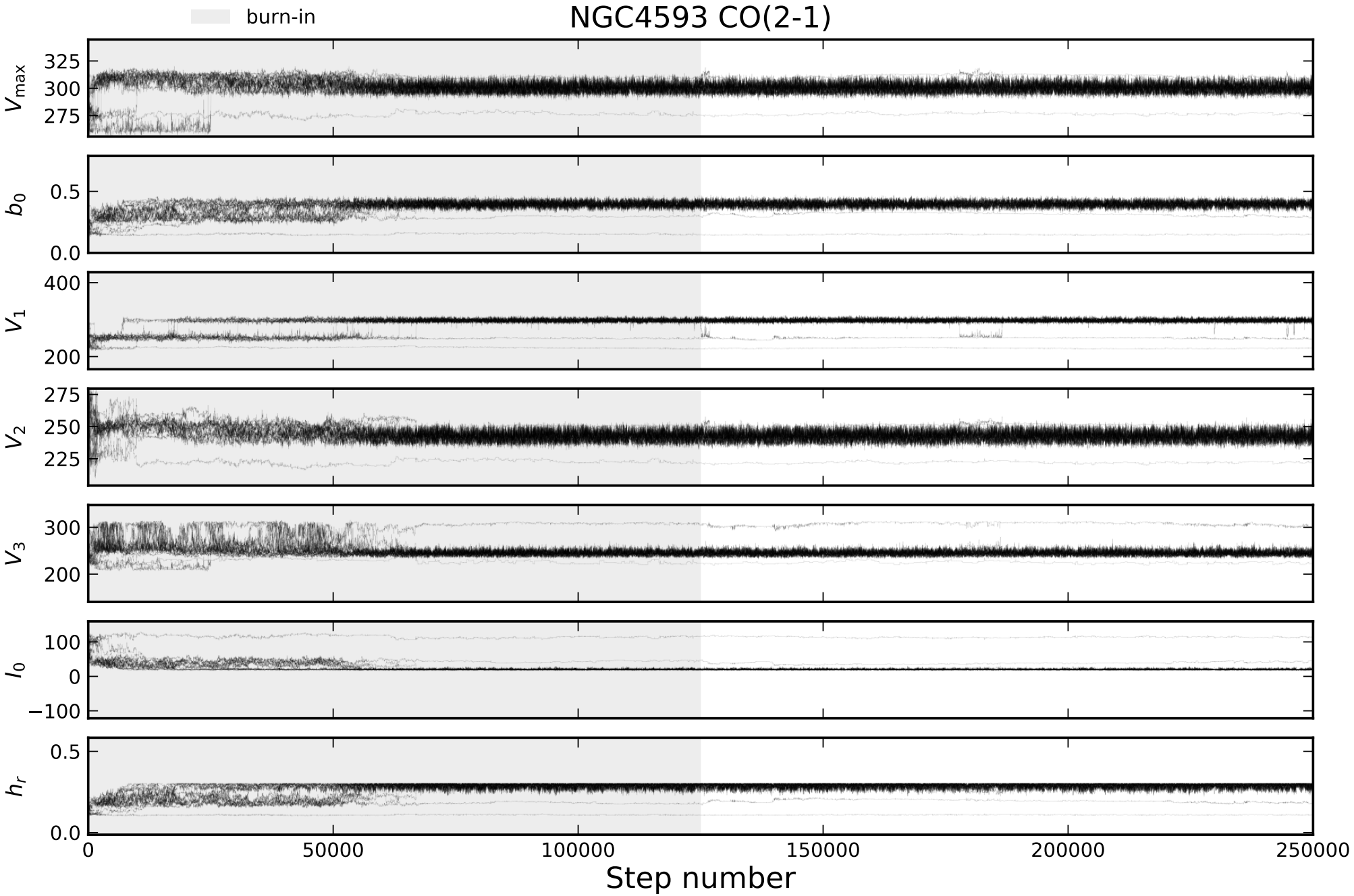

Fig. B.23: Same as Fig. B.3, but for NGC 4593 CO(2-1).

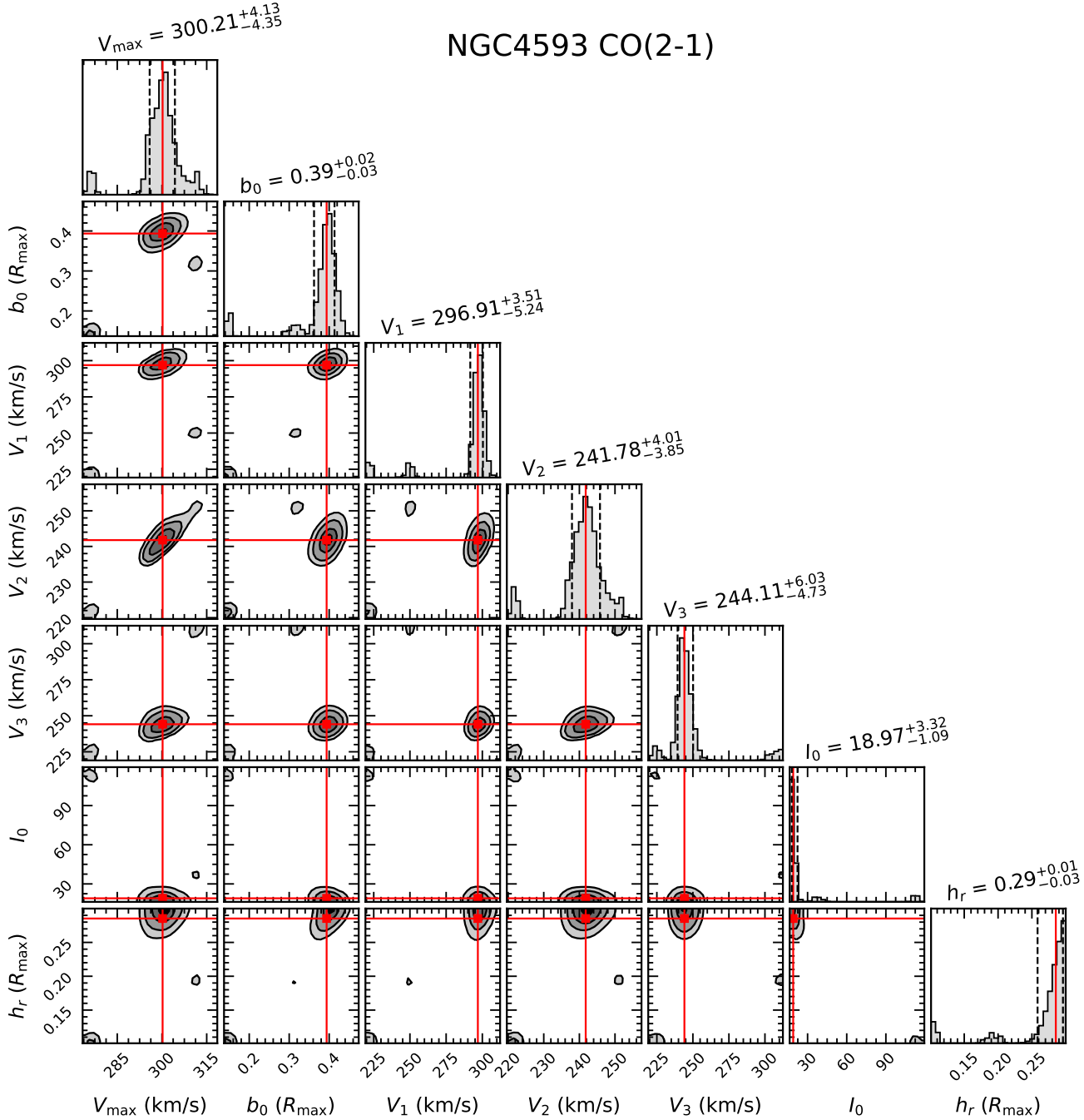

Fig. B.24: Same as Fig. B.4, but for NGC 4593 CO(2-1).

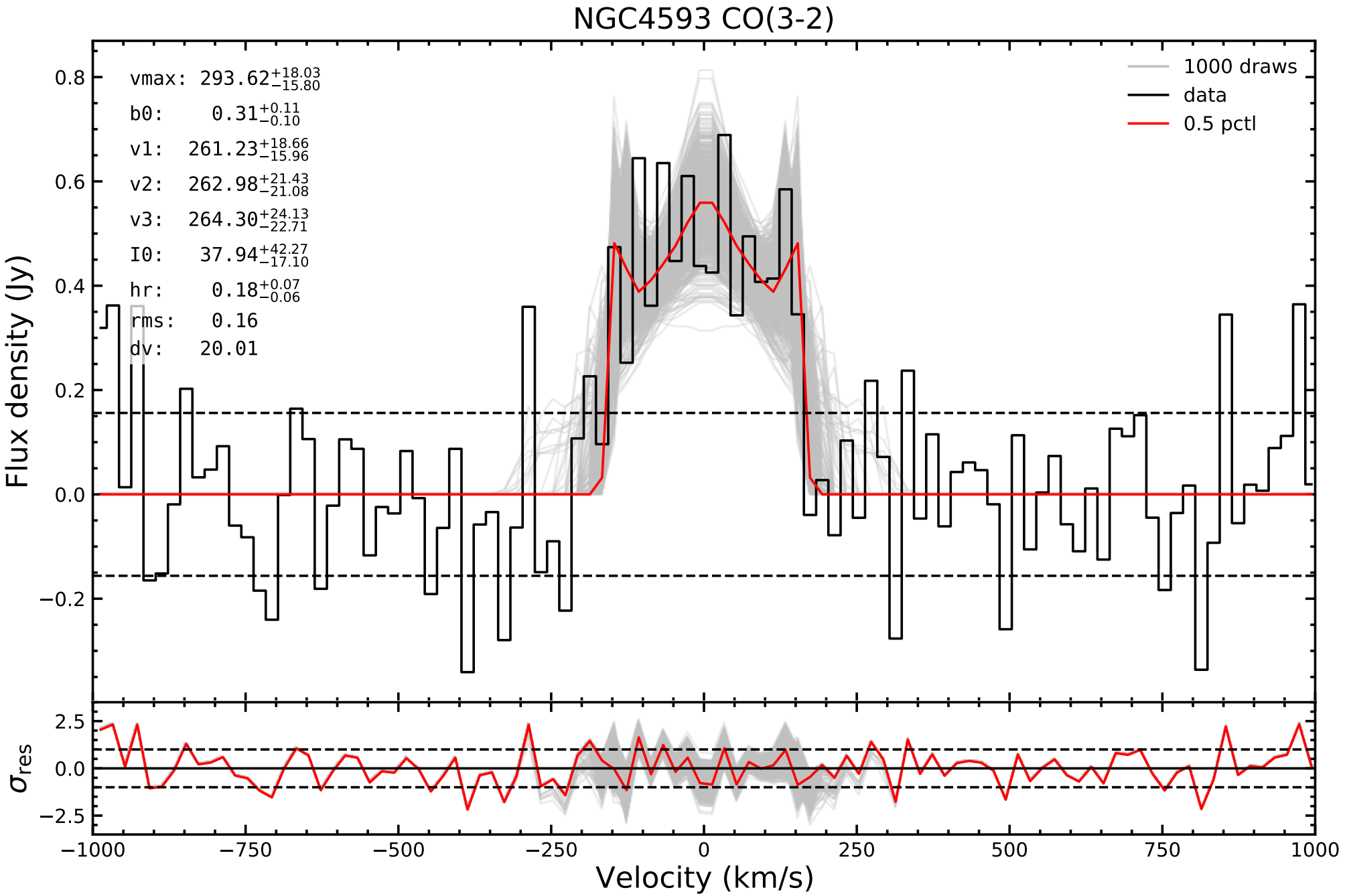

Fig. B.25: Same as Fig. B.1, but for NGC 4593 CO(3-2).

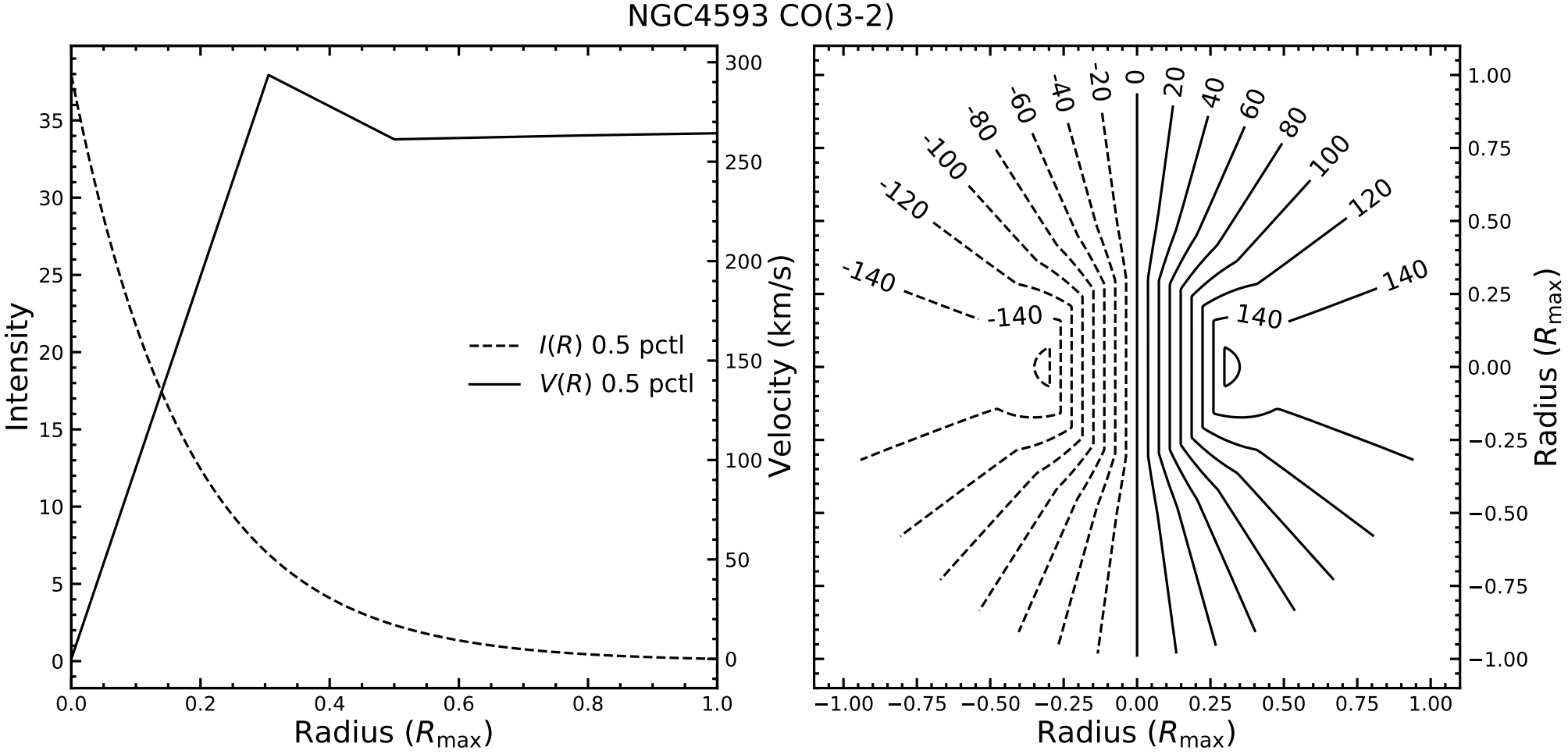

Fig. B.26: Same as Fig. B.2, but for NGC 4593 CO(3-2).

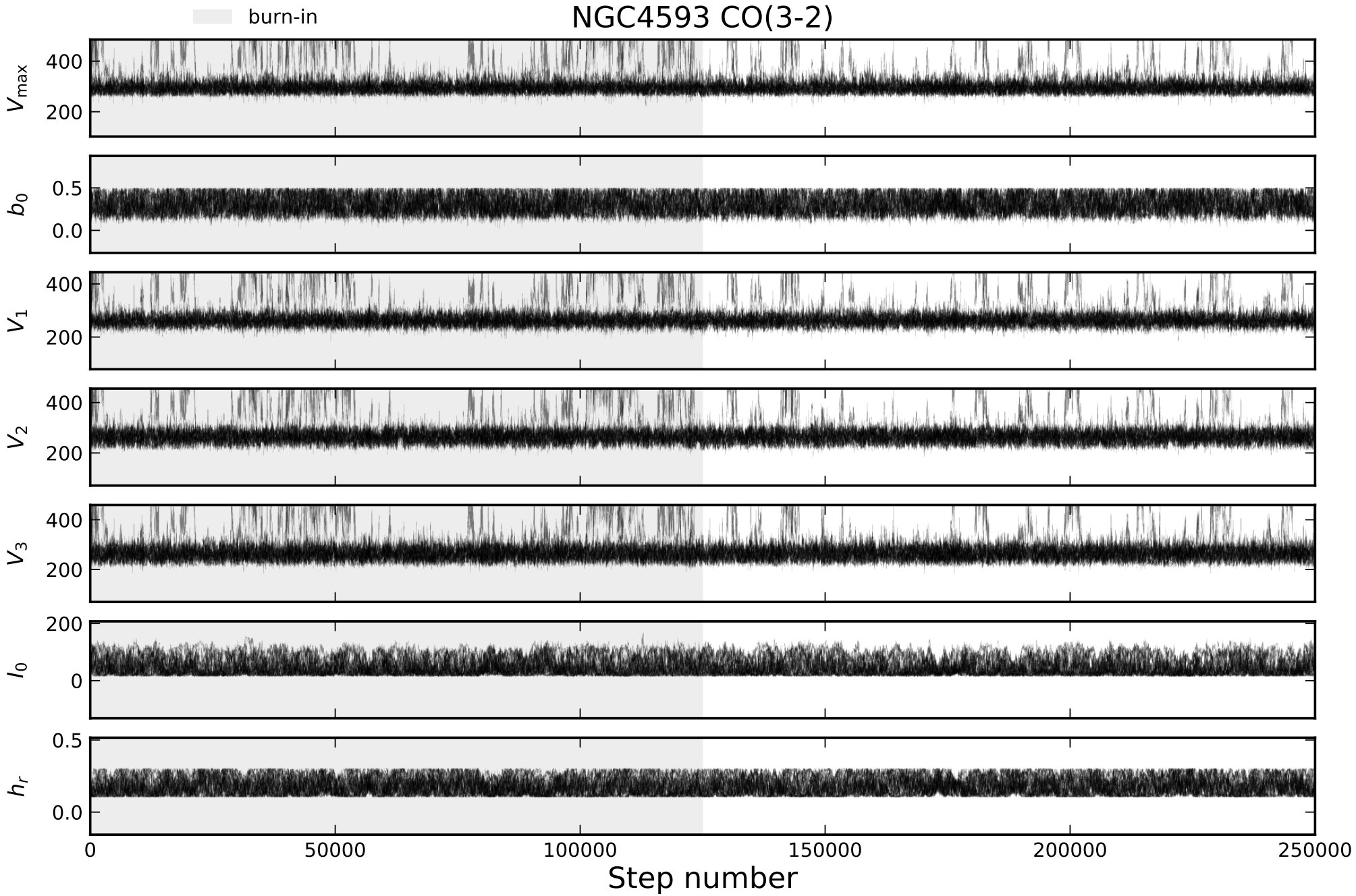

Fig. B.27: Same as Fig. B.3, but for NGC 4593 CO(3-2).

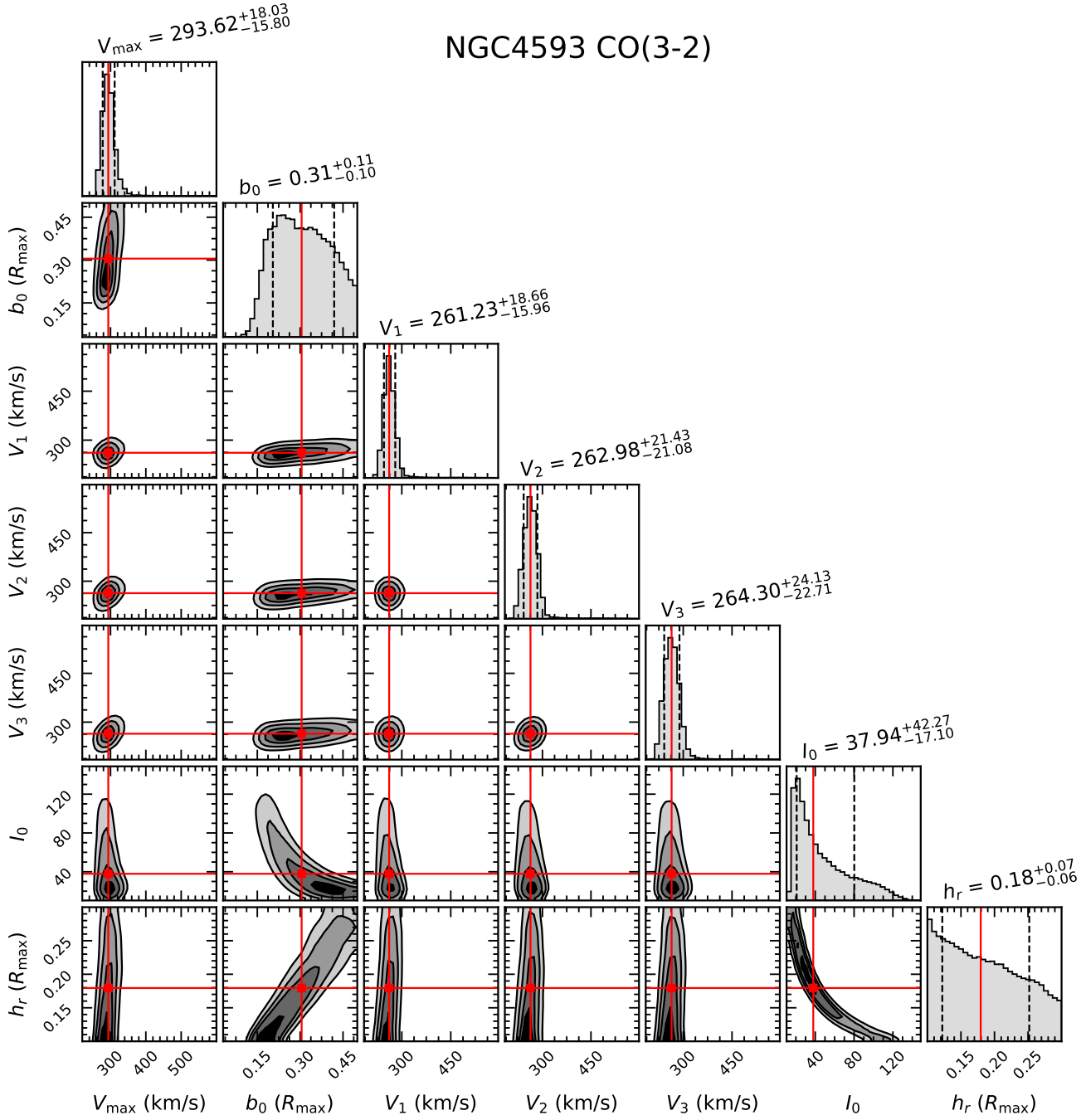

Fig. B.28: Same as Fig. B.4, but for NGC 4593 CO(3-2).

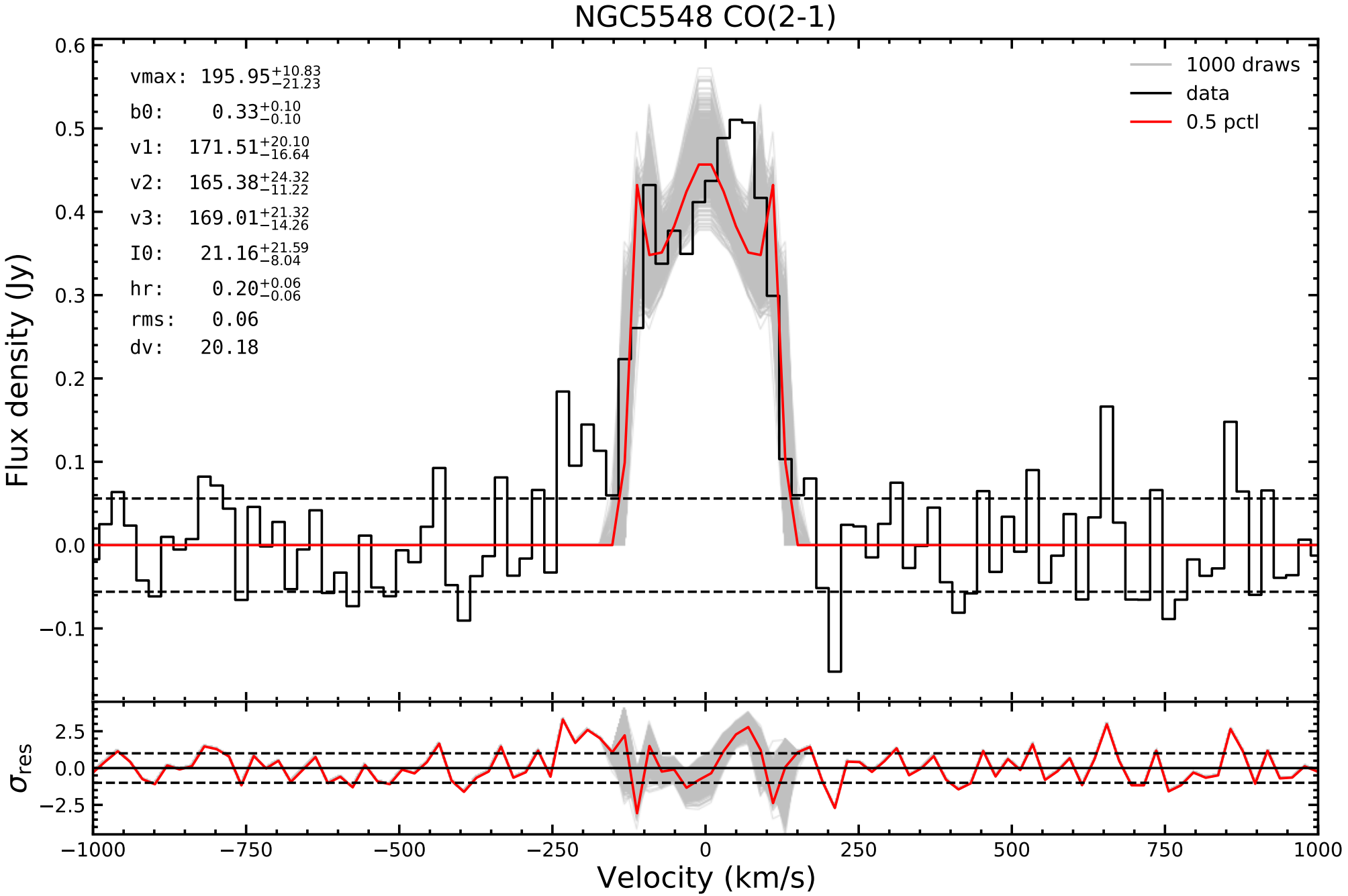

Fig. B.29: Same as Fig. B.1, but for NGC 5548 CO(2-1).

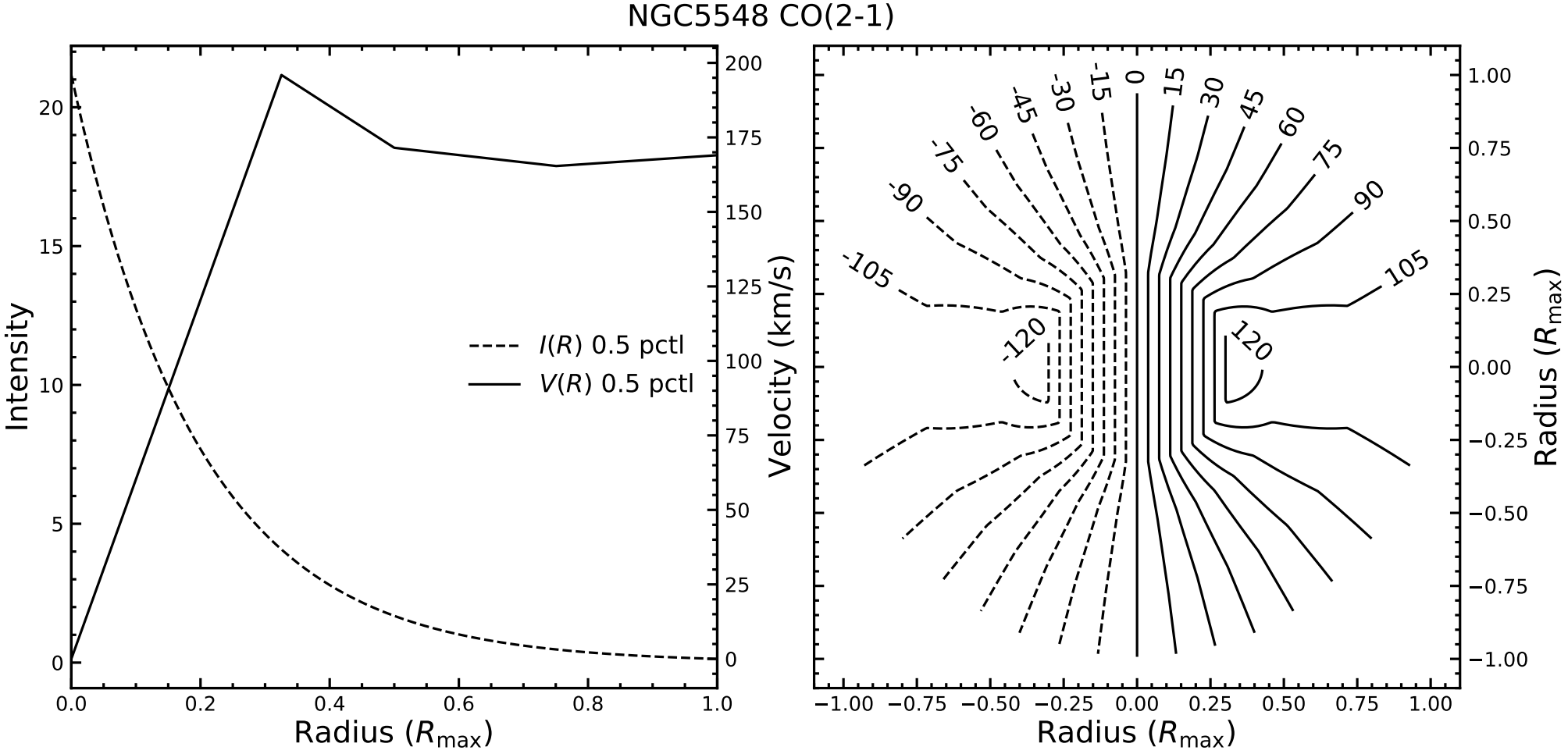

Fig. B.30: Same as Fig. B.2, but for NGC 5548 CO(2-1).

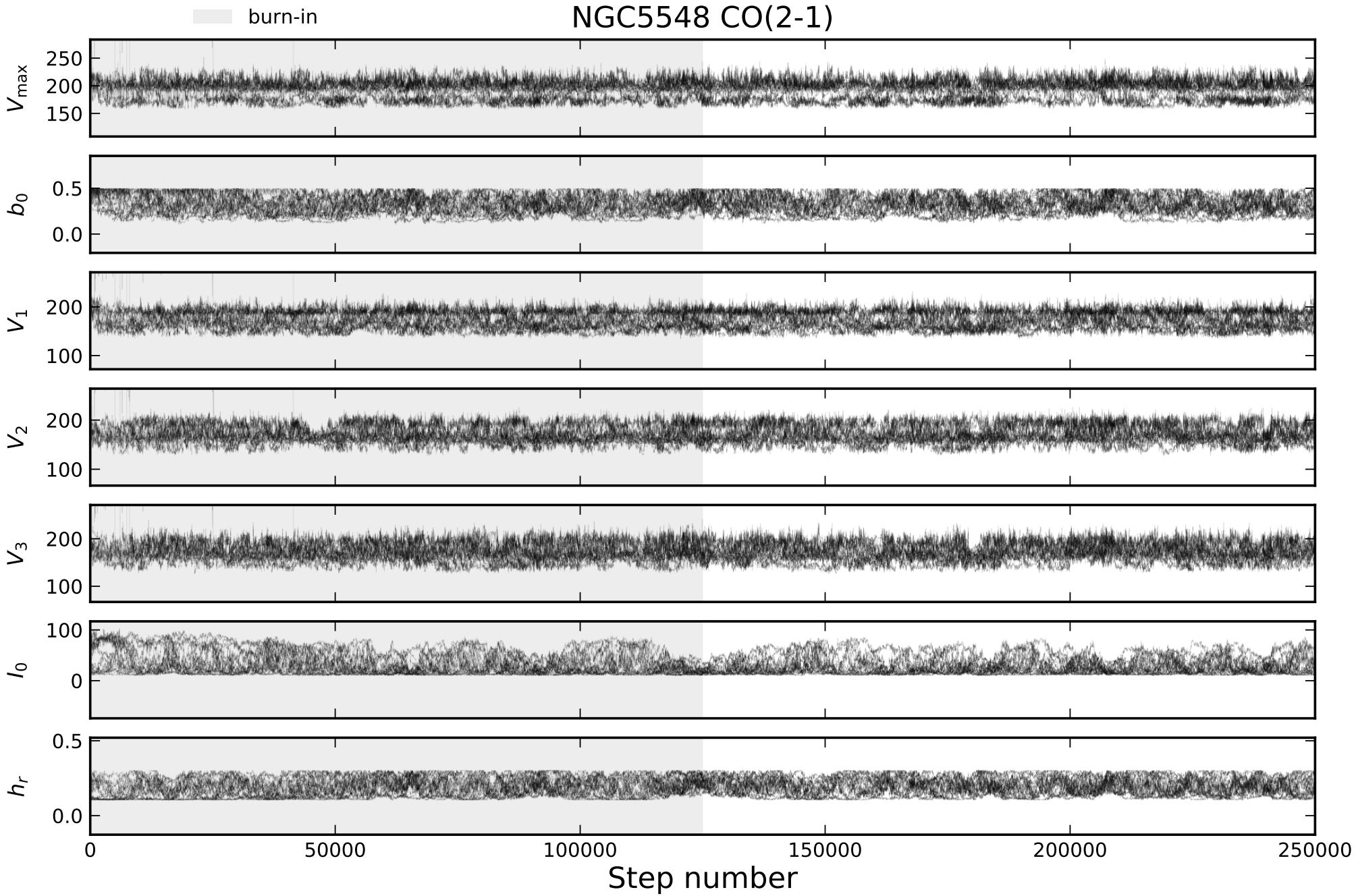

Fig. B.31: Same as Fig. B.3, but for NGC 5548 CO(2-1).

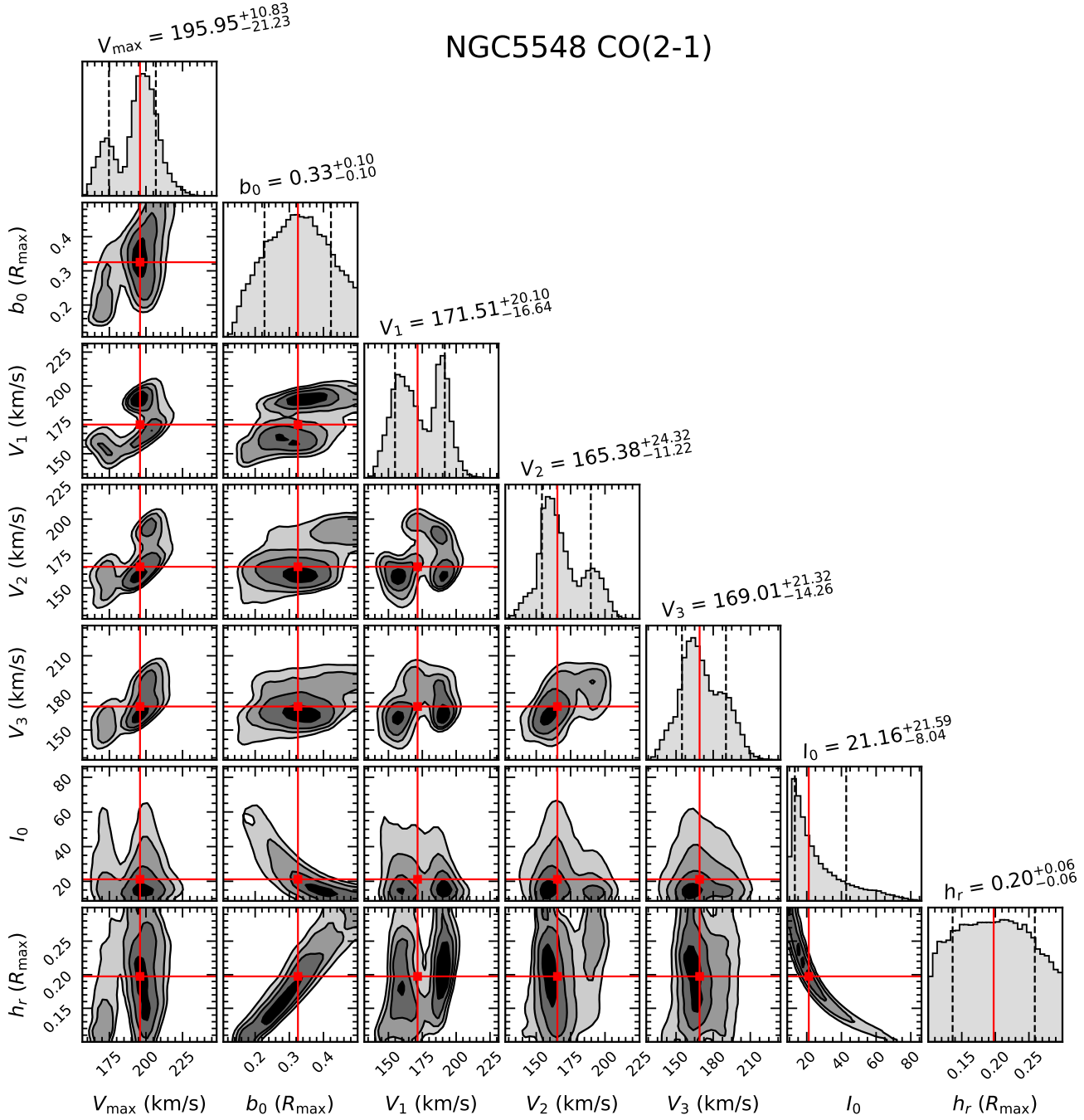

Fig. B.32: Same as Fig. B.4, but for NGC 5548 CO(2-1).

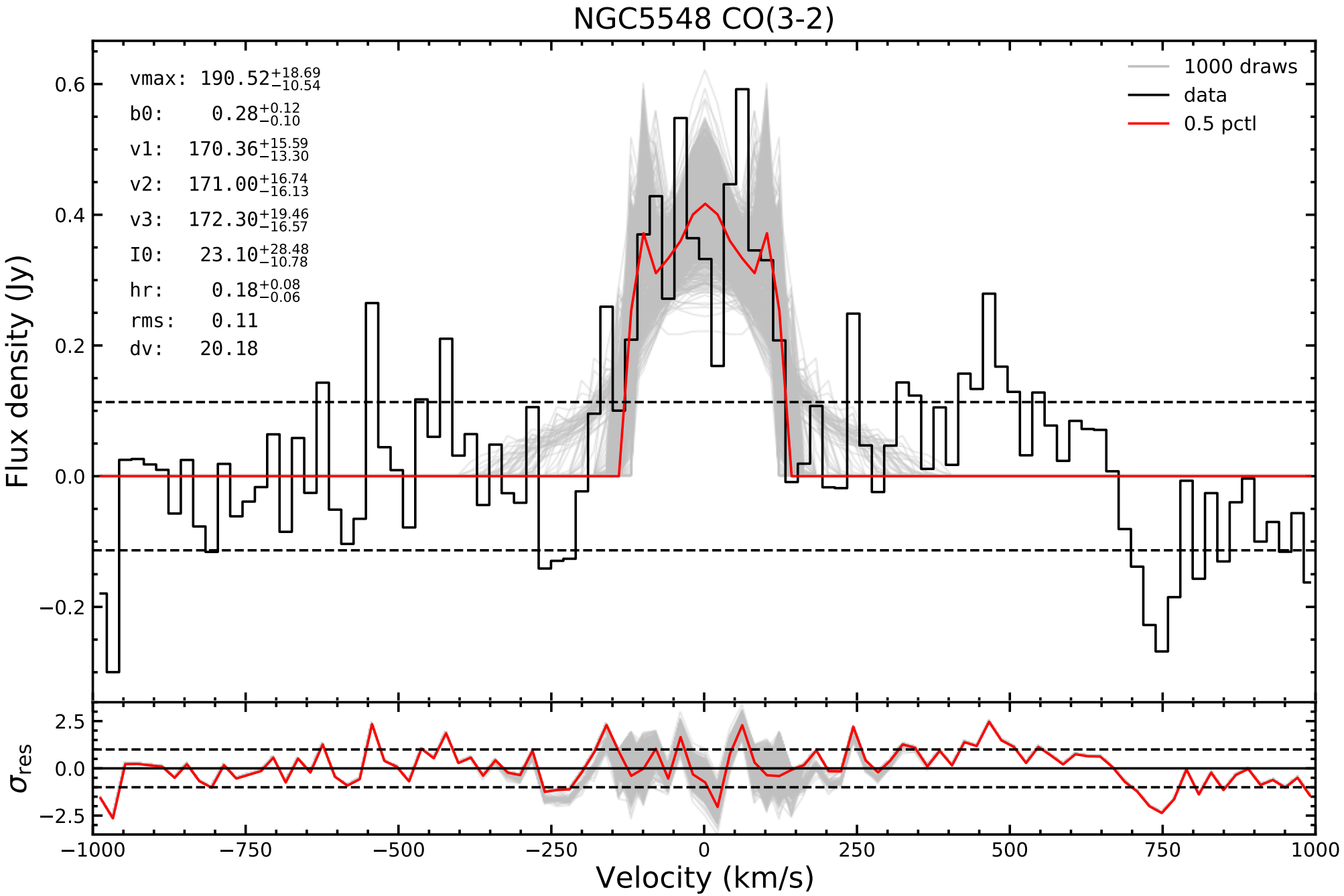

Fig. B.33: Same as Fig. B.1, but for NGC 5548 CO(3-2).

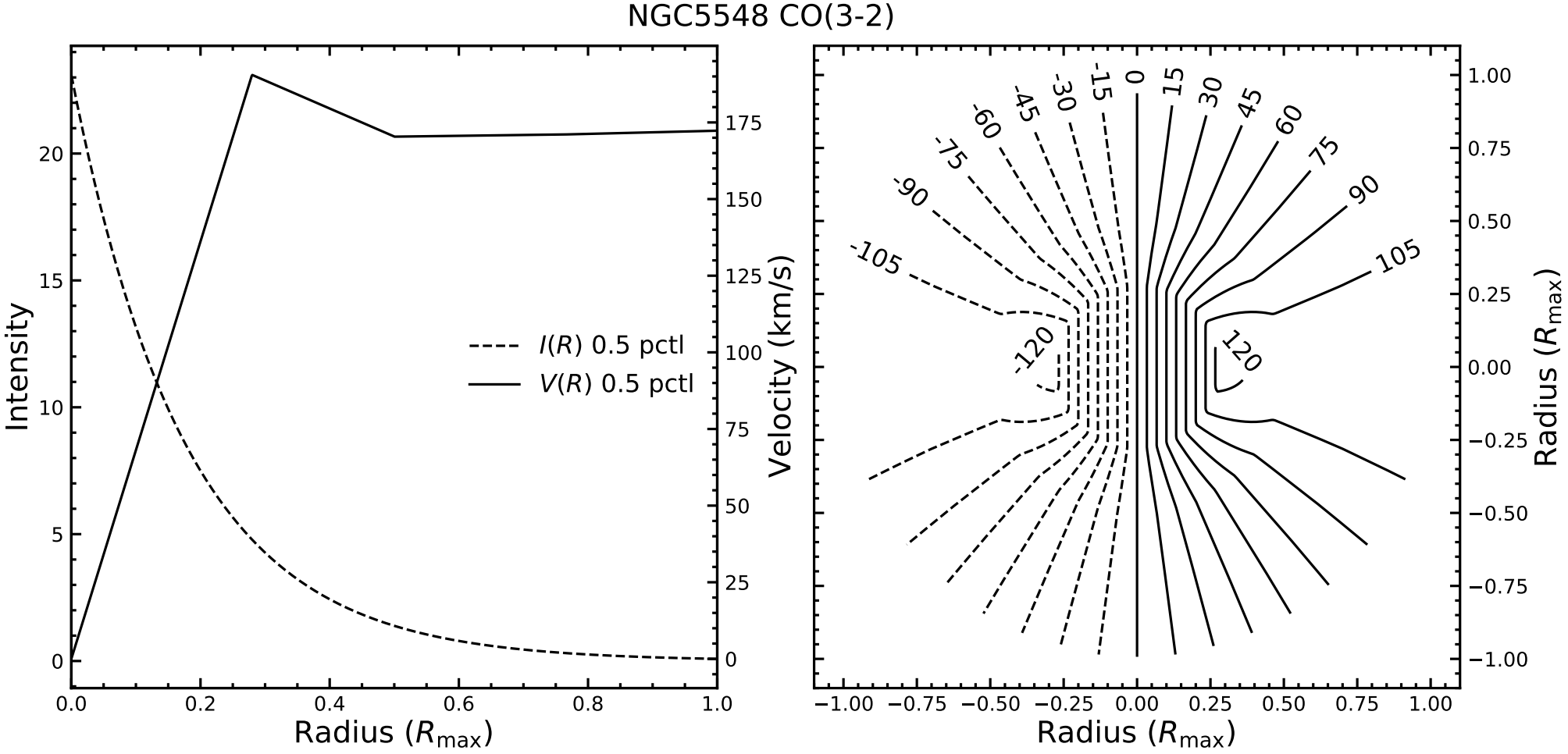

Fig. B.34: Same as Fig. B.2, but for NGC 5548 CO(3-2).

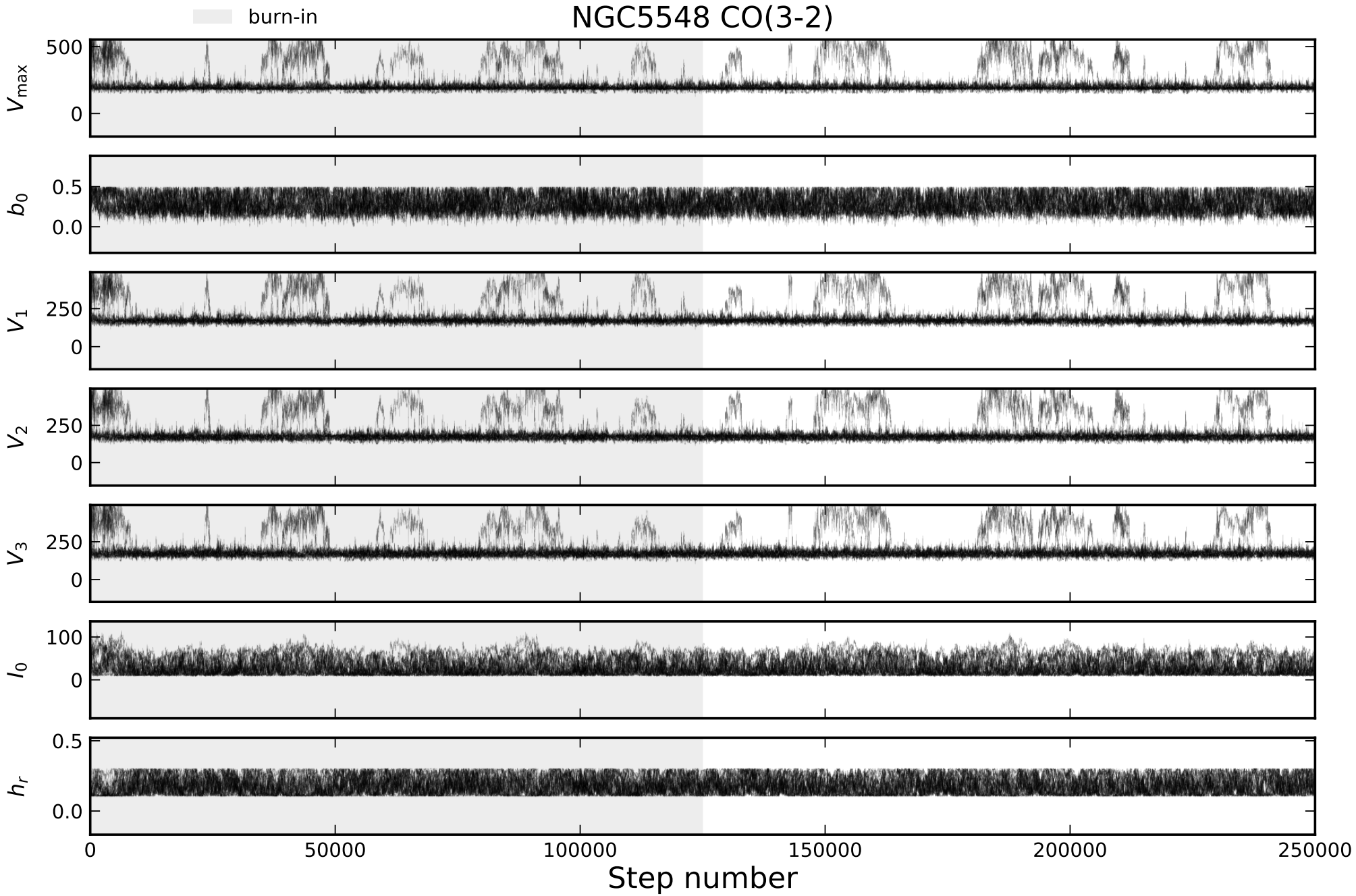

Fig. B.35: Same as Fig. B.3, but for NGC 5548 CO(3-2).

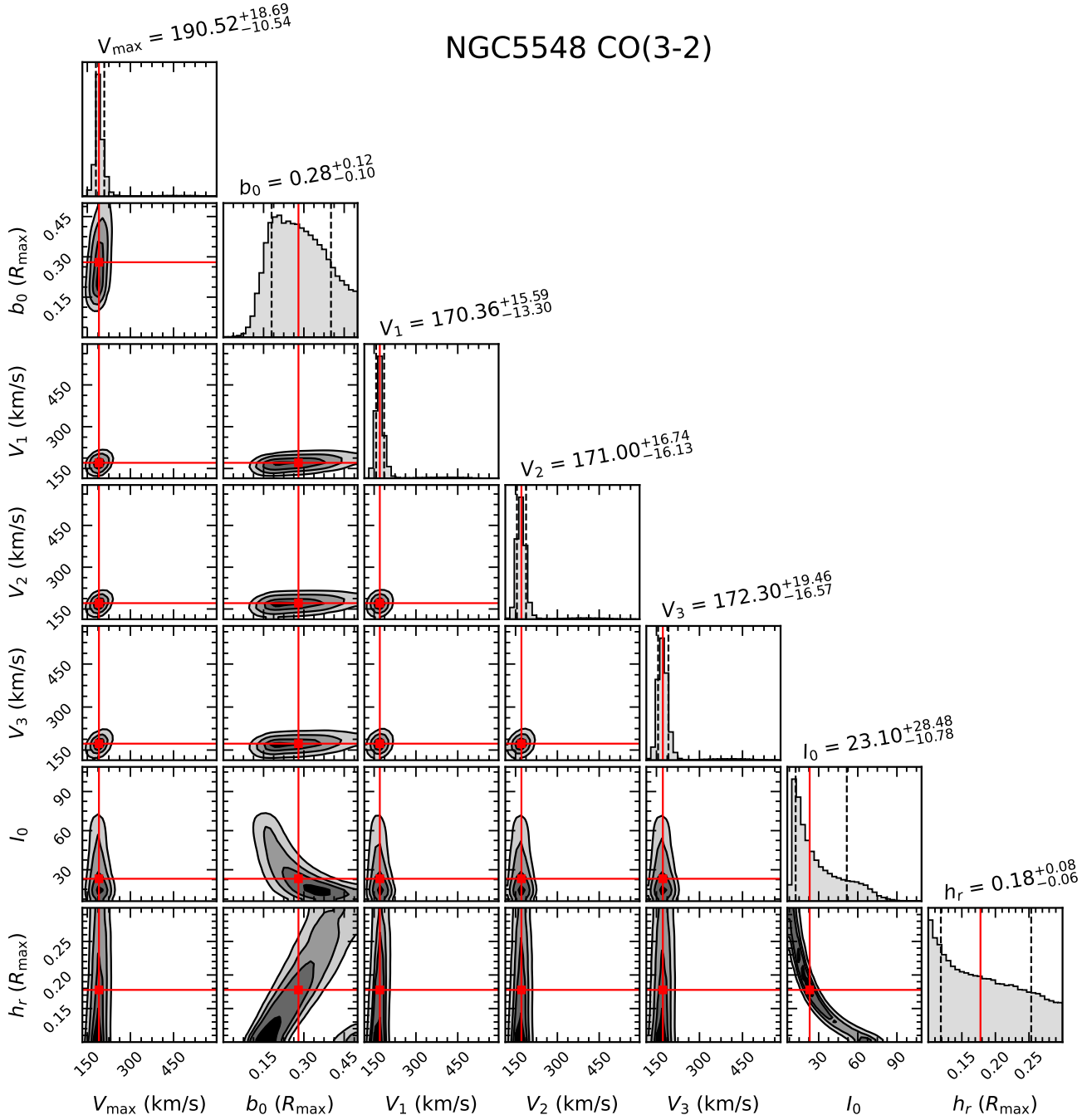

Fig. B.36: Same as Fig. B.4, but for NGC 5548 CO(3-2).

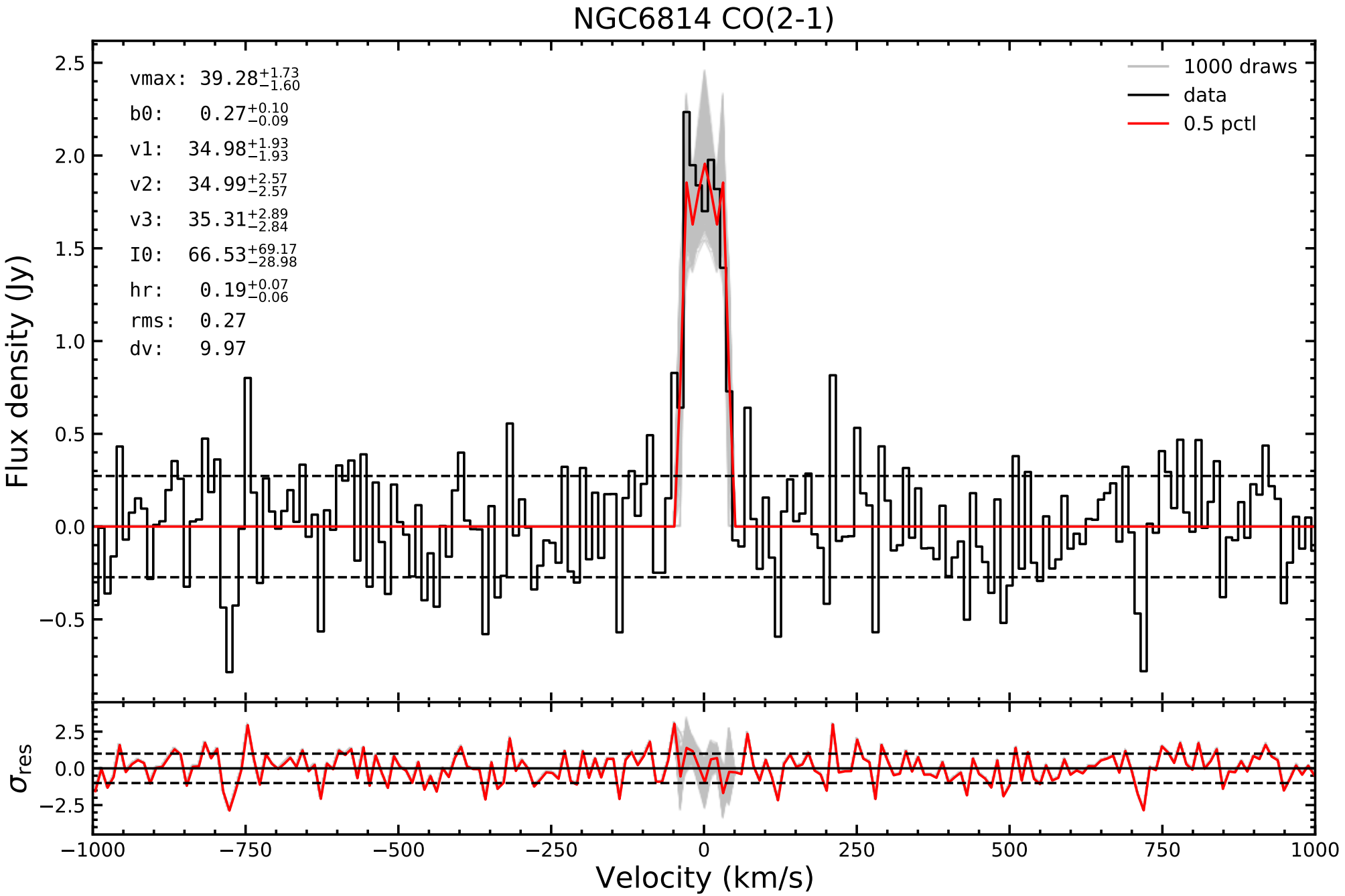

Fig. B.37: Same as Fig. B.1, but for NGC 6814 CO(2-1).

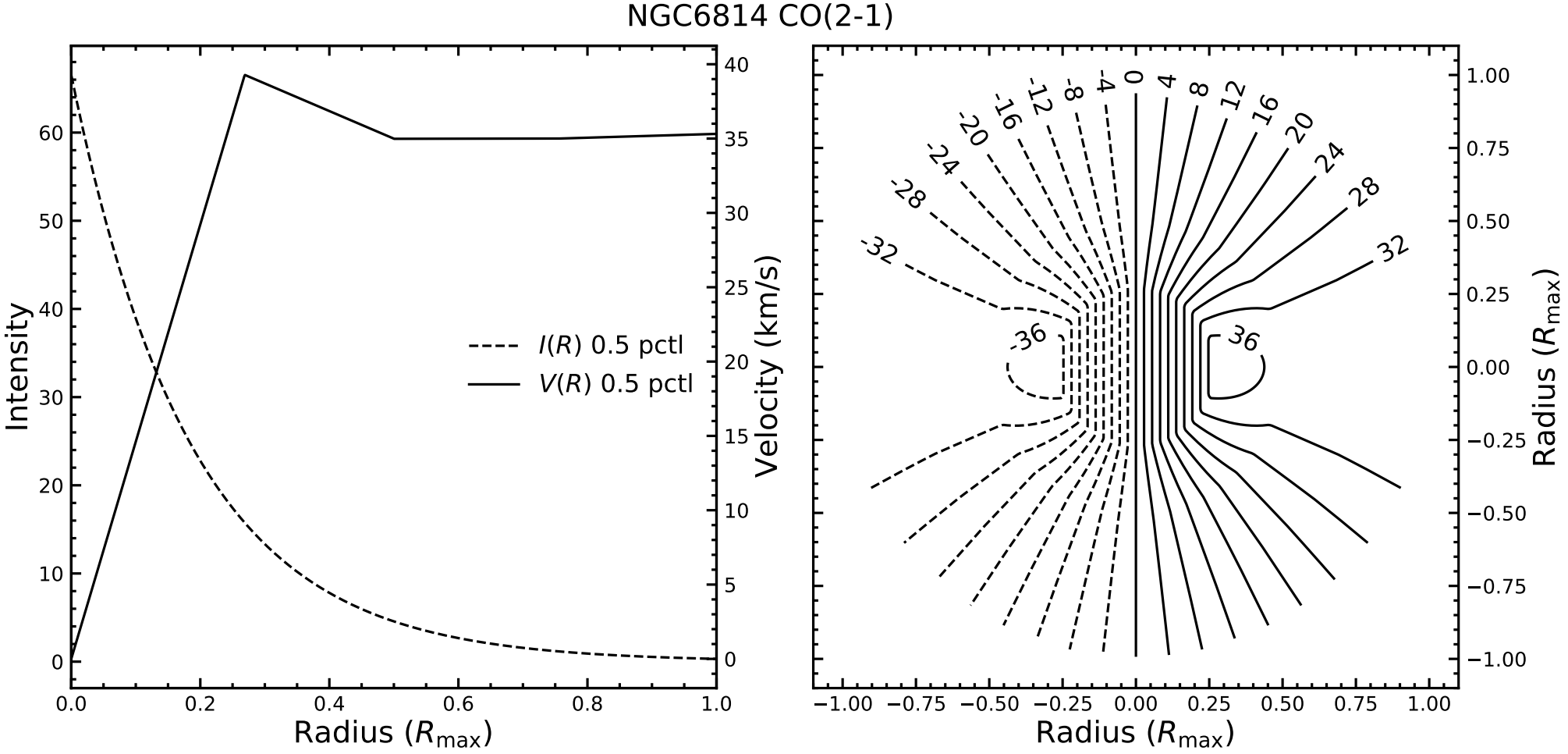

Fig. B.38: Same as Fig. B.2, but for NGC 6814 CO(2-1).

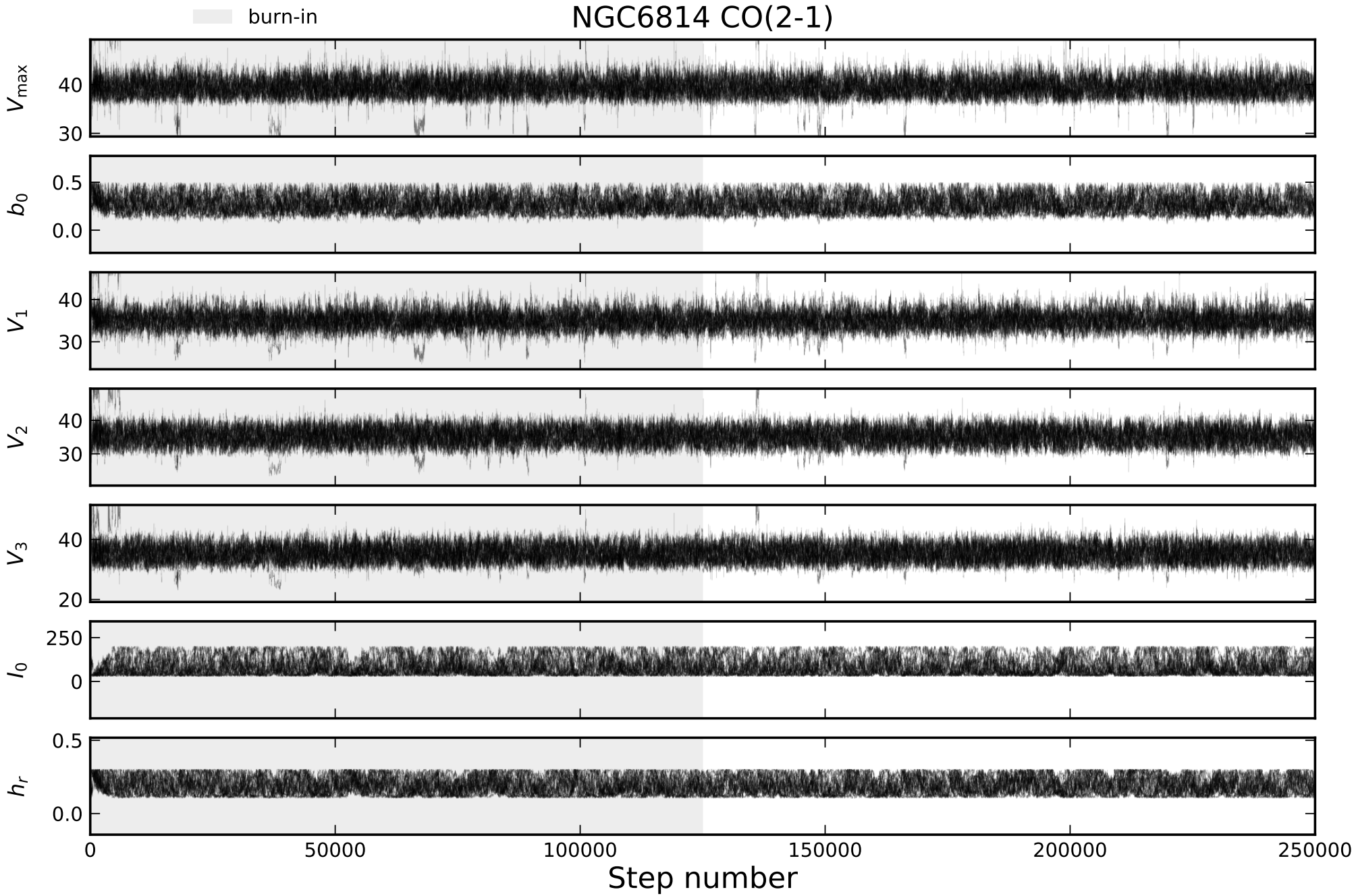

Fig. B.39: Same as Fig. B.3, but for NGC 6814 CO(2-1).

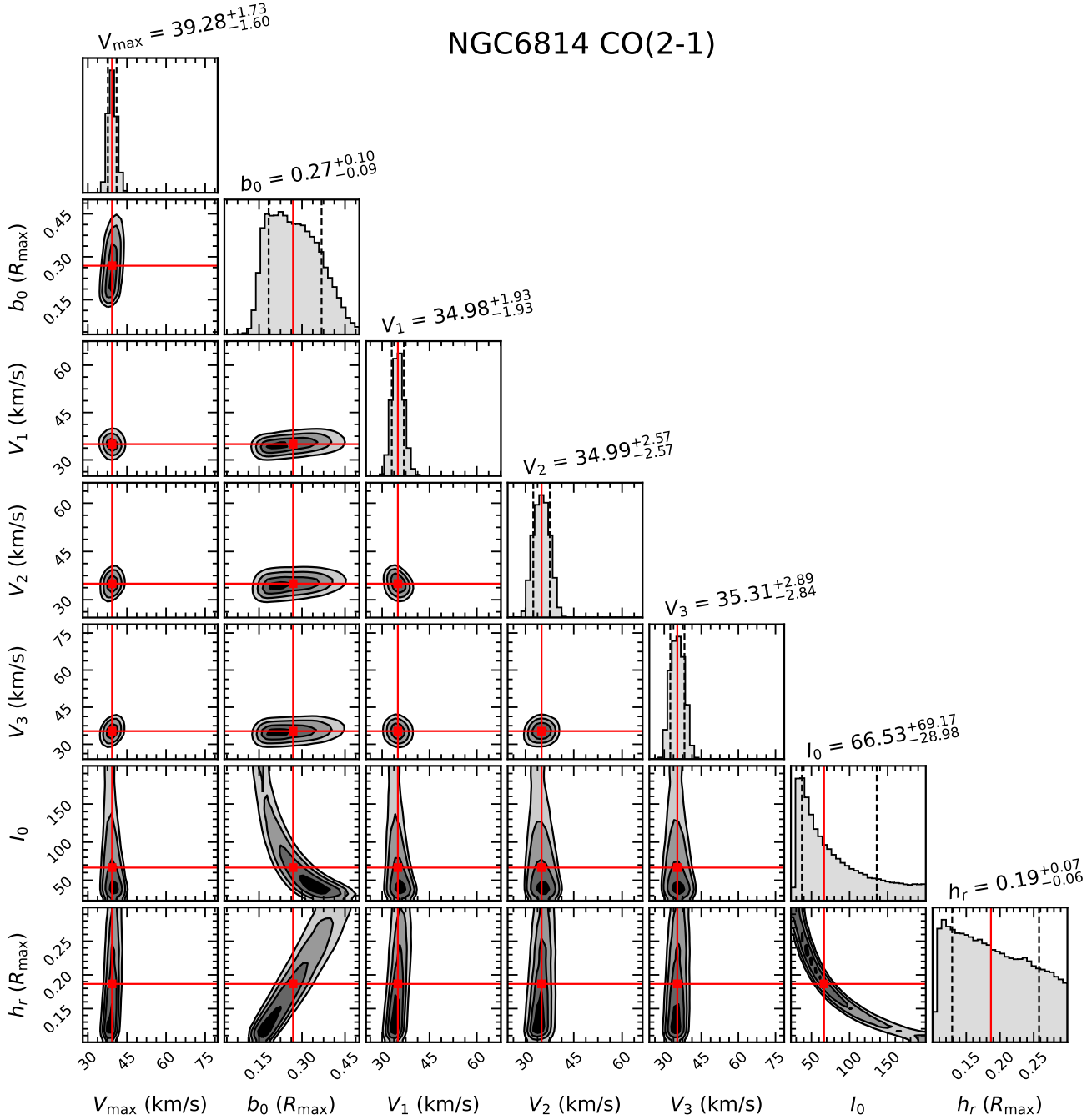

Fig. B.40: Same as Fig. B.4, but for NGC 6814 CO(2-1).

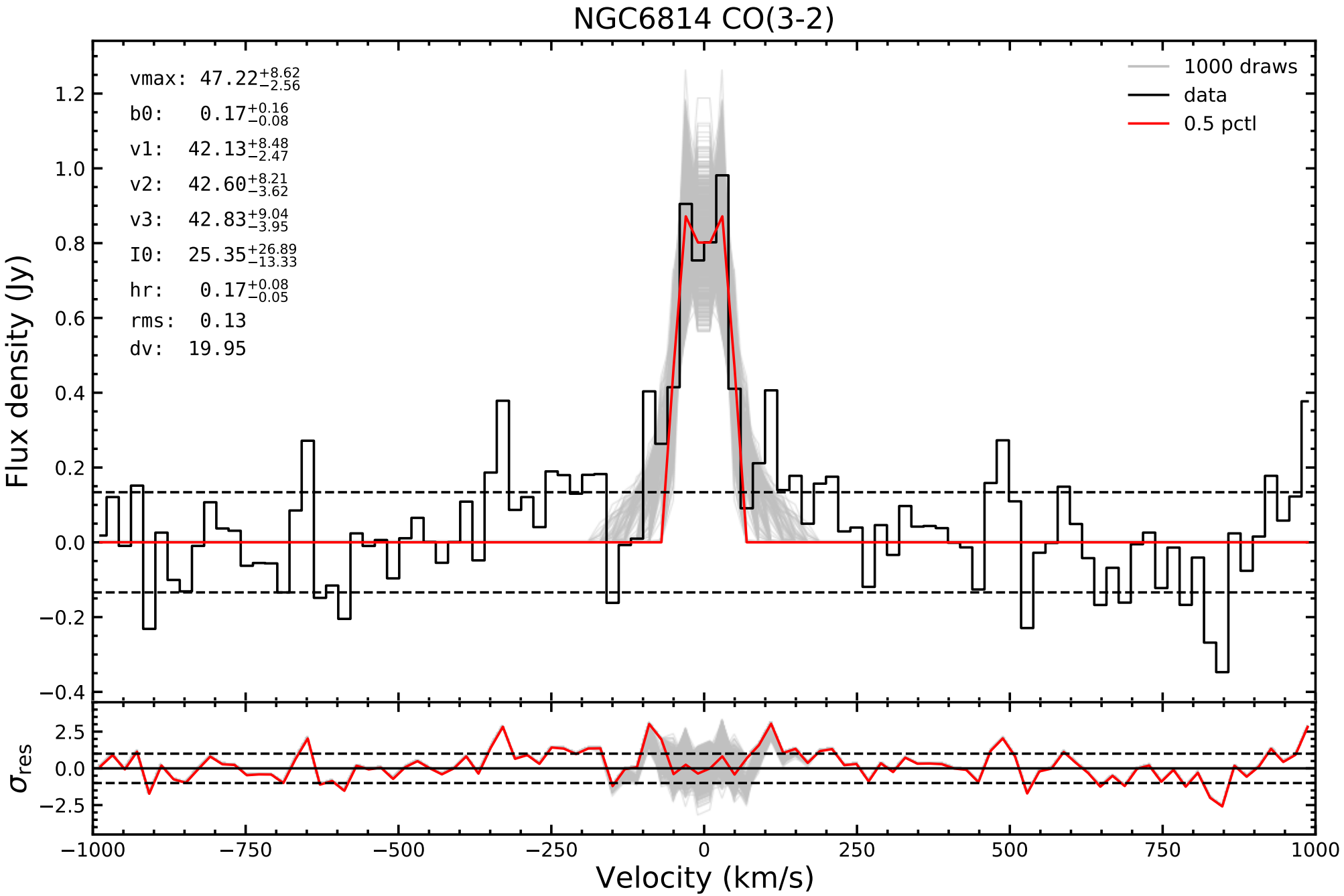

Fig. B.41: Same as Fig. B.1, but for NGC 6814 CO(3-2).

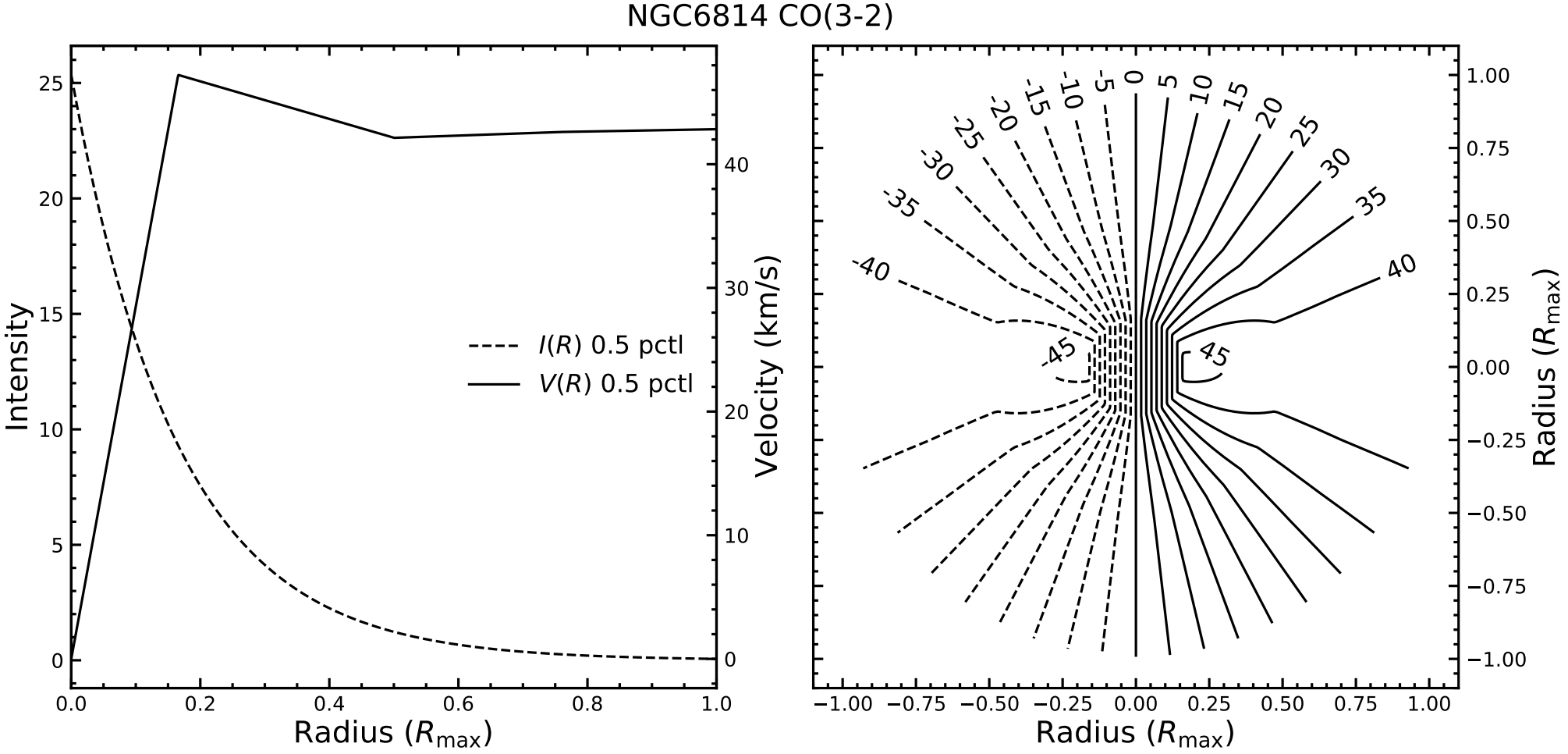

Fig. B.42: Same as Fig. B.2, but for NGC 6814 CO(3-2).

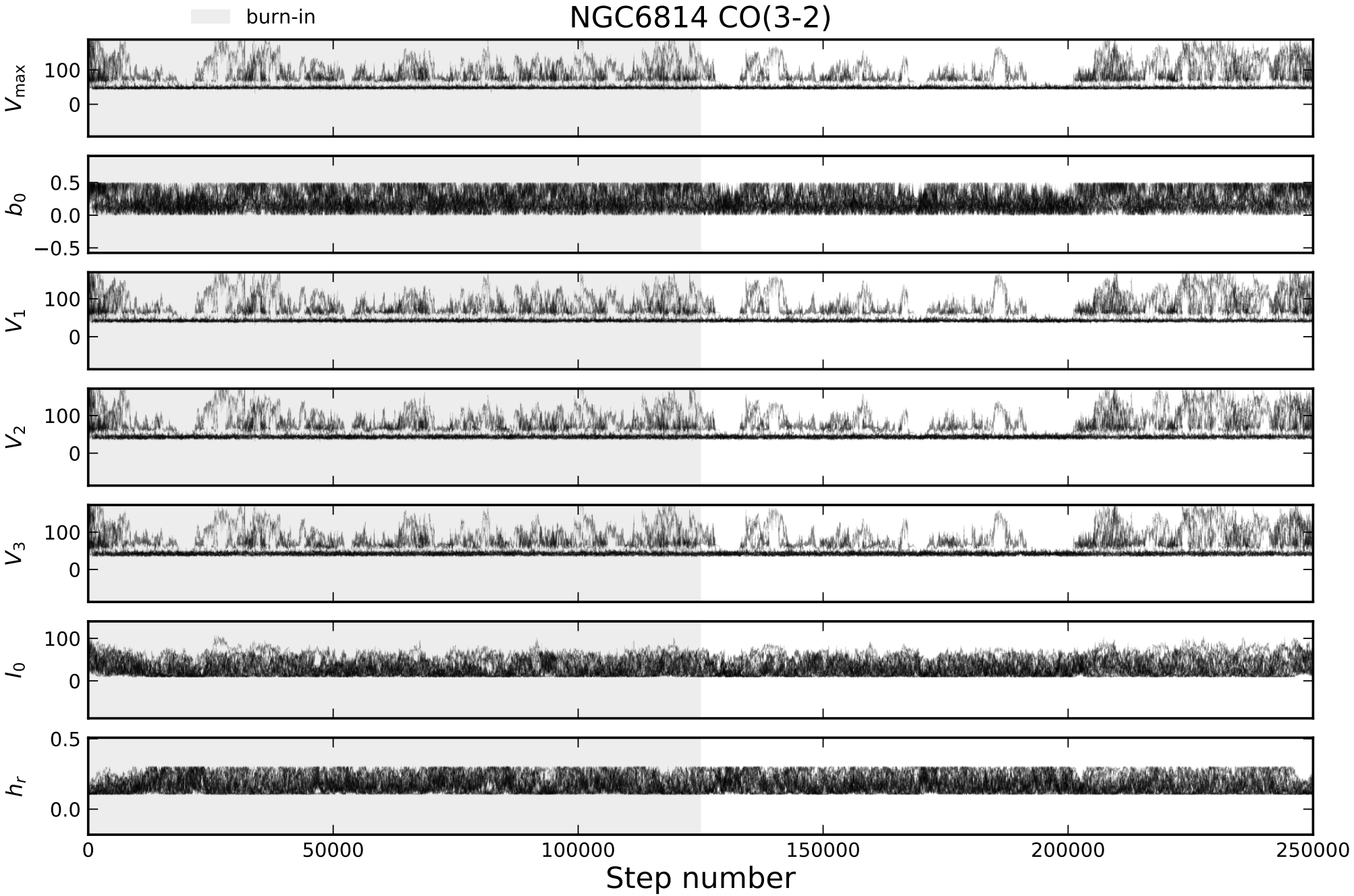

Fig. B.43: Same as Fig. B.3, but for NGC 6814 CO(3-2).

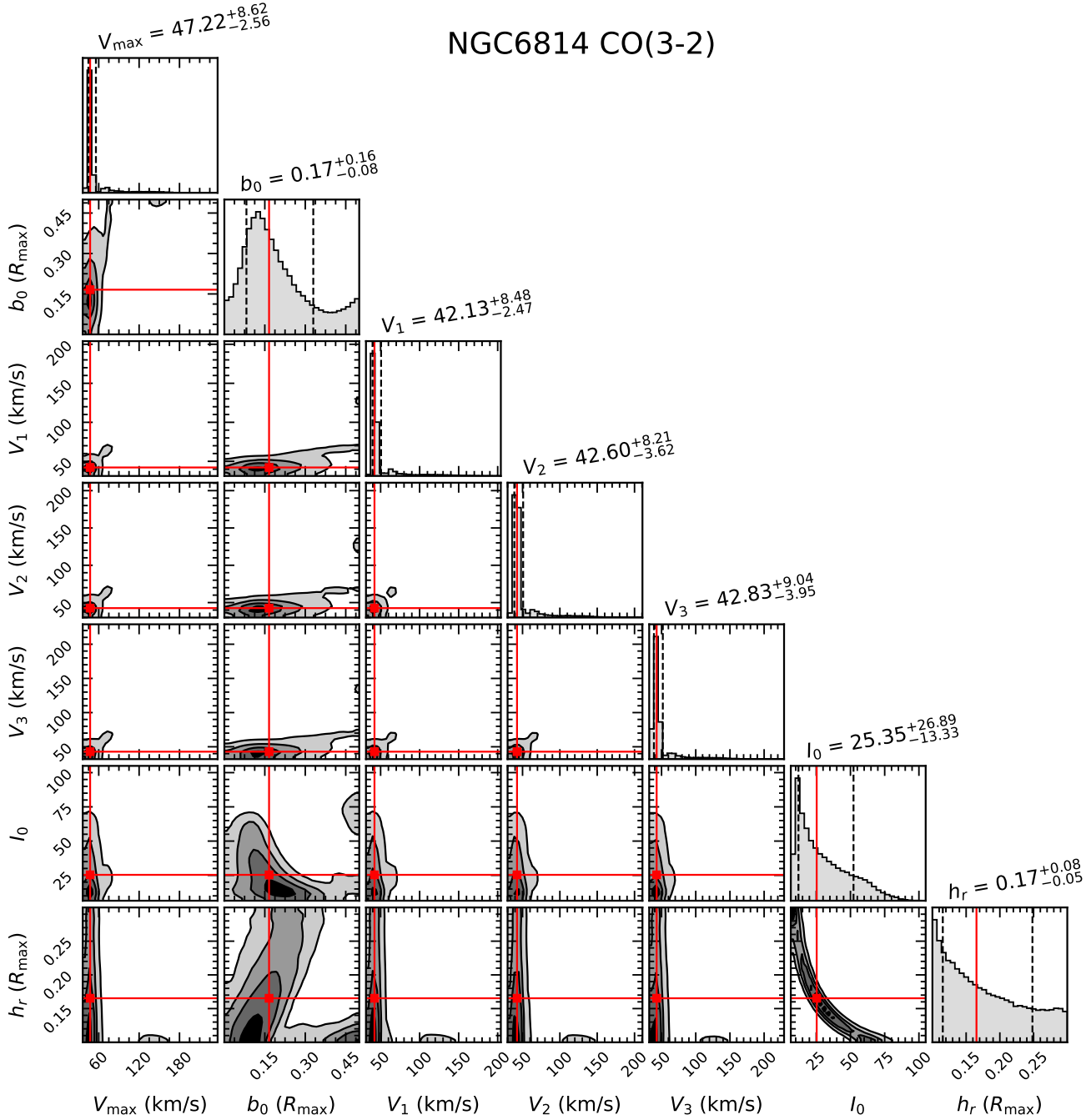

Fig. B.44: Same as Fig. B.4, but for NGC 6814 CO(3-2).

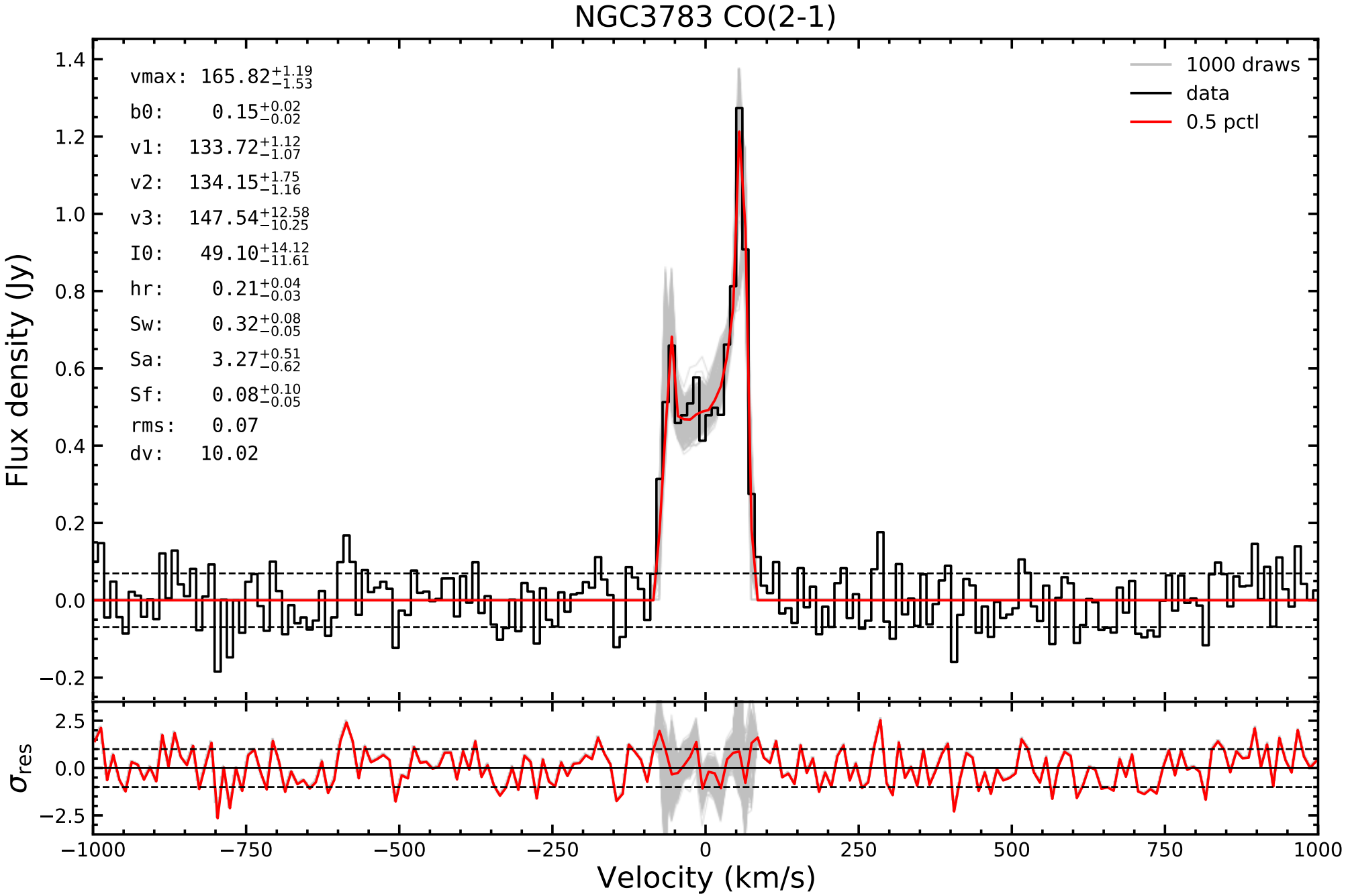

Fig. B.45: Same as Fig. B.1, but for NGC 3783 CO(2-1) and the addition of the S_w, S_a and S_f model parameters listed in Table 4.2.

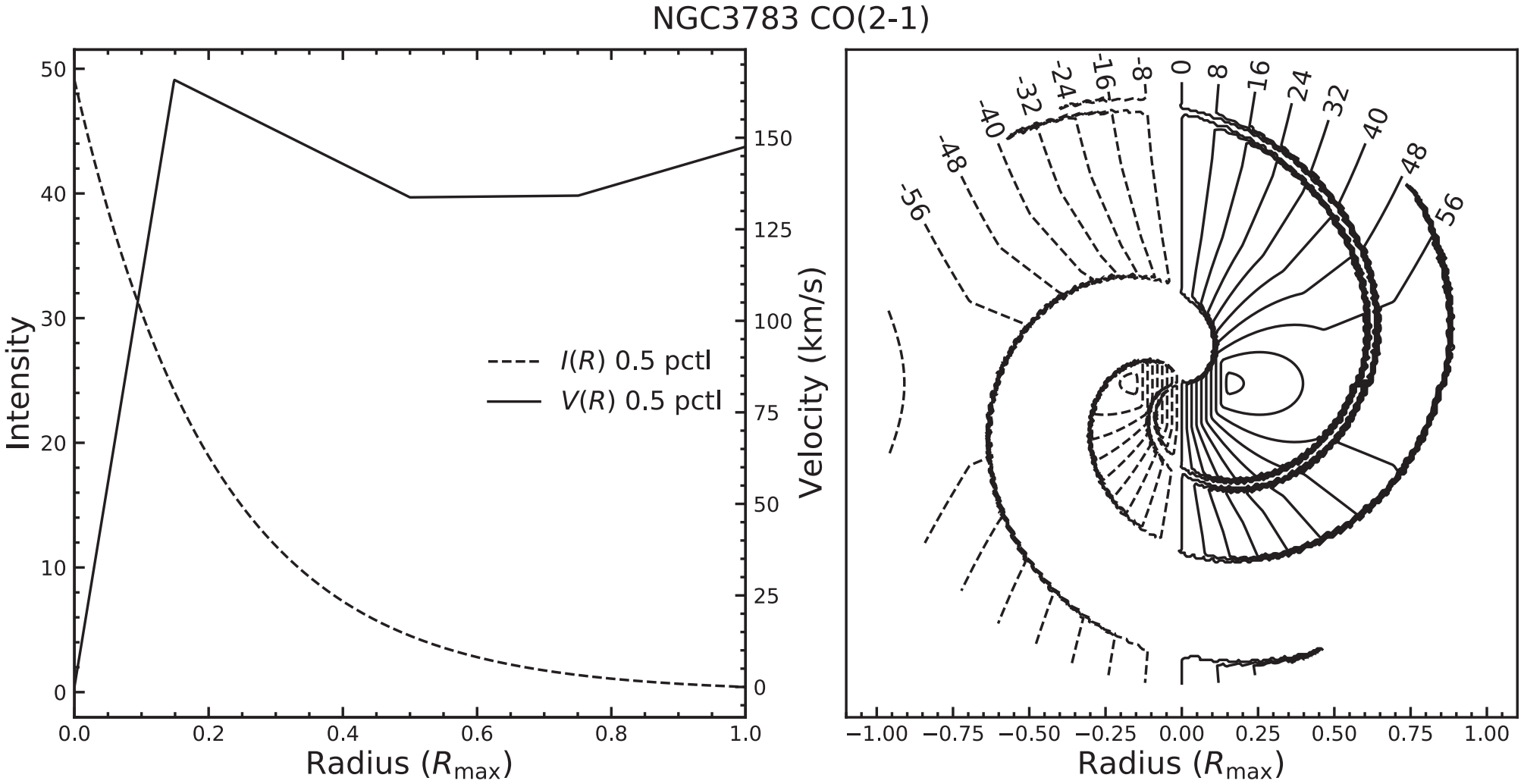

Fig. B.46: Same as Fig. B.2, but for NGC 3783 CO(2-1) and the addition of the S_w, S_a and S_f model parameters listed in Table 4.2. The masked regions devoid of contours are the regions that have had their flux decreased by a factor S_f. These masks are shown purely for visualization purposes; they do not alter the radial velocity of gas at the position, only the flux.

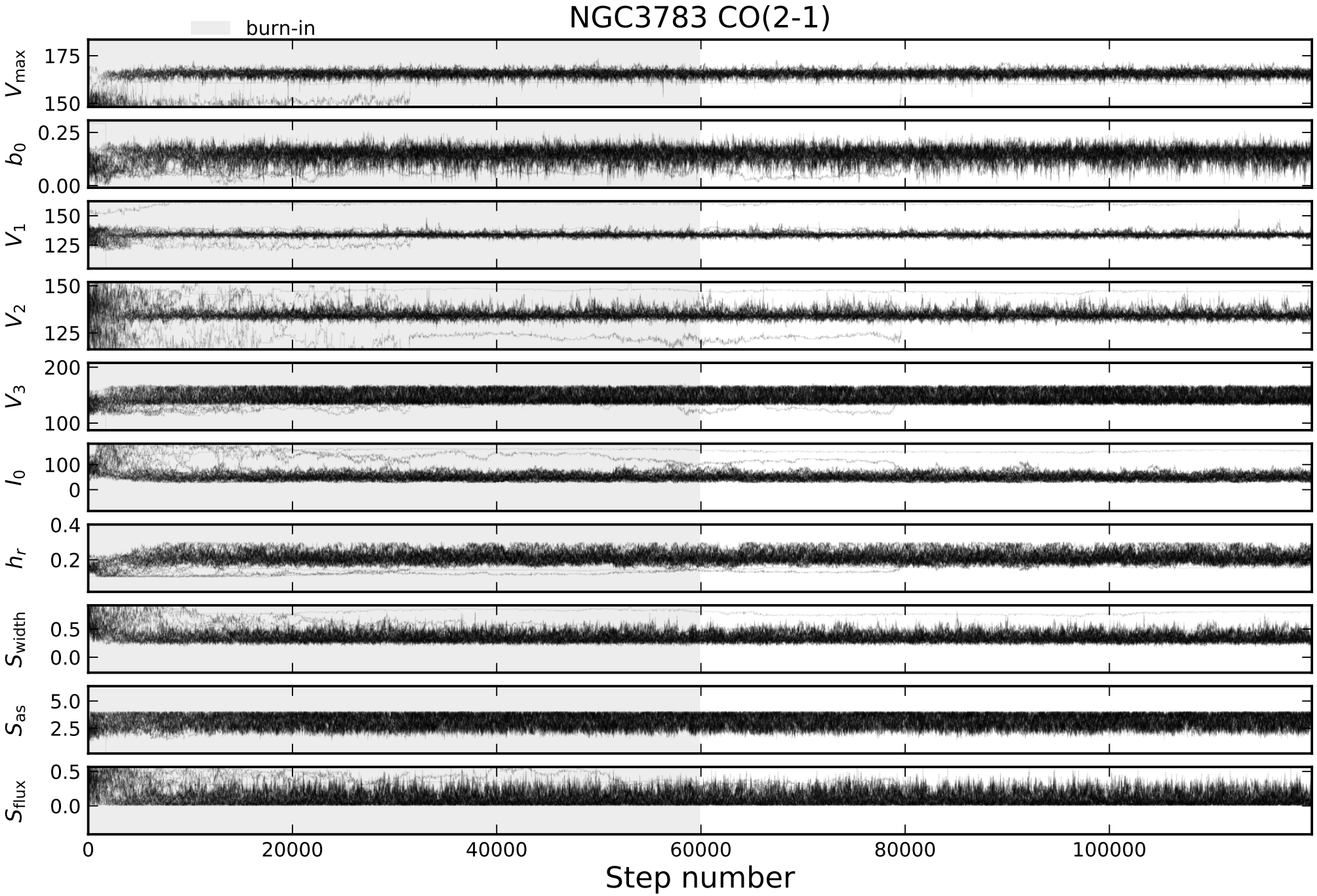

Fig. B.47: Same as Fig. B.3, but for NGC 3783 CO(2-1) and the addition of the S_w, S_a and S_f model parameters listed in Table 4.2.

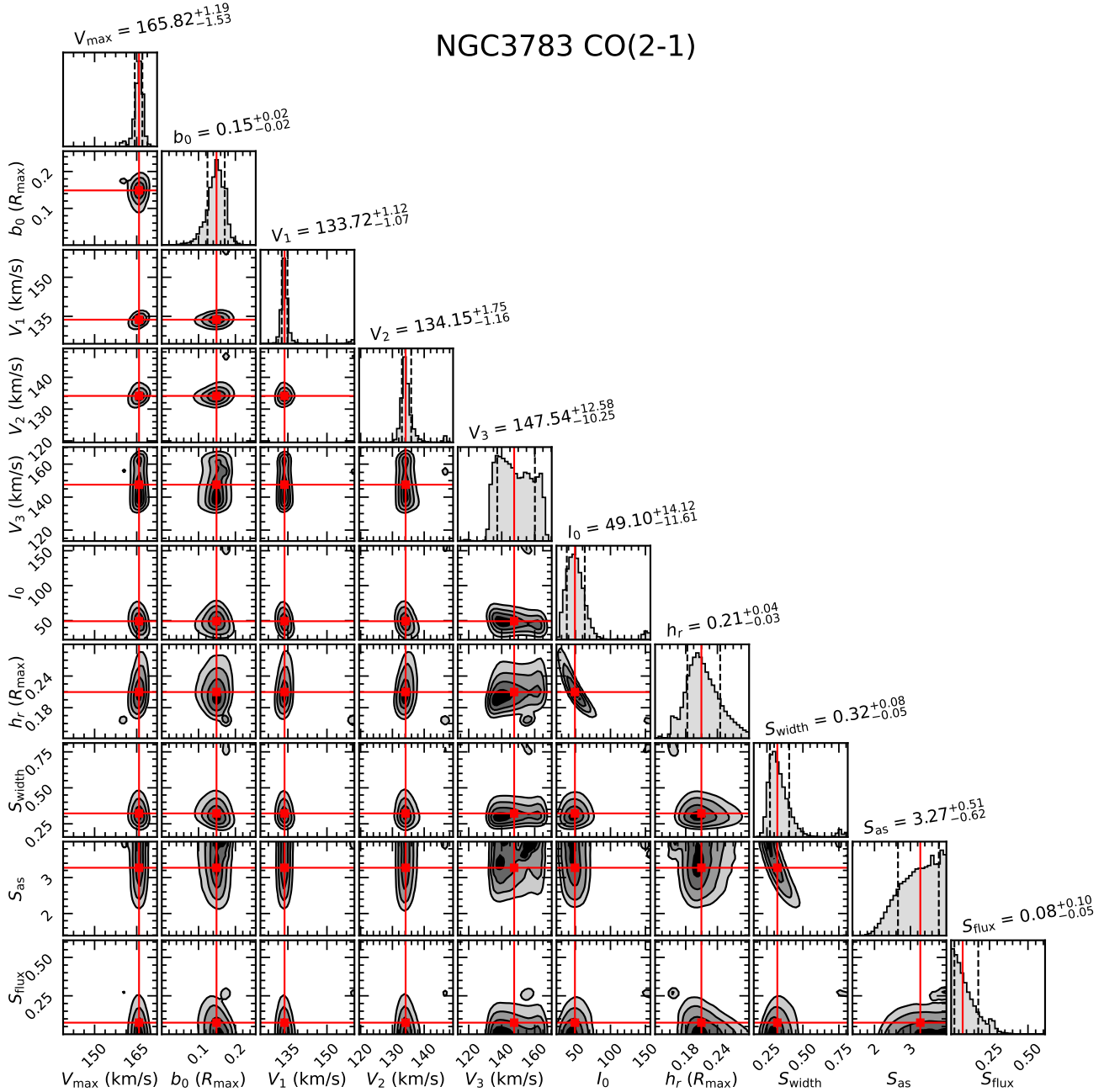

Fig. B.48: Same as Fig. B.4, but for NGC 3783 CO(2-1) and the addition of the S_w, S_a and S_f model parameters listed in Table 4.2.